

Tool Path Planning for Wire-Arc Additive Manufacturing Processes

Von der Fakultät für Maschinenbau, Elektro- und Energiesysteme
der Brandenburgischen Technischen Universität Cottbus–Senftenberg
zur Erlangung des akademischen Grades eines
Doktors der Ingenieurwissenschaften

genehmigte Dissertation

vorgelegt von

MSc.

Qui Lam Nguyen

geboren am 03.01.1991 in Hanoi, Vietnam

Vorsitzender: Prof. Dr.-Ing. Sebastian Härtel

Gutachter: Prof. Dr.-Ing. habil. Markus Bambach

Gutachter: Dr. Evros Loukaides

Tag der mündlichen Prüfung: 31.05.2022

DOI: 10.26127/BTUOpen-5982

“The only certainty in life is that it is uncertain”

[Charles F.Glassman]

Abstract (English)

Digital factories are the future of manufacturing. Leading manufacturing companies are deploying new manufacturing methods into production to cut costs, decrease lead time, reduce risks within the supply chain, and enhance environmental quality. One of these new processes is called additive manufacturing (AM), which differs from conventional manufacturing methods wherein parts are produced by removing materials from wrought blocks or are formed between dies. With AM, materials are added next to each other layer-by-layer to build 3D parts from metals, composites, ceramics, or biomaterials. Among variants of AM technology is the wire-arc additive manufacturing (WAAM) process, which can suitably produce bulky metal parts with a medium complexity due to the building rate, a large working volume, low costs of material and operation as well as low investment costs. The WAAM process uses a heat source to melt the feedstock as metal wire. The heat source can be a laser, electron beam, or electric arc. Due to the characteristics of the gas metal arc welding (GMAW) process, this welding technique is adopted for additive applications whenever feasible. Although WAAM shows great potential to realize digital manufacturing, this process has not been fully explored. There is still room for development and innovation and is therefore a worthwhile subject to further investigate.

This monograph engages with tool path planning for the WAAM process, beginning with a general introduction and the state of the art of WAAM. Using this information as a basis, existing problems in WAAM are subsequently addressed. Before resolving these problems, the next part of the monograph introduces the hardware of a robot based WAAM process. The WAAM system includes a Fronius welder with cold metal transfer (CMT) technology along with a welding torch that is mounted on a six-axis FANUC robot arm. The substrate is placed on a two-axis FANUC positioner allowing for the robot arm and the positioner to coordinate and ultimately perform coordinated motion. Along with specifications, the procedure and tools needed to compile the robot program are also presented in this part. The following sections propose remedies for existing problems, such as multi-bead overlapping models, tool path generation for lightweight structures, a multi-axis deposition strategy, and the extension of the multi-axis deposition strategy in order to produce curved, thinly walled structures.

The existing overlapping models yield an uneven surface because edges of metal parts lag the inner. This is due to the inner beads overlapping with two neighbor beads while the outers

have only a one-sided overlap. New mathematical models are established to obtain the optimal distance between adjacent weld beads and to make surfaces more even.

Lightweight structures are widely applied in many industrial applications due to their high strength as compared to their weight. Producing these structures by WAAM results in imperfections because of uneven weld beads, an inevitable phenomenon when starting a new welding pass. A new tool path strategy to produce lightweight structures is developed using contour patterns, which transforms any arbitrary geometry into that of a continuous Eulerian path. Unfortunately, voids are formed at junctions when using contour patterns. An adaptive correction using machine learning is then developed to overcome this defect.

Large overhang and inclined features are out of reach of WAAM when the welding torch injects material in the x-y plane and when the growth direction is +Z direction in Cartesian system. This limits the ability of the WAAM process. To overcome this limit, each overhang feature should be welded with a distinct direction. This approach is realized within the robot based WAAM process. Establishing the kinematics of the FANUC robot arm and the positioner helps compute the new coordinates of control points, the angular displacements of the positioner, and the orientation of the gun. The proposed strategy is examined through the construction of an overhang part.

The capabilities of the multi-axis deposition are further extended by means of curved, thinly walled structures. The WAAM process with a multi-axis deposition can replace conventional manufacturing methods, such as the bending process. Unlike conventional AM, irregular thickness layers are deposited by controlling the travel speed, resulting in a different deposition rate. The curved, thinly walled structures can be properly fabricated by combining a multi-axis deposition with non-uniform thickness layers. Bonding quality as well as geometric accuracy are also to be investigated. It turns out that material shrinkage and distortion always occur in welded parts. To ensure for geometric accuracy, a compensation strategy based on an experimental approach is developed. The performance of the proposed algorithm is validated on four different geometries.

This paper will conclude with a summary of this work's main achievements and contributions as well as outlooks on future research.

Keywords: Wire-arc additive manufacturing, Lightweight structures, Curve thin-walled structures, Multi-bead overlapping models

Kurzfassung (Deutsch)

Digitale Fabriken prägen die Zukunft der Fertigung, wenn führende Produktionsunternehmen neue Fertigungsmethoden in der Produktion einsetzen, um Kosten zu senken, Vorlaufzeiten zu verkürzen, Risiken in der Lieferkette zu reduzieren und die Umweltqualität zu verbessern. Eines dieser neuen Verfahren ist die additive Fertigung (AM) und unterscheidet sich von konventionellen Fertigungsmethoden, bei denen Teile durch die Entnahme von Materialien aus geschmiedeten Blöcken oder die Formung zwischen Werkzeugen hergestellt werden. Bei AM werden Materialien nebeneinander und schichtweise hinzugefügt, um 3D-Teile aus Metallen, Verbundwerkstoffen, Keramiken oder Biomaterialien herzustellen. Unter den Varianten der AM-Technologie eignet sich das WAAM-Verfahren (Wire-Arc Additive Manufacturing) aufgrund der Baurate, des großen Arbeitsvolumens, der geringen Material- und Betriebskosten sowie der niedrigen Investitionskosten zur Herstellung von sperrigen Metallteilen mit mittlerer Komplexität. Das WAAM-Verfahren verwendet eine Wärmequelle, um das Ausgangsmaterial als Metalldraht zu schmelzen. Die Wärmequelle kann ein Laser, ein Elektronenstrahl oder ein elektrischer Lichtbogen sein. Aufgrund der Eigenschaften des Metall-Schutzgasschweißens (GMAW) wird diese Schweißtechnik für additive Anwendungen eingesetzt, wann immer dies möglich ist. Obwohl das WAAM-Verfahren ein großes Potenzial zur Realisierung der digitalen Fertigung hat, ist es noch nicht voll ausgeschöpft. Daher gibt es noch Raum für Entwicklung und Innovation, und es lohnt sich, dies umzusetzen.

Diese Monografie beschäftigt sich mit der Werkzeugbahnplanung für den WAAM-Prozess, sie beginnt mit der allgemeinen Einführung und dem Stand der Technik von WAAM. Darauf aufbauend werden bestehende Probleme in WAAM angesprochen. Bevor diese Probleme gelöst werden, wird im nächsten Teil der Monografie die Hardware eines roboterbasierten WAAM-Prozesses vorgestellt. Das WAAM-System besteht aus einem Fronius-Schweißgerät mit Cold Metal Transfer (CMT)-Technologie, der Schweißbrenner ist auf einem sechssachsigen FANUC-Roboterarm montiert und das Substrat wird auf einem zweiachsigen FANUC-Positionierer platziert, der Roboterarm und der Positionierer koordinieren sich, um eine koordinierte Bewegung durchzuführen. Neben den Spezifikationen werden in diesem Teil auch das Verfahren und die Werkzeuge zur Erstellung des Roboterprogramms vorgestellt. In den nächsten Teilen werden Lösungen für bestehende Probleme vorgeschlagen, wie z. B. die Überlappungsmodelle für Mehrfachsicken, die Werkzeugbahngenerierung für Leichtbaustrukturen, die mehrachsige

Abscheidungsstrategie und die Erweiterung der mehrachsigen Abscheidungsstrategie zur Herstellung gekrümmter dünnwandiger Strukturen.

Die bestehenden Überlappungsmodelle ergeben eine ungleichmäßige Oberfläche, die Kanten der Metallteile liegen innen, weil die inneren Sicken mit zwei Nachbarsicken überlappt werden, während die äußeren nur eine einseitige Überlappung haben. Es werden neue mathematische Modelle aufgestellt, um den optimalen Abstand zwischen benachbarten Schweißraupen zu erhalten, damit die Oberflächen gleichmäßiger werden.

Leichtbaustrukturen werden aufgrund ihrer hohen Festigkeit im Vergleich zum Gewicht in vielen industriellen Anwendungen eingesetzt. Die Herstellung dieser Strukturen mittels WAAM führt zu Imperfektionen aufgrund ungleichmäßiger Schweißraupen, und dieses Phänomen ist unvermeidlich, wenn ein neuer Schweißdurchgang begonnen wird. Für die Herstellung von Leichtbaustrukturen wird eine neue Werkzeugbahnstrategie unter Verwendung von Konturmustern entwickelt, die jede beliebige Geometrie in eine Eulersche Bahn umwandelt, um eine kontinuierliche Bahn zu erzeugen. Leider bilden sich bei der Verwendung von Konturmustern Hohlräume an Kreuzungspunkten. Um diesen Fehler zu beheben, wird eine adaptive Korrektur mit maschinellem Lernen entwickelt.

Große überhängende und geneigte Merkmale sind außerhalb der Reichweite des WAAM, wenn der Schweißbrenner Material in der x-y-Ebene einspritzt und die Wachstumsrichtung die +Z-Richtung im kartesischen System ist. Dies begrenzt die Leistungsfähigkeit des WAAM-Prozesses. Um diese Grenze zu überwinden, sollte jedes Überhangsmerkmal mit einer bestimmten Richtung geschweißt werden, und dieser Ansatz wird mit dem roboterbasierten WAAM-Prozess realisiert. Die Kinematik des FANUC-Roboterarms und des Positionierers wird erstellt, was bei der Berechnung der neuen Koordinaten der Kontrollpunkte, der Winkelverschiebungen des Positionierers und der Ausrichtung des Schweißbrenners beiträgt. Die vorgeschlagene Strategie wird anhand der Konstruktion eines Überhangteils untersucht.

Die Fähigkeit des mehrachsigen Ablegens wird bei gekrümmten dünnwandigen Strukturen weiter ausgebaut. Der WAAM-Prozess mit mehrachsiger Abscheidung kann konventionelle Fertigungsmethoden, z. B. Biegeverfahren, ersetzen. Im Unterschied zum konventionellen AM werden durch die Steuerung der Verfahrensgeschwindigkeit Schichten ungleichmäßiger Dicke abgeschieden, was zu einer unterschiedlichen Abscheiderate führt. Mit der Kombination aus mehrachsiger Abscheidung und ungleichmäßig dicken Schichten können

gekrümmte dünnwandige Strukturen hergestellt werden. Die Klebequalität und die geometrische Genauigkeit werden untersucht. Es stellt sich heraus, dass bei geschweißten Teilen immer Material schrumpft und Verzug auftritt. Um die geometrische Genauigkeit zu gewährleisten, wird eine Kompensationsstrategie auf Basis eines experimentellen Ansatzes entwickelt. Die Leistungsfähigkeit des vorgeschlagenen Algorithmus wird an vier verschiedenen Geometrien validiert.

Der letzte Teil fasst die wichtigsten Ergebnisse und Beiträge dieser Arbeit zusammen und gibt einen Ausblick auf zukünftige Forschung.

Schlagwörter: Lichtbogenadditive Fertigung, Leichte Strukturen, Gekrümmte dünnwandige Strukturen, Überlappende Modelle

Acknowledgements

This work would have not been possible without the support of so many people and so I would like to express my sincerest gratitude to each of these people. First and foremost, I would like to thank Prof. Dr. Markus Bambach for inspiring me with his distinct mentoring. He provided me free room to explore new ideas and approaches while keeping me on the track of my own academic adventure. I am very grateful for his superb mentoring along with the useful advice he provided for my dissertation.

I also owe thanks to Dr. Johannes Buhl for his great deal of support. His critical thinking and scientific approach helped me a lot in the accomplishment of this research. In addition, Dr. Buhl provided several opportunities to learn new things, helping me gain a great deal of knowledge and skills. He ultimately became a sort of older brother for me, not only because of his kindness and willingness to aid me, but also for the invaluable advice for personal life.

A special thanks to all my colleagues at BTU Cottbus-Senftenberg for their support in this study, especially Angelika Jedynak, Benjamin Sydow, Mario Pietzig, Markus Hirtler, Lemopi Isidore Besong, Johan Andreas Stendal, Irina Sizova, Thawin Hart-Rawung, Robert Goldmann, Lutz Jaeger. Thanks also to Ms. Rodenbeck, the Chair of Materials and Physical Metallurgy for her assistance with tensile tests.

I would like to express, from the very bottom of my heart, my sincerest gratitude to my family for all they have done for me. They broke their backs to provide me with exceptional opportunities for personal and professional development.

Finally, I would like to thank my friends for being by my side and for providing emotional support during my journey.

Qui Lam Nguyen

Cottbus, May 2020

List of Figures

Fig. 1 The three phases of an AM process.....	23
Fig. 2 A schematic diagram of the wire-based technique: (a) WLAM; (b) EBF ³ ; (c) GTAW additive manufacturing; (d) GMAW additive manufacturing	24
Fig. 3 A schematic of a cross section of single weld bead, as reported in Ref. [43]	26
Fig. 4 Stair steps among adjacent layers	28
Fig. 5 An uneven weld bead: (a) real weld bead (a) and (b) schematic cross section of a weld bead.....	31
Fig. 6 Weld bead humping: (a) gouging region morphology and (b) beaded cylinder morphology, as reported in Ref. [95].....	32
Fig. 7. A schematic of typical tool path patterns: (a) zigzag; (b) contour; (c) hybrid	33
Fig. 8 A schematic of void formation among adjacent weld beads.....	34
Fig. 9 A representation of a schematic tool path as a graph	35
Fig. 10 Robot classification by the mechanical structures, as reported in Ref. [141]	42
Fig. 11 A schematic of a synergic line, as reported in Ref. [151]	44
Fig. 12. An illustration of the frame system of the robot arm in Cartesian coordinates.....	46
Fig. 13. An illustration of the two-axis positioner	47
Fig. 14 Illustration of the process chain (a) and WAAM robot system (b)	49
Fig. 15. Coordinated motion overview	50
Fig. 16 Leica DFC290 stereomicroscope	51
Fig. 17 ATOS 5 system - 3D scanner	52
Fig. 18 Uniaxial tensile testing machine ‘Inspekt 100’	52
Fig. 19. Schematic of weld pool shape: (a) elliptical shape; (b) tear drop shape	55
Fig. 20. A schematic of a multi-bead profile for zigzag and contour patterns	56
Fig. 21. A schematic of the cross section of the multi-bead profiles.....	58
Fig. 22. A schematic of examined blocks.....	59

Fig. 23. Macrographs of specimens: (a) existing overlapping distance ($d_l = 0.738w$); (b) proposed overlapping distance ($d_l = 0.47w$).....	60
Fig. 24. A comparison of surface profiles between the proposed models and the existing model	61
Fig. 25. A schematic of specimen extraction for the waviness investigation.....	64
Fig. 26. A representation of the tool path by a graph: (a) single pass; (b) double pass without connector lines; (c) double pass with connector lines	65
Fig. 27. Eulerian path generation: (a) illustration of the slice procedure; (b) cross section; (c) offset curves; (d) valid path; (e) invalid path.....	66
Fig. 28. A schematic of a basic adaptive void-filling path	67
Fig. 29. A welding speed diagram at a turning point: (a) tool path pattern; (b) velocity diagram	67
Fig. 30. An illustration of determining L with standard contour	68
Fig. 31. A comparison between (a) standard contour tool path and (b) corrective contour tool path.....	70
Fig. 32. The types of junctions considered: (a) three ribs with three equal angles; (b) three ribs with two equal angles; (c) three ribs with different angles; (d) four ribs with four equal angles; (e) four ribs with three equal angles; (f) four ribs with two-pair of equal angles; (g) four ribs with one-pair of equal angles; (h) four ribs with different angles (h).....	71
Fig. 33. A schematic architecture of the ANN	71
Fig. 34. The tool path for a layer of the tensile testing samples: (a) wall; (b) cross feature	72
Fig. 35. Preparation of tensile specimens: for the thin wall (a); for the cross feature (b) ...	72
Fig. 36. A technical drawing of the tensile specimen.....	73
Fig. 37. Macrographs of the wall cross sections.....	73
Fig. 38. Macrographs of the two-bead wall cross sections.....	74
Fig. 39. Performance of an example: (a) tool path without correction and (b) tool path with correction	75
Fig. 40. A side view of the metallic part: (a) without correction; (b) with correction.....	75

Fig. 41. Results for various junction geometries: (a) standard contour tool path and (b) adaptive void-filling tool path.....	76
Fig. 42. Junctions with different PPN^* : (a) 0.0 mm; (b) 25.0 mm; (c) 26.0 mm; (d) 27.0 mm	76
Fig. 43. The influence of the shifting distance on void area.....	77
Fig. 44. Regression: (a) training; (b) test	78
Fig. 45. Error histograms for various sets of training / validation data	79
Fig. 46. A comparison of (a) yield strength, (b) elongation, and (c) ultimate tensile strength	80
Fig. 47. The CAD model of the case study: (a) perspective view of the CAD model and (b) a typical intersection	81
Fig. 48. A comparison of the standard contour tool path (a) and the Eulerian tool path (b). The red stars show start/stop positions.	82
Fig. 49. The metal parts after face milling: (a) standard tool path and (b) proposed tool path	83
Fig. 50. The deposition angle: (a) neutral without incline; (b) neutral with torch incline; (c) neutral with positioner incline	87
Fig. 51. A representation of the WAAM robotic system in the Cartesian coordinate: (a) representation of a control point and (b) representation of the frame system	88
Fig. 52. An example of part decomposition: (a) CAD model; (b) model slicing; (c) split overhangs; (d) centroidal axes	92
Fig. 53. A simplification: (a) before removing inner cross sections and (b) after removing inner cross sections	93
Fig. 54. Scenarios between the projected bottom and the top layer: (a) unrelated; (b) uniform; (c) not uniform	93
Fig. 55. Normal vector identification.....	93
Fig. 56. Pseudo code for adjusting moving distance	94
Fig. 57. Split lines determination: (a) step 1; (b) step 2; (c) step 3.....	95

Fig. 58. Trajectory planning: (a) slicing sub-parts; (b) tool path; (c) control points extraction	95
Fig. 59 Building overhanging features: (a) building the bottom; (b) building the cylinder; (c) building the handles; (d) finished part	96
Fig. 60 A nominal model and technical drawing of examined structures	99
Fig. 61 The procedure of adaptive slicing algorithm: (a) schematic and (b) flowchart.....	100
Fig. 62 A representation of the creation of 3D slices: (a) cross section and (b) 1 st 3D slice	101
Fig. 63 A schematic of the start and end portion in a closed weld pass	101
Fig. 64 The construction of inner and outer shells: (a) nominal CAD model; (b) a cross section between the slicing plane and the shell model	103
Fig. 65 Representation of a 3D slice on a bent tube	104
Fig. 66 Process procedure for a metal part	105
Fig. 67 Data acquisition from a 3D slice	105
Fig. 68 A schematic of the CAD intersection with three extracted specimens	106
Fig. 69 A representation of three cutting planes at three positions.....	107
Fig. 70 A schematic of the infrared camera set-up with a reference plate	108
Fig. 71 Representation of distortion caused by the virtual bending moment	109
Fig. 72 A deposited wall with the travel speed of 500 mm/min.....	110
Fig. 73 A scatter chart and interpolation function between travel speed and bead height (dash line) and between bead width and bead height (continuous line).....	111
Fig. 74 Construction of a CAD model: (a) computed CAD model with inner and outer shells; (b) top view of the computed CAD model; (c) intersection of the cutting plane (A-A) and the computed CAD model	112
Fig. 75 A deposition process with WAAM	113
Fig. 76 An illustration of the tool paths: (a) discontinuous; (b) continuous spiral path	113
Fig. 77 Comparison of metal parts from two tool path strategies in part I: (a) discontinuous; (b) continuous; (c) side view	114

Fig. 78 Tool path and metal part. Only every fifth layer is displayed	114
Fig. 79 The macrostructure of the metal part: (a) intersection (grey due to sand blasting); (b) specimen A; (c) specimen B; (d) specimen C.....	115
Fig. 80 Waviness along actual profile	116
Fig. 81 The alignment of the computed CAD models and actual parts.....	117
Fig. 82 A schematic of the target and actual central axis (a) and deviation along the central axis (b)	117
Fig. 83 Cross-section deviation between the computed CAD model and the actual part at three intersections	118
Fig. 84 A box plot for the repeatability at three positions on the central axis.....	119
Fig. 85 Thermal gradient during processing.....	120
Fig. 86 Profile deviation between room temperature and high temperatures.....	121
Fig. 87 A schematic of the central axis with 6 reference points (a) and deviation during the process (b).....	121
Fig. 88 A comparison of surface deviation of two strategies	122
Fig. 89 A schematic of the target and actual central axis (a) and deviation between the actual and the target along the central axis (b).....	122
Fig. 90 An intersectional comparison of the three positions for actual and target geometry with the correction strategy.....	123
Fig. 91 Incomplete layer deposition	124

List of Tables

Table 1 TPS500i Fronius welder [150].....	45
Table 2 Specifications of the ARC Mate 100iC/12 robot arm	46
Table 3 Specifications of the positioner	47
Table 4 Raw data for robot program generation.....	48
Table 5 The chemical composition of ER70S-6 and C45	53
Table 6 The as-welded metal properties of ER70S-6.....	53
Table 7 The chemical composition of AlSi5	53
Table 8 The as-welded metal properties of AlSi5	53
Table 9. Variation of welding parameters	60
Table 10 Process parameters for rib-web structures.....	69
Table 11 Validation of the ANN.....	78
Table 12 A summary of tensile properties results in rib-web structures	81
Table 13 The number of welding passes and the processing time for one layer	82
Table 14 The input data for a multi-axis CAM program.....	96
Table 15 Material and process parameters for the experiment in multi-axis deposition.....	96
Table 16 The maximum and minimum layer thickness for slicing the curved thin-walled models.....	101
Table 17 The raw data for robot program generation.....	105
Table 18 Average height and width of a weld bead	112
Table 19 Validation results for the relationship of bead height and bead width	115
Table 20 The ovality of welded hollow sections	119

Nomenclature

r	Radius of weld pool
h	Weld bead height
w	Weld bead width
l	Overlapping length of inner beads
d_1	Overlapping distance at edges between contour and zigzag patterns
d_2	Overlapping distance at edges between parallel patterns
v_t	Travel speed
v_w	Wire-feed rate
W_t	Waviness
E	Deposition efficiency
θ	Vertex angle
L	Void length
Δh	Deviation between the target and actual height at the junction
λ	Empirical weight
A_{void}	Void area
\vec{N}_{RUF}	Normal vector of a point in the robot user frame
\vec{V}_{RUF}	Initial welding torch orientation in the robot user frame
P_{RUF}	A point in the robot user frame
θ_x	Rotation angle of the positioner along the x-axis
θ_z	Rotation angle of the positioner along the z-axis
R	Rotation matrix (3×3)
d	Translation matrix (3×1)
$H_{F_2}^{F_1}$	Homogeneous transformation matrix (4×4) of frame F_2 respects to frame F_1
A	Euler's angles of the welding torch, along the z-axis
B	Euler's angles of the welding torch, along the y-axis
C	Euler's angles of the welding torch, along the x-axis
\vec{N}	Normal vector
I_i	Centroid of the current cross section
I_{i+1}	Centroid of the next cross section
SP	Slicing plane
G	Guessed point

\vec{V}	Angle vector that is composed by I_t and I_b
γ	Angle between the normal vector and the angle vector
β	Limit angle (constant)
h'	Nominal moving distance
h'_{min}	Minimum height within a CAD slice
h'_{max}	Maximum height within a CAD slice
h_{min}	Minimum height that can be deposited
h_{max}	Maximum height that can be deposited
d_{max}	The maximum measured diameters
d_{min}	The minimum measured diameters
OV	Ovality

Abbreviations

ALC	Arc length correction
AM	Additive manufacturing
ANN	Artificial neural network
ASCII	American Standard Code for Information Interchange
AWS	American Welding Society
BCM	Beaded cylinder morphology
CAD	Computer-aided design
CAM	Computer-aided manufacturing
CMOS	Complementary metal oxide semiconductor
CMT	Cold metal transfer
CMT-ADV	CMT advanced
CMT-D	CMT dynamic
CMT-P	CMT pulse
CMT-PADV	CMT pulse advanced
CNC	Computer numerical control
DIN	Deutsches Institut für Normung e.V.
e.g.	for example
EBF ³	Electron-beam freeform fabrication
FDM	Fused deposition modelling
GMAW	Gas metal arc welding
GRM	Gouging region morphology
GTAW	Gas tungsten arc welding
i.e.	that is
ISO	International Organization for Standardization
LMD	Laser metal deposition
MAG	Metal active gas
MAT	Medial axis transformation
MIG	Metal inert gas
PAW	Plasma arc welding
PC	Personal computer
PUF	Positioner user frame

PWF	Positioner world frame
RUF	Robot user frame
RWF	Robot world frame
SCARA	Selective compliance assembly robot arm
SLM	Selective laser melting
SLS	Selective laser sintering
Std.	Standard deviation
TCP	Tool center point
TIG	Tungsten inert gas
USB	Universal Serial Bus
UTS	Ultimate tensile strength
WAAM	Wire-arc additive manufacturing
WLAM	Wire and laser additive manufacturing
YS	Yield strength

Contents

1. Introduction.....	22
1.1. Motivation	22
1.2. AM categories and process description	23
1.3. Literature review	26
1.3.1. Weld bead modelling.....	26
1.3.2. Surface roughness and staircase effect	28
1.3.3. Defects and imperfections in WAAM	29
1.3.3.1. Residual stress and deformation.....	29
1.3.3.2. Uneven weld bead geometry	30
1.3.3.3. Porosity	31
1.3.3.4. Weld bead humping	32
1.3.4. Tool path strategy	32
1.3.4.1. Tool path strategy for light-weight structures.....	32
1.3.4.1. Tool path for complex functional structures	35
1.3.5. Mechanical properties.....	36
1.3.6. Shielding gas.....	37
1.4. Aims and outlines of the thesis.....	38
1.4.1. Research gaps	38
1.4.2. Main contributions.....	39
1.4.3. Thesis outline.....	40
2. Robot-based WAAM system, testing devices and materials.....	42
2.1. Introduction and scope of the chapter	42
2.2. The cold metal transfer technique	43
2.2.1. Description of the pure CMT technique	43
2.2.2. CMT and feasibility in cladding application	43

2.2.3.	Synergic lines and arc length correction.....	44
2.2.4.	Equipped Fronius welder.....	45
2.3.	Robot system.....	46
2.3.1.	ARC Mate 100iC/12 robot arm.....	46
2.3.2.	FANUC positioner.....	47
2.3.3.	Robot controller and robot language generation.....	47
2.3.3.1.	R-30iB controller.....	47
2.3.3.2.	Offline robot program generation.....	48
2.3.3.3.	Coordinated motion control.....	50
2.4.	Testing and measuring devices.....	50
2.4.1.	Microscope.....	50
2.4.2.	Metrology equipment.....	51
2.4.3.	Uniaxial tensile testing machine.....	52
2.5.	Materials.....	52
3.	Multi-bead overlapping models.....	54
3.1.	Chapter introduction.....	54
3.2.	Establishment of multi-bead overlapping models.....	54
3.3.	Validation of the proposed overlapping models.....	59
3.4.	Performance of the developed overlapping models.....	60
3.5.	Summary of findings within the chapter.....	61
4.	Tool path generation for lightweight structures.....	62
4.1.	Chapter introduction.....	62
4.2.	Waviness and deposition efficiency.....	63
4.3.	Establishment of Eulerian paths.....	64
4.4.	Solutions for void filling in junctions.....	66
4.4.1.	A geometric solution for void filling.....	66
4.4.2.	Machine learning approach for void filling.....	70

4.4.2.1.	Tolerance for the shifting distance	70
4.4.2.2.	Training an artificial neural network with experimental data	70
4.5.	Evaluation of tensile properties	72
4.6.	Experimental results of the tool path generation for lightweight structures	73
4.6.1.	Evaluation of waviness and effective wall thickness.....	73
4.6.2.	Evaluation of the geometrical void filling criterion.....	74
4.6.3.	Performance of the ANN	76
4.6.3.1.	Tolerance.....	76
4.6.3.2.	Training ANN with experimental data.....	77
4.6.3.3.	The determination of an optimal training data set	78
4.6.4.	Tensile properties.....	80
4.6.5.	Realization of the proposed method for rib-web structures.....	81
4.7.	Discussion of the proposed tool path for rib-web structures	83
4.8.	Summary of chapter findings	84
5.	Multi-axis deposition for WAAM processes	86
5.1.	Introduction of the chapter	86
5.2.	Welding position for WAAM.....	86
5.3.	Multi-axis control for FANUC robot	87
5.4.	The decomposition algorithm.....	91
5.5.	Experimental results for the multi-axis deposition strategy	95
5.6.	Summary of chapter findings	97
6.	Tool path generation for curved thin-walled structures with shrinkage compensation	98
6.1.	Chapter introduction.....	98
6.2.	Examined geometries	99
6.3.	Multi-axis deposition with layers of non-uniform thickness.....	99
6.3.1.	Tool path generation by means of the adaptive slicing algorithm of CAD geometry.....	99

6.3.2.	Deposition of a non-uniform thickness layer.....	102
6.3.2.1.	The relationship between weld bead geometry and travel speed.....	102
6.3.2.2.	The correlation between the tube curvature and diameter	104
6.3.3.	Multi-axis programming of the welding robot	105
6.4.	Macrostructure and dimensional accuracy of the welded hollow sections	106
6.4.1.	Bonding quality and waviness (destructive test)	106
6.4.2.	Geometric accuracy (non-destructive test)	106
6.4.2.1.	Surface deviation between actual geometries and target geometries.....	106
6.4.2.2.	Ovality of welded hollow sections	107
6.4.2.3.	Reproducibility of metal parts.....	107
6.5.	Off-line compensation approach for material shrinkage and distortion	108
6.5.1.	The evolution of part geometry	108
6.5.2.	Compensation strategy.....	109
6.6.	Experimental results of tool path generation for curved thin-walled structures ..	110
6.6.1.	Relationship between weld bead geometry and travel speed, and computed CAD model	110
6.6.2.	Tool path generation and deposition performance	112
6.6.3.	Evaluation of the macrostructure and dimensional accuracy of welded hollow sections	115
6.6.3.1.	Macrographs and the waviness of curved thin-walled structures	115
6.6.3.2.	Geometric accuracy between actual geometries and target geometries..	116
6.6.3.2.1.	Surface deviation between actual geometries and target geometries	116
6.6.3.2.2.	Ovality of welded hollow sections.....	119
6.6.3.2.3.	Reproducibility of metal parts	119
6.6.4.	Compensation of shrinkage and distortion for curved thin-walled structures	119
6.6.4.1.1.	Evolution of part geometry during welding.....	119
6.6.4.1.2.	Compensation strategy.....	121

6.7.	Discussion of the developed tool path generation and the compensation strategy	123
6.7.1.	Discussion of the continuous deposition strategy and variable wall thickness	123
6.7.2.	Discussion of the compensation strategy	124
6.8.	Summary of chapter findings	125
7.	Summary of the main findings and possibilities for future research	127
8.	Publications.....	132
9.	Literatures	133
10.	Appendices	146

1. Introduction

1.1. Motivation

The Additive manufacturing (AM) technique is an unconventional manufacturing process, which creates physical objects from computer-aided design (CAD) models. Since Charles Hull patented the first AM machine [1], namely the stereo lithographic apparatus, AM technology has continued to experience significant development. The revenue forecast is expected to reach \$35.6 billion for all AM products and services worldwide in 2024 [2]. In the past, this technique was applied as a rapid prototyping manufacturing method during the product development phase due to time and cost reduction [3, 4]. Recently, AM products have been used directly for actual applications in many sectors such as aerospace [5, 6], the automotive [7, 8] and maritime [9] industries, civil construction [10, 11], footwear [12] as well as the biomedical industry [13–15]. This diverse evolution is possible because the AM technique offers several advantages, such as small batch production, freeform design [16], lead time reduction [17], and low buy-to-fly ratios [18] as compared to conventional manufacturing processes.

When it comes to conventional manufacturing methods, the production of large and complex metallic structures is completed by one-piece precision casting, forging, or the more popular option of machining from billets. For small batch production, these methods experience high production costs, tooling costs, waste material, and long lead-time. As such, new manufacturing methods should replace the traditional processes in order to produce complex metallic parts of medium and large sizes with low costs. Additional benefits would include less waste material, and a small lead-time. The wire-arc additive manufacturing (WAAM) process is a highly suitable candidate for manufacturing due to its high deposition rate, large working space as well as its low capital and operational costs [19]. Although many studies have been carried out, none have yet been able to successfully implement a WAAM system that constructs lightweight structures and complex functional parts. Therefore, there is still room for improvement and development.

As can be seen from Fig. 1, there are three steps in an AM process. Firstly, a 3D model is designed in a computer-aided design (CAD) software. In the next phase, the CAD model is sliced from the bottom to the top to get cross sections. Tool paths are then established from these cross sections and converted into machine language, which is included within computer-aided manufacturing (CAM). Lastly, within the third phase, metal parts can be produced.

This thesis mainly addresses CAM programs that manufacture lightweight structures and complex functional parts produced by WAAM processes. The proposed methods begin with CAD models and end with near-net shaped metal parts.

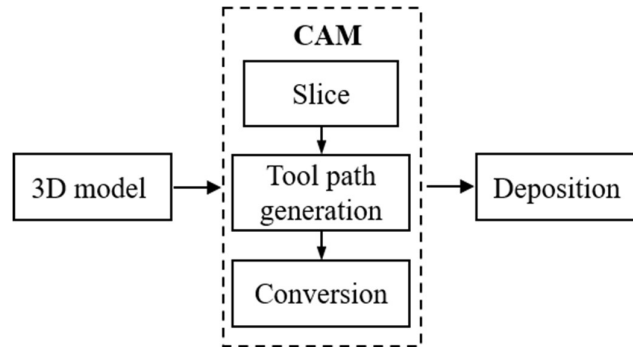


Fig. 1 The three phases of an AM process

1.2. AM categories and process description

In general, the AM technique uses a heat source to create fully dense components. Based on the type of material, AM technology is categorized into two main groups: powder-based and wire-based. The powder process utilizes different techniques including selective laser melting (SLM) [20, 21], selective laser sintering (SLS) [22], and laser metal deposition (LMD) [23]. The wire feed system includes wire and laser additive manufacturing (WLAM) [24], electron-beam freeform fabrication (EBF³) [25, 26], and WAAM [27]. Besides the processes for metallic materials, FDM (fused deposition modelling) is a well-known process to produce 3D components from thermoplastic materials and polymer-based composites [28–31].

The properties of various processes make them suitable for specific applications. Power-based processes, such as SLM, can build up fully functional products with high surface quality. The powder melting process takes place in a closed chamber filled with argon or nitrogen, which can limit the working space. The size of the powder is within the range of 15-45 μm [32] and the layer thickness is within the range of 20-100 μm [33]. Capital and material costs for these processes are relatively high and so have low deposition rates [34] and high production costs [35]. Powder-based techniques are therefore suitable for small components with high complexity. In contrast, wire-based processes experience a higher layer thickness ($\geq 900 \mu\text{m}$) [36] with an uneven weld bead geometry. These techniques consequently result in a rough surface quality, high deposition rate as well as a near-net shape.

Fig. 2 presents a schematic diagram of the wire-feed AM processes, which all use wire as feedstock. The heat source can be an electric arc, laser beam, or electron beam. WLAM uses a

laser beam to create a melt pool on the base material, where the wire is directed toward the molten pool laterally, and the metal liquid solidifies into a bead when the laser beam or the substrate is moved. The melt pool is protected from oxidation and contamination by a shielding gas, such as argon or helium. This technique is able to manufacture a few metals and alloys, but the energy efficiency is only about 10% [26].

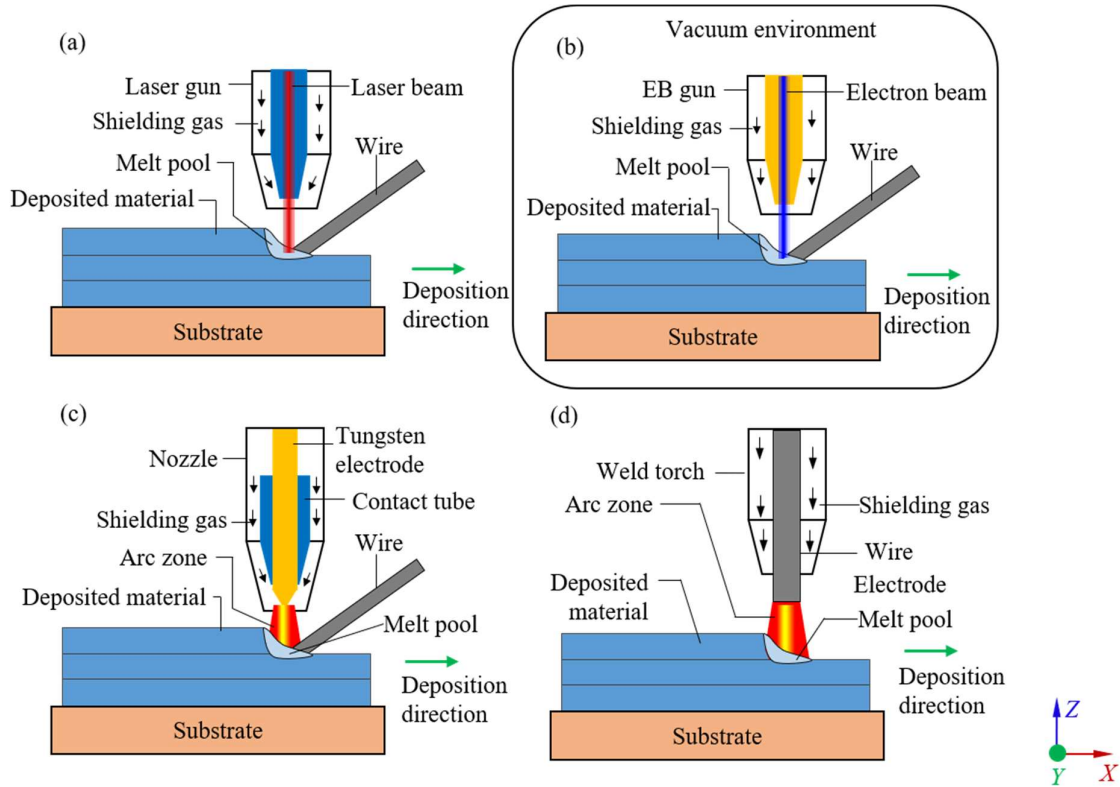


Fig. 2 A schematic diagram of the wire-based technique: (a) WLAM; (b) EBF³; (c) GTAW additive manufacturing; (d) GMAW additive manufacturing

EBF³ utilizes a high-energy electron beam to melt the base material and the wire-feed stock. Dense components are fabricated by depositing the welding wire on the substrate. The manufacturing process takes place in vacuum chamber, wherein shielding gas is not required but the working envelope is limited. Akin to WLAM, EBF³ works effectively with a wide range of materials, including reflective alloys. This technique reveals a significantly higher power efficiency (90%) [26].

WAAM uses a fusion welding process as a heat source, such as gas tungsten arc welding (GTAW), plasma arc welding (PAW), and gas metal arc welding (GMAW). This GTAW technique is also known as tungsten inert gas (TIG) welding. The electric arc is produced between a non-consumable tungsten electrode and the base material to create a melt pool.

During this process the wire is fed towards the melt pool. The weld bead is protected from oxidation and contamination by a shielding gas, such as argon or helium. Like GTAW, PAW also uses a non-consumable tungsten electrode to create an electric arc. However, this electric arc is not directly used for welding. There are two gas channels in the PAW nozzle – one for shielding the welding area and another for jetting gas plasma into the electric arc in order to create a plasma arc. Due to the ionized state of the gas, temperatures can exceed more than 28,000°C. GMAW differs from other welding techniques due to its use of a consumable wire electrode to melt and deposit the feedstock. The wire feeds towards the welding surface perpendicularly and the shielding gas flows through the nozzle to protect the welding area. The GMAW is often chosen to implement within a WAAM system due to its many benefits, including versatility, reliability, high thermal efficiency, and large working space. The arc efficiency and travel speed of GMAW is also much higher than those of GTAW and PAW [37]. The working range can be extended by mounting GMAW hardware with robotic automation, a relatively easy procedure. The GMAW-based WAAM process is an advantageous choice when producing metal components with medium and large sizes. The process has low production costs, high deposition rates (up to 10 kg/h) [38, 39], and a large working space (up to 12.5 m) [40]. The WAAM process is therefore highly suitable for building bulky parts [41].

During the metal transfer process, the traditional GMAW procedure experiences four primary modes: short-circuit transfer, globular transfer, sprayer transfer, and the pulse-spray transfer mode. Each mode has its own distinct advantages. Details of each mode are summarized below [42]:

❖ Short-circuit transfer mode:

The metals of electrode tips are melted by an excessive current when the electrode touches the base material and short-circuits at the frequency of 20-200 Hz. This is considered a low-energy mode and can be used for all weld positions with thin materials.

❖ Globular transfer mode:

This mode occurs with active gases (e.g., CO₂) at a low welding current. The droplet sizes are usually larger than the electrode diameter being used. Due to its low viscosity, this mode is better suited to welding procedures that require flat and horizontal positions rather than vertical and overhead positions.

❖ Spray transfer mode:

Akin to the globular transfer mode, the spray transfer mode produces a large molten pool, and is usually used for thick materials at flat and horizontal welding positions. This mode sprays tiny molten droplets (smaller even than the electrode diameter) which detach onto the base materials. Unlike the short-circuit transfer mode, spray transfer occurs continuously by using a high current and voltage with argon as the main shielding gas.

❖ Pulse-spray transfer mode:

The pulse-spray transfer mode is a modification of the spray transfer mode. This technique is achieved by controlling the peak current and voltage at a frequency of 30-400 Hz. A droplet transfers from the electrode to the weld puddle within each cycle. By reducing energy input, this mode can mitigate distortion and prevent burn-through.

1.3. Literature review

1.3.1. Weld bead modelling

AM parts are an integration of single weld beads, which is achieved by moving a metal trail on the base material. Therefore, weld bead geometry is an important factor in the tool path planning process. A comprehensive model of weld bead geometry will provide better information as to reduce failures, leading to a potentially stable process and increasing the geometric accuracy of the fabricated parts.

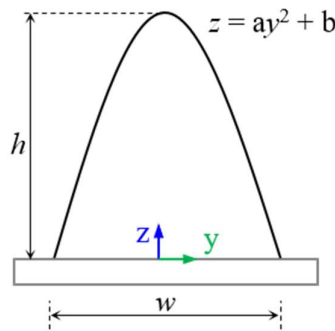


Fig. 3 A schematic of a cross section of single weld bead, as reported in Ref. [43]

The melt pool size plays an important role in regards to mechanical properties and the surface quality of metal parts [44]. For instance, melt pools that are too large result in rough surfaces, while those that are too small lead to incompetent bonding. High-strength bonding among adjacent layers demands a melt pool of a sufficient size, one that allows for existing top layers to re-melt.

In the GMAW-CMT process, which is introduced later in section 2.2, a cross section profile of a single bead is mathematically modelled as a parabola, cosine, or arc [45]. Among the latter, the parabolic profile shows the best fit to real weld bead profiles [46], as shown in Fig. 3. The bead dimensions can be represented using height (h) and width (w).

Since weld bead geometry plays an important role in the tool path planning process, it is essential to establish the relationship between welding parameters and weld bead geometry. Suryakumar et al. [43] established algebraic equations to compute the bead height and width from welding parameters such as wire diameter, wire-feed rate, and travel speed. Besides mathematical models, the weld bead geometry can also be predicted by using artificial neural networks (ANNs) [46–48]. Several studies used a supervised machine learning approach to make predictions from rule-based learning with experimental training data. In this context, an ANN represented the relation between bead geometry and process parameters. The process parameters were adjusted to achieve the desired bead geometry. Other groups of researchers used an online learning approach to establish rules between process parameters and weld bead geometry. Heralic et al. [49] integrated a 2D scanner into a WLAM system to determine the distance between the laser gun and the deposition surface during deposition. The deviation in layer height is controlled by iterative learning approach within scanned data. The proposed algorithm adjusts the travel speed in each subsequent layer to maintain a constant distance between the laser gun and the deposition surface. Another work of note was executed by Aviles-Vinas et al. [50], who utilized the ANN approach to control weld bead geometry. The process of generating training data and acquiring the seam geometry automatically took place in real time while the welding system learned by itself how to produce the desired weld seam for the GMAW process.

A single weld bead width has limits to a certain value, e.g., [1.0-2.0] mm [39]. To deposit thicker components, multiple overlapping weld beads and oscillating patterns can be employed [51, 52]. The step-over rate is the overlapping rate between two adjacent weld beads, in WAAM the step-over rate is defined as the distance of the welding torch between two parallel weld seams. Suryakumar et al. [43] and Ding et al. [45] utilized an overlapping approach when ascertaining an optimal step-over rate of 0.67 and 0.738, respectively. However, it should be noted that contour beads grow slower in height than inner beads due to the fact that the boundary contour overlaps only on one side with other weld beads [53]. To overcome this problem, Flores et al. [53] proposed a heuristic method to level the deposited layer up in the manufacturing of solid structures. The showcase was deposited by following hybrid tool path patterns as well as

the addition of an extra contour bead to every two layers. As a metal part requires the deposition of several layers, uneven layer surfaces may lead to accumulated errors along the growth direction, resulting in unstable deposition after few layers [54]. Therefore, it is essential to establish robust models.

1.3.2. Surface roughness and staircase effect



Fig. 4 Stair steps among adjacent layers

When the layer marks become distinctly visible on the surface of the parts, giving the perception of a staircase, this phenomenon called staircase effect.

For power-based processes, e.g., SLM, the layer thickness that occurs is less than 0.1 mm and metal parts do not suffer significantly from the staircase effect. However, this effect influences the geometric accuracy of metal parts considerably in wire-based processes due to a large layer thickness. Many studies have been conducted to mitigate these issues by adjusting the layer thickness, based on a part's contours [55–57]. A weld bead cross section in wire-based AM processes represents a parabolic shape with a bead height range of about 1.0 to 2.0 mm [39]. As a result, stair steps can emerge among adjacent layers (Fig. 4) making the WAAM process suitable for building near-net shape parts. Post-processing, e.g. milling, must be applied to work surfaces in order to ensure accurate dimensions as well as an attractive appearance. The removal may yield a low deposition efficiency. Almeida and Williams [58] reported that the deposition efficiency for single bead walls is about 80% with the GMAW-CMT process for Ti-6Al-4V. This same material reveals higher wire-plasma deposition rates, with an average of about 93%. Surface waviness could be captured on single thin-walled parts with a range of around 0.35-1.51 mm [59].

1.3.3. Defects and imperfections in WAAM

1.3.3.1. Residual stress and deformation

In WAAM, metal parts experience periodic heating, melting, evaporation, solidification, and cooling. Due to thermal expansion and phase changes, deposited volumes change from a liquid state to solid state before dropping to room temperature. The microstructure cannot respond to these changes during the thermal conduction process, leading to an irregular thermal expansion and contraction of material. These phenomena can cause residual stresses, which inevitable in welded parts [60–62], may result in the deformation, distortion, or even cracking of metal parts, especially when the part size increases [63]. Shrinkage is considered as the reduction of the material volume during cooling without external forces [64]. The shrinkage rate depends on a specific location and time within a metal part [65]. Deformation and distortion can be mitigated with the application of a few simple methods, including:

- the use of fixture and jig to clamp substrates [66],
- preheating substrates [67],
- letting welded products cool to room temperature in the fixture [66], and
- rolling and peening [68–70].

Some research groups reported that less thermal input and smaller weld beads can reduce deformation and distortion due to yielding less residual stresses [60, 71, 72]. Colegrove et al. [60] used finite element models to predict heating and cooling cycles during WAAM process. Thermo-mechanical properties were examined by means of a single wall. The results determined that top layers yield more longitudinal residual stresses, and that a high heat input promotes significant residual stress and subsequently distorts the wall. CMT technology, on the other hand, can reduce thermal input by 35 – 40% [73], thereby producing less deformation and residual stresses [74]. A decreasing wire-feed rate leads to a lower heat input [75], therefore making it essential to use a small wire-feed rate and to keep the travel speed as high as possible so as to minimize the thermal concentration. To produce large parts with the WAAM process, Denlinger and Michaleris [76] proposed an approach wherein two parts were deposited onto both sides of a substrate in order to neutralize residual stresses on the substrate. By doing so, the maximum longitudinal bending distortion is decreased by 91%. However, residual stresses deform not only the substrate but the metal parts as well. This strategy is probably suitable to produce rib-web structures when the contact between parts and substrates is significant. During the production of complex functional structures, the metal part is created above the substrate and can be deformed and distorted.

Though substantial efforts have been implemented, material shrinkage and distortion cannot be avoided. Therefore, a compensation strategy is needed. Closed-loop monitoring systems have been developed to control process parameters, ensuring the geometric accuracy. For instance, a vision system [50, 77, 78] was applied to monitor the melt pool during processing, which serves as a basis for adapting the input energy and deposition speed. A red line scanner was also used to maintain a stable distance between the laser source and deposited surface during the deposition process [49]. This scanner is not appropriate for hot-glowing surfaces which means scanning operations are performed after pausing the process for one minute. Therefore, blue laser technology is recommended for hot-glowing surfaces [79]. Shrinkage and distortion occur during the deposition process, during the time it takes parts cool down to room temperature. The feedback data from experiments contains noises, which can lead to inaccurate control input. However, an online process cannot compensate for material shrinkage and distortion within fusion welding. An offline process would be better suited, one in which the tool path is adjusted according to the geometric deviation obtained after the deposition. This approach has been developed for SLM process [80]. Within this current work, the geometric deviation is compensated by modifying the CAD model so that the metal parts shrink and distort in such a way that they assume the desired geometry after cooling. The properties of the powder-bed system are different from those of the WAAM process, particularly in terms of the support structures utilized as well as the heat flux and cooling rates. Due to these differing properties, the existing method cannot be applied directly to the WAAM process. The simulation approach can be used to obtain geometric deviation. Finite element models have been developed for the prediction of shrinkage and distortion [81, 82] in WAAM. However, these models were validated and tested on simple geometries and the computational cost was high [81]. Establishing a numerical model to predict the shrinkage rate in layer-wise manufacturing is expensive. As aforementioned, the shrinkage rate depends on the size, shape, and specific position of AM parts, hence existing numerical models might not be applicable for complex structures in WAAM.

1.3.3.2. Uneven weld bead geometry

When it comes to the GMAW process, weld bead geometry typically follows a profile akin to the one shown in Fig. 5, with a significant height difference between the start and end position. The penetration is lower at the starting point due to heat loss and so the weld bead is higher than during steady-state welding. Towards the end position, a slope is observed due to the weld

pool [83]. The accumulation of uneven geometries might lead to geometrical defects, underfills, and a low surface quality.

Many strategies have been proposed to cope with the problem of uneven weld beads. One of these strategies included a hybrid process that manufactured metallic parts using both additive and subtractive processes [52, 84]. During this process, a milling operation was used to mill the surface between two subsequent layers. Every surface was flattened after a layer was deposited, thereby avoiding an accumulation of errors. Zhang et al. [83] suggested a method to improve deposition accuracy by controlling the welding parameters in the start and end portions of a weld track. For instance, Zhang began the welding process with a higher speed and decelerated to a constant velocity. The velocity decreased slightly as the process reached the end of the track. In addition to these strategies, a suitable tool path strategy can also be a measure for uneven weld beads, which is detailed in section 1.3.4.

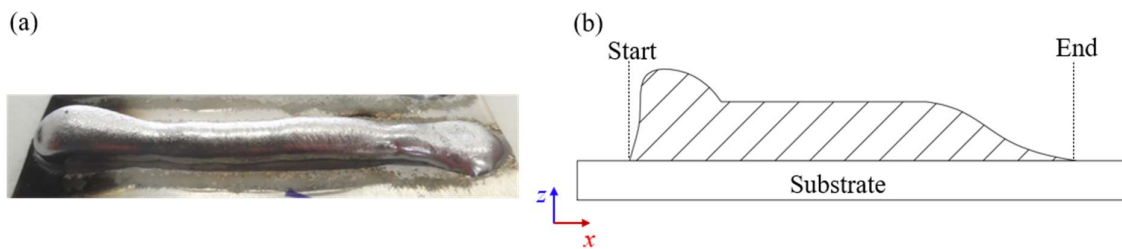


Fig. 5 An uneven weld bead: (a) real weld bead (a) and (b) schematic cross section of a weld bead

1.3.3.3. Porosity

Porosity refers to impurities such as a blowhole, wormhole, pore, or bubble in solidifying weld metals [66]. This imperfection reduces the mechanical properties of AM products [85]. For instance, increased porosity level leads to decreased stiffness. Damages, such as micro-cracks, may occur when put under pressure, degrading the mechanical strength of the product. Lateral expansion that occurs under compression can promote an opening mode or shearing effect, which reduces mechanical properties [86]. Despite the manner in which it degrades mechanical properties, porosity has a significant advantage: it promotes the permeability of porous structures within an injection-molding die [87]. Due to the evolution of hydrogen during solidification, porosity is inevitable when depositing aluminum and its alloys. Many studies have been conducted to investigate the mechanism of porosity development and to propose methods of minimizing porosity [88–90].

1.3.3.4. Weld bead humping

Humping is defined as the periodical undulation of weld metal on bead surfaces. This phenomenon may be caused by the momentum of the back flow of the molten pool (114, 124) along with a high welding travel speed [91], which limits the capacity of high-speed welding processes [91–93]. There are two humping morphologies in fusion welding processes: gouging region morphology (GRM) and beaded cylinder morphology (BCM) [94]. Fig. 6 depicts the two types of humps. For the GRM, open and unfilled fry spot occur in between the humping beads. The front of the molten pool experiences a large depression known as the gouging region. During the BCM process, the solidified metal bulges are connected by a narrow trail.

The humping phenomenon was investigated within CMT welding, wherein a high-speed deposition was utilized with the wire electrode as a mild steel (ER70S-6). It was found that the humps emerged at a travel speed of 0.6 m/min [95]. The front portion of the weld pool was prevented from backfilling due to the strong momentum of the backward flow, which caused the elongation and solidification of the wall jet, forming a valley in a humped weld bead.

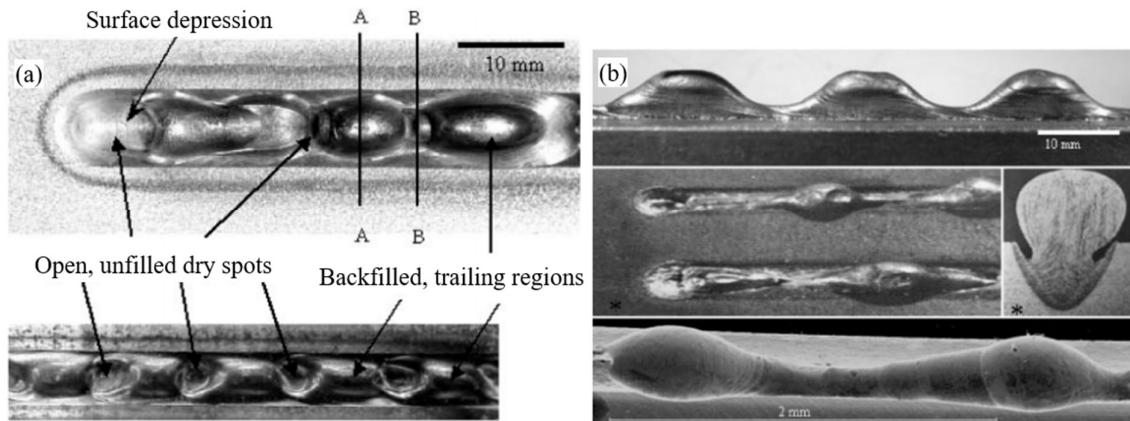


Fig. 6 Weld bead humping: (a) gouging region morphology and (b) beaded cylinder morphology, as reported in Ref. [94]

1.3.4. Tool path strategy

1.3.4.1. Tool path strategy for light-weight structures

The way of moving the weld torch is known as a tool path. This movement plays an important role in the geometric shape of weld bead, surface quality, mechanical properties, and productivity for WAAM. Fig. 7 illustrates a schematic of typical tool path patterns such as the zigzag, contour, and hybrid patterns. The zigzag pattern connects single paths from raster patterns [96] along the x- or y-direction, which results in continuous paths as well as a level of

movement efficiency that compares to other patterns [97]. Despite significant productivity, this pattern causes poor outline accuracy [98] and overfills at turning points [99].

The contour pattern, on the other hand, can tackle the drawbacks of the zigzag pattern, e.g., improving outline accuracy and avoiding overfills. However, gaps can result among adjacent beads and facilitate low movement efficiency when the contour pattern is offset at a specific distance [99]. Overall, the hybrid pattern seems to be the most promising, as it can deal with the disadvantages of the zigzag and contour patterns. For instance, the inner areas are filled by zigzag patterns to foster productivity and eliminate gaps among adjacent weld beads while the outer areas follow contour patterns to improve surface quality.

Due to the large working volume and high deposition rates, WAAM processes are applicable to components such as rib-web structures, which are predominantly used as lightweight aerospace structures. Rib-web structures are also found in the equipment used for heat, chemical and process engineering, where the ribs can be used to promote heat transfer. Forging and subsequent milling typically produce high-performance components. Forged ribs are made by forming work pieces between two dies, typically resulting in high tooling costs [100]. Rib-web structures are often manufactured by removing material from solid blocks, yielding a very high buy-to-fly ratio [101] and a lot of material waste. Using WAAM processes to manufacture lightweight structures would reduce material waste along with the number of machining operations. Investments into tooling and machinery would also be reduced as well as production lead-times. To summarize, the WAAM process has the potential to replace conventional manufacturing processes.

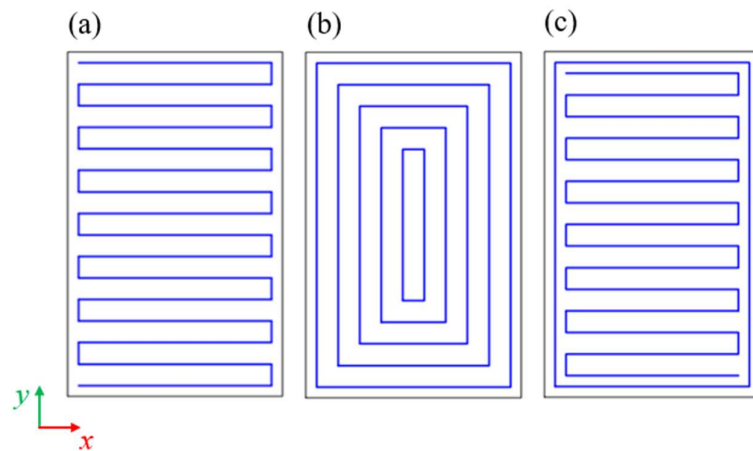


Fig. 7. A schematic of typical tool path patterns: (a) zigzag; (b) contour; (c) hybrid

Rib-web components are considered as lightweight structures, which consist of several connected ribs. The quality of the junctions between these ribs depends heavily on the deposition strategy. A direct crossing strategy [102] can cause imperfections such as the development of material peaks and deposition failures within junctions. In other words, the welding torch works on existing seams, and thus the number of layers deposited at a vertex of the rib-web structure is larger than necessary. A common remedy is to deposit one wall continuously, while the walls intersecting this wall are deposited discontinuously, i.e., the torch moves over the vertex depositing material but leaves out the vertex itself. Stopping and starting the welding motion at a vertex may cause binding errors. To deal with this issue, the torch may follow a fillet at the intersection point instead of overlapping its neighboring ribs [51, 103]. However, this strategy has a drawback since the generation of voids is possible. Contour patterns cause the intersecting area to enlarge, making the deposited material insufficient for this area, as shown in Fig. 8. The schematic shows a junction of three ribs, which have been manufactured from three weld passes and the contour pattern. One can clearly see a gap among the adjacent weld beads. Venturini et al. [104] proposed a strategy to deposit rib-web structures with single weld beads, with each rib requiring only one weld bead to be deposited. The tool path was modified in junctions to avoid voids and to deal with uneven weld beads. Another void correction method was proposed by Liu et al. [105], whom investigated start-shaped geometry. The study found that a void would develop between adjacent weld beads at a turning area if the turning angle is less than 58.65° . The distance between consecutive paths was much greater than normal but did not ensure an optimal overlapping rate, leading to a shortage of deposited material at the turning area. The turning point of the inner contour was modified, i.e., shifted towards the outer contour, to ensure a proper overlapping rate.

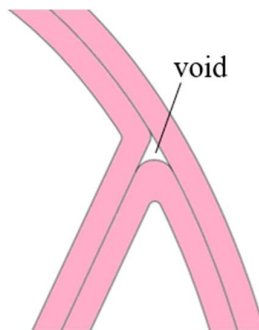


Fig. 8 A schematic of void formation among adjacent weld beads

As mentioned in the previous section, uneven weld beads should be avoided, as the uneven weld bead geometry can affect the production of thin-walled parts. Ma et al. [52] proposed in

their study that the welding direction alternates between adjacent layers. Another method to deal with uneven weld beads would be to reduce the number of welding passes in tool path planning. For lightweight structures, e.g., a rib-web structure, each layer can be represented by a graph. The multi-graph in Fig. 9 represents a schematic tool path for a rib-web component. The structure represented by this graph cannot be welded in a single continuous motion of the weld torch. In other words, if the torch can travel along each edge of the graph only once, the welding torch cannot start and end at the same vertex. Jumping to a different position and re-igniting the arc increases the danger of welding defects and under-fills. According to graph theory, the deposition process can be performed continuously if the tool path represents a Eulerian path [106], i.e., a graph in which a continuous trail exists that visits each edge only once. A connected graph is only considered Eulerian if all vertices have an even degree, and semi-Eulerian only if two vertices in the graph have odd degrees [107]. In graph theory, the degree of a vertex is the number of edges which meet at that vertex. Within rib-web structures, the degree describes the number of walls meeting at a vertex. Therefore, no Eulerian path exists within arbitrary rib-web structures. In this case, the welding torch starts and stops more than once per layer, which increases the probability for welding defects.

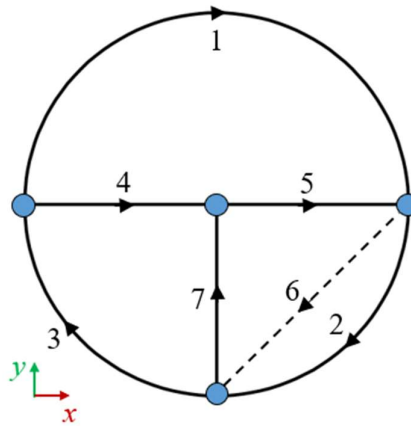


Fig. 9 A representation of a schematic tool path as a graph

1.3.4.1. Tool path for complex functional structures

Overhanging structures are not a challenging prospect within the powder bed systems, e.g., SLM, support materials are applicable therefore making the overhanging structures possible. In addition, plastic wire-based process, e.g., FDM, can add supportive materials in other solvent materials or in scaffold structures [108] which can be easily removed after deposition. These materials support the deposition process but do not add value to the parts. To reduce the use of supportive materials in the FDM process, a multi-axis deposition approach has been introduced

[109, 110]. While small overhangs are possible during the WAAM process, large overhangs are decidedly not. This is owing to the fact that scaffold structures as a means of support are not feasible [111]. However, overhang features can be produced with a multi-axis deposition, the welding torch is simply reoriented to coincide with the inclinations of a part's contours [112–116]. This strategy can enhance the part quality by preventing defects, such as the running of molten material due to gravity. It can also alleviate the staircase effect [112]. Many research efforts have been made to produce overhanging features in WAAM. By using the multi-axis deposition strategy, functional metal parts with overhanging features could be manufactured [114]. Each overhanging feature was deposited with a distinct position by means of a five axis CNC machine. A mathematical model was developed to estimate the height of subsequent layers from the geometry of the first weld bead. This model was confirmed by means of experimental data gathered through the deposition of 30-layer parts. However, the weld bead geometry can differ when increasing the number of deposited layers due to accumulative heat [117]. The geometric accuracy of printed parts was not investigated. For applications regarding civil engineering [118], each individual pipe was produced with a distinct direction by adding layers of constant thickness and avoiding out-of-position welds. The joint structures can be extended in many directions with customized diameters. The cross-section deviation is about ± 1 mm and the angular errors are less than $\pm 0.5^\circ$. The printed pipe can shrink longitudinally during the process and there was no evaluation of longitudinal errors. The concept of producing overhanging features with layers of irregular thicknesses was proposed by Ruan et al within powder cladding processes [119]. Hybrid manufacturing systems, such as additive and subtractive manufacturing, were used to fabricate these irregular layers. These are systems in which operations were integrated within a multi-axis machine. A nozzle deposited layers of identical thicknesses with constant process parameters. The inclined surfaces were produced by means of face-milling operations. This hybrid method ensured a controlled metal build up as material was always deposited on milled, flat surfaces. However, this method also revealed a few drawbacks, such as a longer processing time, more machinery costs as well as more waste.

1.3.5.Mechanical properties

To satisfy the strict requirements of engineering applications, AM parts are required to meet specific mechanical properties. Achieving such mechanical properties is a challenge in AM because of the addition of material. Furthermore, materials must also be weldable. The most used ones are as steels [120], aluminum alloys [121], and titanium alloys [122]. During WAAM processes, deposited metals are affected by a complex thermal history, i.e. heating, melting,

solidification, cooling, and local remelting [123, 124]. Many studies have been implemented with the goal of understanding the effects of process variables on microstructure and mechanical properties. These variables include shielding gas, deposition path and post-fabrication heat treatment. Caballero et al. [125] conducted a study on 17-4 PH stainless steel by WAAM using CMT technology. The work determined that the required tensile properties can be obtained by applying post-deposition heat treatment. Suryakumar et al [126] investigated mechanical properties on mild steels using GMAW-WAAM processes. The work found that hardness is not affected by thermal cycles, just the last few layers yield hardness variation. Tensile strength in all directions (vertical and horizontal) was homogeneous when the welding current was increased. Prado-Cerqueira et al. [120] compared the performance of GMAW and CMT in the construction of mild steel parts, and in terms of hardness and tensile strength. The experiment's results revealed that CMT technology allowed for homogeneous hardness and higher ultimate tensile strength. Sizova1 et al. [122] utilized hot forming components with WAAM products as pre-forms from the titanium alloy Ti-6Al-4V. It was determined that final components from WAAM pre-forms have properties similar to conventional forging process chains.

1.3.6. Shielding gas

It has been found that shielding gas composition plays an important role in fusion welding [127] since it affects heat transfer. Shielding gas protects the weld pool from atmospheric influences and maintains the stability of the arc. The weld pool and its surrounding areas oxidize when brought into contact with the oxygen in the air at high temperatures. Nitrogen and humidity in the air is also troublesome, as it can lead to pores in welded parts. Thermal input is affected by the shield gas, which influences the material transfer from the wire electrode into the molten pool, thereby affecting spatters and weld bead geometry as well [128].

The GMAW technique includes a metal active gas (MAG) process and a metal inert gas (MIG) process. The techniques are distinguished by the type of gas used. The MAG process is used for ferrous metals with a typical shielding gas composition of argon (Ar), oxygen (O₂), and carbon dioxide (CO₂). The proportion of one to another can affect the transfer mode, behavior of weld pool, penetration, and mechanical properties. It should be noted that pure Ar is unsuitable for steels due to an unstable arc and low thermal conductivity [129]. The use of pure CO₂ provides advantages such as greater penetration and low cost, but also carries with it disadvantages, such as a high amount of spatter and an unstable arc [130]. Therefore, a mixture of Ar with CO₂ and/or O₂ is preferable. Due to the low cost of CO₂ in comparison with O₂, a

mixture of Ar with 5-20% CO₂ is popular [131]. This mixture can provide a stable arc, and enhance penetration of the weld bead [132]. Increasing the CO₂ ratio results in less porosity [129], lower hardness and higher toughness [130, 131]. The MIG process, on the other hand, is famous for stainless steels and non-ferrous metals such as aluminum and titanium alloys. Argon and helium are the inert gases typically used for MIG welding. Pure Ar is used for the production of WAAM parts with aluminum and titanium [133, 134]. Oxidation of titanium alloys was discovered by Caballero et al. [135]. The authors found that oxidation occurs when temperature and exposure time are high enough. To reduce the reactivity of Ti with O₂, metal parts should be manufactured in an argon protective chamber [122]. For depositions with duplex stainless steels, a mixture of He and Ar is applied as the shielding gas [136]. A ratio of 25-75% He to 75-25% Ar leads to different weld seams. An increased percentage of He causes higher heat input and thus results in wider weld beads. Use of more He can enhance productivity but is more expensive than Ar.

1.4. Aims and outlines of the thesis

1.4.1. Research gaps

Although a significant effort has been made to realize the potential of WAAM, tool path strategies to produce complex and lightweight structures are still being developed and improved upon. Existing commercial CAM software is mostly for polymer materials and powder-based processes. Due to its distinct properties, this software cannot be directly applied to WAAM processes. Tool path strategy plays an important role in building capabilities, mechanical properties [137] and the accuracy of WAAM products [98]. Several challenges should be addressed when developing advanced process planning tools, including weld bead modelling and multi-axis deposition. Furthermore, tool path strategies have to be developed to produce both lightweight structures and curved thin-walled structures.

Multi-bead overlapping modelling: The weld bead geometry of single beads have been studied [43, 138, 139], and a metal component manufactured by depositing single beads side-by-side and layer-by-layer. In such cases, a multi-bead overlapping model seems to be appropriate. This overlapping model ensures proper fusion among adjacent weld beads and therefore smooth surfaces. Multi-bead models have been developed [43, 45] but none of them considered the edge contours, where weld beads have only a one-sided overlap. New multi-bead overlapping models are needed in order to improve the building ability and geometrical accuracy of additive parts.

Tool path strategy to produce lightweight structures: Lightweight structures, such as rib-web structures, consist of connected ribs. The deposition path does not always represent a Eulerian or semi-Eulerian path, so additive parts may suffer from uneven weld beads owing to an increasing number of weld passes. This is particularly true of GMAW process. When straight walls are deposited, the cross section area derives from a single bead geometry. At turning points, the cross section of a single bead is irregular and unpredictable [51], therefore the existing overlapping models are inapplicable in intersections and junctions occurring within rib-web structures. Moreover, single beads limit to a certain width, which means large walls are required for multi-bead depositions. Existing tool path strategies for lightweight structures also reveal drawbacks, indicating the need to develop a new tool path strategy.

Multi-axis deposition: Complex and large overhanging features are challenging for traditional WAAM processes, wherein materials are deposited in the x-y plane as Cartesian coordinates. Due to the complexity of support materials and scaffold structures, each overhanging feature should be detected and deposited with a distinct direction. A multi-axis deposition strategy can bring even more advantages. Therefore, a CAM program should be established that decomposes overhanging features and generates a multi-axis program for a robot system.

Tool path strategy to produce curved, thin-walled structures: Overhanging features can be produced, but a research gap still exists concerning the generation of curved, thin-walled structures and the compensation of shrinkage and distortion. An often-overlooked approach is one in which the deposition of nonuniform layers is combined with the adaptive slicing of curved, hollow profile sections. To create these irregular layers without milling operations, the deposition process requires precise control of weld bead geometry throughout the process parameters. The geometry of a weld bead in WAAM is a consequence of the process parameters, such as travel speed and wire-feed rate. Although many prediction models have been developed [43, 139–141], only single layers have been considered. Single layers cannot represent more complex geometries, since differences in temperature history affect weld bead geometry [117]. There is a pressing demand for a simpler model to estimate weld bead geometry that utilizes process parameters and takes thermal behavior into account. As aforementioned, a simulation approach, along with online compensation for shrinkage and distortion, is difficult, even infeasible. An offline compensation strategy in tool path planning is needed.

1.4.2. Main contributions

This thesis addresses all challenges mentioned in the previous section. The main novel contributions are summarized below:

- Multi-overlapping models are constructed to ensure the proper growth of part edges. Adopting an existing single bead model, the proposed algorithm uses mathematical models to realize overlapping models for hybrid patterns by determining the optimal distances between adjacent weld beads. This method paves the way for tool path planning for other AM processes, such as directed laser metal deposition.
- A continuous tool path strategy for the fabrication of lightweight structures is established by converting arbitrary graphs into Eulerian paths, which can bypass the effects of uneven weld beads. In addition, a new correction method is developed using an artificial neural network to evade voids at junctions. The impact of the developed method on surface quality and mechanical properties is also studied.
- A multi-axis deposition system for a robot based WAAM is set up. The developed method detects and decomposes overhanging features into subparts. Each subpart can be deposited with a distinct direction. The study proposes a neutral deposition position to mitigate the impacts of disturbances, requiring a kinematics of a robot system with two groups to be introduced.
- Further applications of multi-axis deposition are applied to produce curved thin-walled structures. A simple method is developed to construct a relationship between weld bead geometry and travel speed. Layers of irregular thicknesses can be produced without milling operations. These layers are deposited continuously to form a metal part. Geometric accuracy is ensured by an offline compensation strategy for shrinkage and distortion. The proposed manufacturing method can be a substitute for conventional processes to produce industrial applications, such as structural frames, wiring conduit, gas and fluid transportation, and vehicle frames.

1.4.3. Thesis outline

The structure of the present work is as follows:

Chapter 2 introduces the specifications of a WAAM system and other measuring and testing devices.

Chapter 3 presents multi-bead overlapping models for WAAM processes. Optimal distances between adjacent beads are determined from a volume approach. The proposed models are verified with different process parameters.

In chapter 4, a tool path strategy for lightweight structures is developed. Arbitrary cross sections are transformed into a Eulerian path, which is considered as a continuous tool path in order to

avoid the effect of uneven weld beads. Due to a larger volume at junctions, an adaptive correction is developed based on a machine learning approach. The proposed approach is validated through the production of a rib-web structure.

Chapter 5 illustrates a multi-axis deposition strategy. The growth direction of subparts is identified with which the welding torch should align. The welding position is controlled by neutral deposition position. Kinematics of the FANUC system is introduced, and the neutral position is maintained by manipulating the positioner and the orientation of the torch. The multi-axis deposition strategy is examined by the construction of an overhanging feature.

Chapter 6 introduces a novel method to manufacture curved thin-walled structures. The procedure to generate nonuniform layers is presented. The proposed method is validated through experiments to examine the building capacity and performance of the compensation strategy.

Chapter 7 draws a summary of the main findings and future research orientation.

2. Robot-based WAAM system, testing devices and materials

2.1. Introduction and scope of the chapter

The term *industrial robot* is defined by the International Organization for Standardization (ISO) as an automatically controlled, reprogrammable, and multipurpose manipulator. The industrial robots can have two or more axes, and they are either fixed or placed on a mobile platform [142]. According to the mechanical structures, the industrial robots are categorized into four groups, including Cartesian robots, Selective Compliance Assembly Robot Arm (SCARA) robots, articulated robots, and parallel robots.

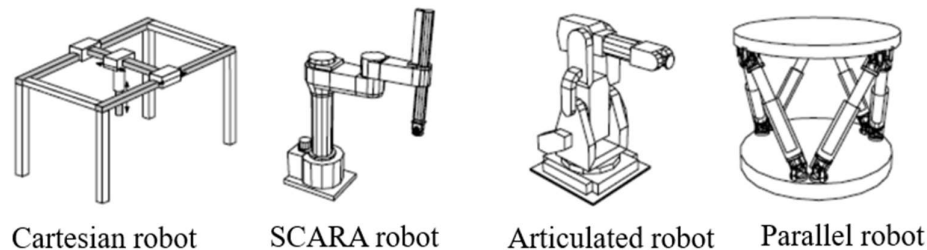


Fig. 10 Robot classification by the mechanical structures, as reported in Ref. [142]

To define the position and the attitude of a robot, a frame of reference must be defined. A world frame is predefined for each robot in the Cartesian coordinate system as the default frame. For an industrial robot, the end effector is a device typically mounted onto the tool plate of the robot's wrist to perform specific tasks. Depending on the required function, the end effector can be a gripper, welding torch, spray gun, cutting tool, or measuring device. The position of the end effector is defined as the value of x , y , and z in a Cartesian coordinate system and in Euler's angles [143]. The term *tool center point* (TCP) is used to represent the position and orientation of the end effector. Industrial robots are a combination of many actuators, e.g., servo motors. To manipulate the end effector, robot joints are coordinated simultaneously. Besides the world frame, a joint frame is introduced to define robot joints. The robot's attitude and position are defined by angular displacements. In this work, these two frames are used to describe the position and orientation of a welding torch as well as the angle of a positioner.

Among the robots in Fig. 10, the articulated robots reveal the most versatile features in fusion welding applications [144]. These features comprise of a large working space, flexibility, a light weight, and a low price. Such advantages make this type of robot a popular choice for varying projects, this current academic paper included. Therefore, articulated robots were chosen to drive the welding torch in the WAAM system.

The objective of this chapter is to specify the hardware specifications used in this monograph, which includes a FANUC serial robot coordinated with a positioner and a Fronius welder with CMT technology. The content is extended with the procedure for offline programming for the robot based WAAM system. Besides the WAAM system, other measuring and testing devices are also introduced in this chapter.

2.2. The cold metal transfer technique

2.2.1. Description of the pure CMT technique

A new GMAW technique was introduced in 2004 by Fronius International GmbH called cold metal transfer (CMT) technology [145]. This technique is a versatile fusion welding method that can be used for many metals, alloys, and even dissimilar metals. CMT technology derives from the short-circuit transfer mode of the traditional GMAW process and retracts the electrode automatically by a feeder when short-circuiting at about 63-160 Hz. At each cycle, the electric arc reignites and the electrode feeds towards the molten pool, causing the electrode to be deposited drop-by-drop.

There is no electromagnetic force due to a drop in the welding current during the metal transfer process, thereby reducing spatter [146, 147]. Each droplet undergoes a three phase cycle: peak current phase, background current phase, and short-circuiting phase [145]. In the first phase, the arc voltage is constant, allowing a current pulse to appear and create the molten pool from which a droplet forms. During the next phase, the current drops considerably, in fact almost near zero, so as to avoid the globular transfer mode. In the final phase, the arc voltage falls to zero and the wire-feeder retracts the electrode, stimulating the detachment of the droplet into the molten pool. Due to the complex waveform of the welding current, the CMT process is controlled via a digital control unit. The welding energy (voltage and ampere) is controlled in cooperation with the wire-feed rate in the CMT technique. In other words, droplet sizes are manipulated through the wire-feed rate, and the welding energy is the resultant.

2.2.2. CMT and feasibility in cladding application

Besides the pure CMT mode, Fronius International GmbH has also recently developed a type of CMT technology with different droplet transfer modes for welding applications such as CMT pulse (CMT-P), CMT advanced (CMT-ADV), CMT pulse advanced (CMT-PADV), and CMT dynamic (CMT-D) [148]. Amongst them, CMT-P, CMT-PADV, and CMT-D reveal more heat input and arc input and are therefore not suitable for additive manufacturing processes [74,

149]. On the other hand, CMT-ADV reported less heat input than the pure CMT mode due to polarity reversal in the short-circuit phase.

Advantages of the CMT technique include low heat input into the base material and robust weld bead geometry. As reported, thermal inputs can reduce by 35 – 40% in comparison with the traditional GMAW process [73, 150]. CMT yields low penetration, low dilution and a wide weld bead [75, 151] with a maximum deposition rate of up to 5.5-6.0 kg [74]. In addition, the dilution and penetration of the process can be controlled by changing the synergic line and arc length correction [146].

2.2.3. Synergic lines and arc length correction

Synergic lines refer to a welding program which tunes the parameters according to voltage, wire-feed rate, shielding gas, or material thickness. For instance, the welding powder will be calculated automatically based on selected wire-feed rate, shielding gas and material thickness. New synergic lines are required for different materials and wire diameters, a task undertaken by Fronius International GmbH, who develops and installs the lines. As such, the number of synergic lines available are limited [149].

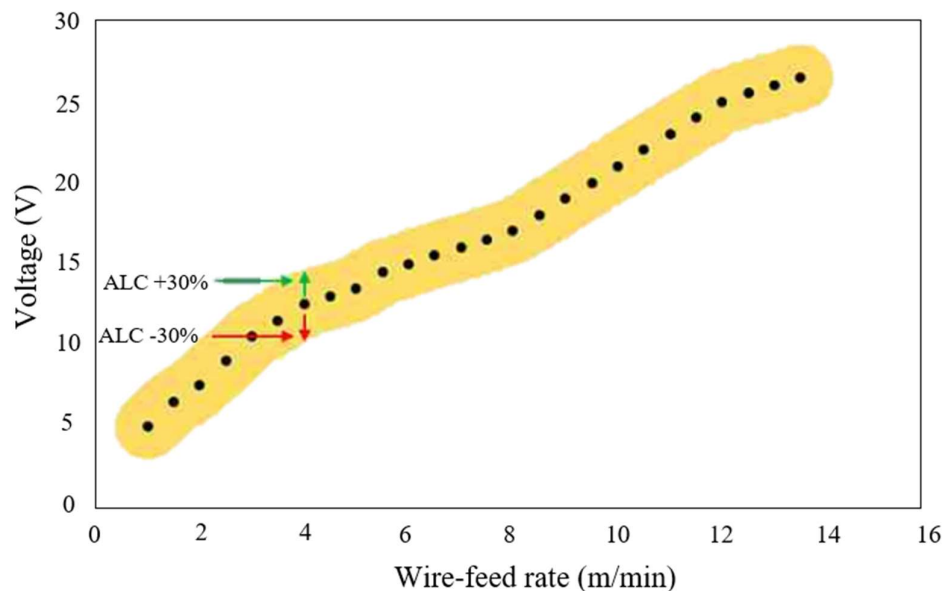


Fig. 11 A schematic of a synergic line, as reported in Ref. [152]

Fig. 11 illustrates a schematic of a synergic line (yellow region), wherein the voltage will change according to the desired wire-feed rate. The dotted curve represents a standard voltage, which results a standard arc length. However, the welding conditions for creating a synergic line cannot be the same as the working conditions. An optimal result can be achieved by using

arc length correction (ALC) through adjusting the voltage. This correction varies spatial elongation of the arc plasma column from -30 to +30%, which respects to the standard arc length. The ALC factor effects the arcing time and leads to a different average of voltage and heat inputs. An increasing ALC value results in longer arc and higher heat input, which leads to higher dilution and wider weld beads, and vice versa. With one control parameter (wire-feed rate), CMT technology can produce consistent welds and saves time in finding optimal parameters.

2.2.4. Equipped Fronius welder

The heat source utilized was a GMAW welder TPS500i from Fronius which was manufactured using state-of-the-art technology. The power source is completely digitized by a microprocessor-controlled inverter power source. Due to the modular design, the equipment offers various welding packages such as GMAW standard, GMAW pulse, pulse multi control (PMC), low spatter control (LSC), and cold transfer technology (CMT), which enables a high degree of flexibility [151]. Details of each package can be seen in Ref. [151].

Table 1 TPS500i Fronius welder [151]

Maximum welding current (A)	500
Minimum welding current (A)	3
Welding current (A) / Duty cycle [10min/40°C] (%)	500/40
Operating voltage (V)	14.2-39.0
Open-circuit voltage (V)	71
Mains frequency (Hz)	50/60
Mains voltage (V)	3×400
Mains fuse (A)	35
Weight (kg)	38

The main specifications of the heat source are reported in Table 1. Besides the power source, the welder includes other components such as torch, wire feeder, and a cooling unit [153]. Depending on the application, users can configure the synergic line from welding conditions, e.g., material and shielding gas, and save it as a job for later use in a machine program. The wire-feed rate is manually set from the knob control while the synergic line itself calculates the voltage and current for setting wire-feed rate.

2.3. Robot system

2.3.1. ARC Mate 100iC/12 robot arm

The FANUC company is one of the world's leaders in robotics. They produce more than 100 robot models, with a maximum payload and reach of up to 2,300.0 kg and 4.7 m, respectively. Among the products of FANUC robotics is the ARC Mate series, which was designed for arc welding [154]. This work uses the ARC Mate 100iC/12 robot arm for additive applications. The specifications of this robot arm are reported in Table 2. This robot arm is an articulated robot with six joints and a maximum reach of about 1420 mm. The robot arm provides a high level of flexibility and reliability. For security, a force sensor is mounted onto the wrist of the robot arm, protecting the robot arm from any damage that could occur due to unexpected collisions.

Table 2 Specifications of the ARC Mate 100iC/12 robot arm

Model	ARC Mate 100iC/12
Controlled axis	6
Repeatability (mm)	± 0.03
Mechanical weight (kg)	130.0
Maximum reach (mm)	1420.0
Maximum load capacity (kg)	12.0

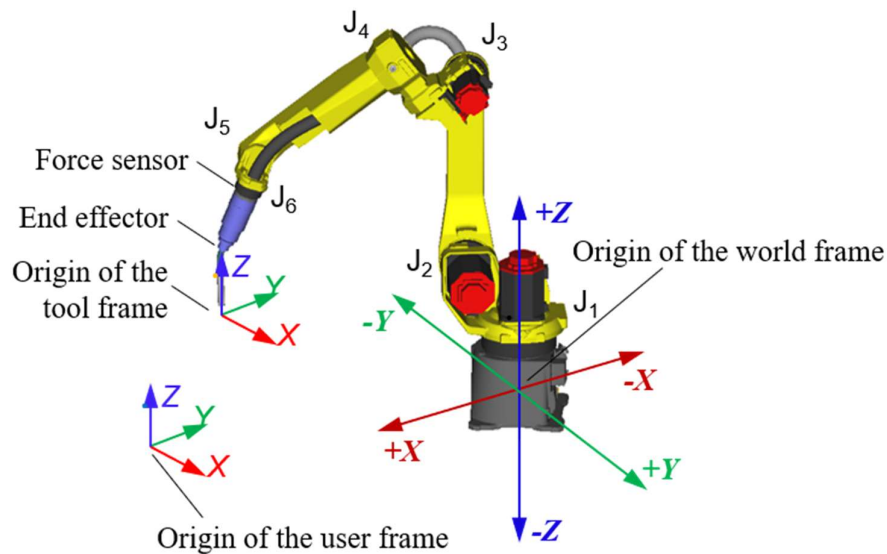


Fig. 12. An illustration of the frame system of the robot arm in Cartesian coordinates

Fig. 12 illustrates the frame system of the articulated FANUC robot in Cartesian coordinates. There are two types of frames in FANUC robotics, which include world frames and customized frames. The former is a single fixed frame that is considered as a reference for others. The

customized frames include tool frames and user frames. Further details and the procedure to set up these frames can be seen in Ref. [155]. A two-axis positioner is integrated as well in order to extend the level of welding position flexibility. The specifications of this positioner are detailed in the following section.

2.3.2.FANUC positioner

Fig. 13 shows an illustration of the FANUC positioner. The positioner includes servo motors, an integrated piping and welding power cable, and a near zero backlash RV-reducer. Further specifications of the positioner are reported in Table 3. The positioner and the robot arm have a highly coordinated motion, allowing for a flexible, reliable and cost-effective solution for AM applications to achieve a high product quality.

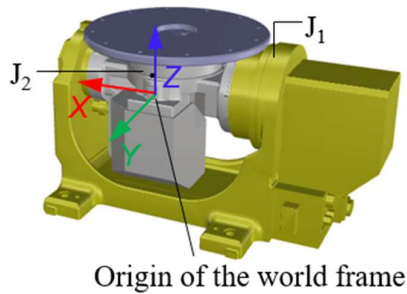


Fig. 13. An illustration of the two-axis positioner

Table 3 Specifications of the positioner

Weight (kg)	395.0
Controlled axis	2
Load capacity (kg)	500.0
Motion range (°)	J1 140
	J2 480
Maximum speed (°/sec)	J1 120
	J2 190

2.3.3.Robot controller and robot language generation

2.3.3.1.R-30iB controller

Any motion of the robot arm and the positioner is driven by one or more of their joint actuators simultaneously. To perform this job, a computer-based controller is needed. This work uses a R-30iB controller to actuate the robot system, one which cooperates with the welder to perform the fusion welding function. More information regarding the controller can be found in Ref. [155]. The basic actions of the robot arm itself are defined by the position and orientation of

the welding torch, which is considered robot level programming. The basic movements are linear and circular interpolation. The positioner used the lower-level programming of joint interpolation, which is defined by the angle of individual joints.

There are essentially three methods of programming which comprise of online programming, offline programming, and hybrid programming. Each method, of course, has its own advantages and disadvantages [156]. The offline programming method is used to generate the CAM program in this work due to some key features, mainly high efficiency and productivity, continuous production, and high levels of accuracy in WAAM applications. Details of this programming method is introduced in the following section.

2.3.3.2.Offline robot program generation

The offline programming method composes of a text-file CAM program, which includes the robot declarations and trajectories. The declarations introduce select information such as program name, date, or robot group. The trajectories describe paths via points through which an equivalent set of joint motions are converted. Other data in the CAM program are also specified, including moving patterns, travel speed, and welding function. In FANUC robotics, Teach Pendant (TP) programs are customarily used. TP programs are binary files that can be edited through the teach pendant buttons (or touch screen). These TP files can also be compiled and decompiled from LS files (human-readable ASCII file). This work uses an alphanumeric method to compose the CAM program as an LS file. The robot controller compiles binary files by means of the *ASCII Program Loader*, which is an extra option from FANUC robotics. In case the *ASCII Program Loader* is not available, TP files can be compiled in the ROBOGUIDE software.

Table 4 Raw data for robot program generation

Layer index	TCP coordinate			TCP orientation			Weld_Enable
	X	Y	Z	Z	Y	X	
1	-50.0	0.0	0.0	1.0	0.0	0.0	TRUE
1	-49.8	-3.6	0.0	0.937	0.0	0.348	TRUE
...
n	-37.2	0.0	80.324	1.0	0.0	0.0	FALSE

Fig. 14 shows the process chain for WAAM parts and the WAAM robot system. Starting from a CAD model, the CAM program is generated by slicing the CAD model with a slicing plane. An appropriate tool path is applied for each cross section in Grasshopper/Rhinoceros and a conversion into the FANUC robot's format is compiled in MATLAB. A table of data, as shown

Table 4, is the output of a tool path strategy. The first column, labeled as the layer index, tells the position of layers from the slicing sequence. The next six rows describe the position and orientation of the TCP in the user frame. To be compatible with FANUC robots, the normal vector is transferred to Euler's angles, including Yaw (C), Pitch (B), and Roll (A). These three elements represent the angular displacements of the TCP with respect to the world frame. Yaw is a rotation of the TCP along the z-axis, Pitch is a rotation of the TCP along the y-axis after applying Yaw, and Roll is defined as a rotation along the x-axis after applying Yaw and Pitch sequentially. The order of these rotations is essential, as a different sequence can lead to incorrect orientation. The last column is a Boolean variable, which indicates whether the welding function is on or off. The LS program is transferred to the robot controller through either a portable USB storage device or an Ethernet/IP protocol.

When utilizing the positioner, the robot arm and positioner must be coordinated to perform the desired task. The motion addresses not only the starting and stopping motion of two groups at the same time, but also the relative TCP speed must be controlled automatically. The next section presents a FANUC robotics tool that allows for this vital coordinated motion to be performed.

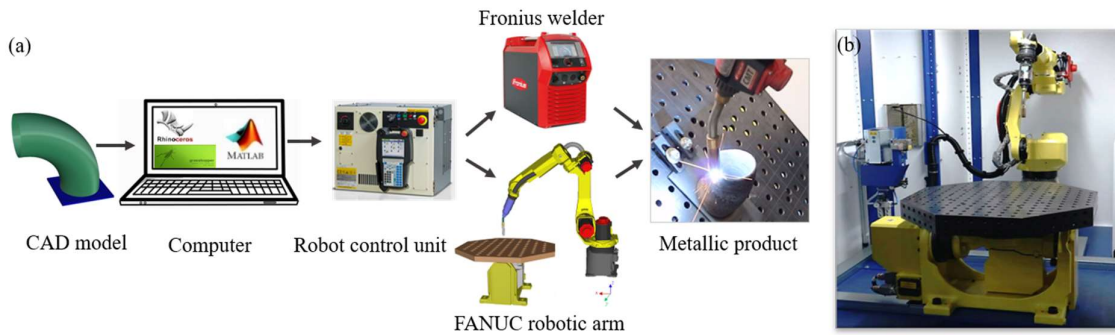


Fig. 14 Illustration of the process chain (a) and WAAM robot system (b)

2.3.3.3.Coordinated motion control

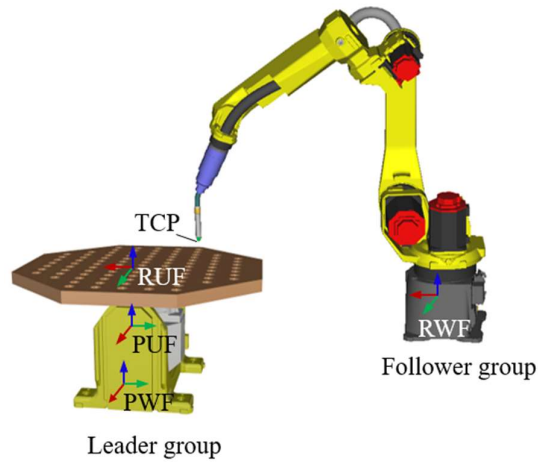


Fig. 15. Coordinated motion overview

When a robot system has more than one group, as illustrated in Fig. 15, the positioner plays the role as the group leader while the other group to become a follower. To achieve the desired coordinated movements, the TCP speed and position of the follower are manipulated in relation to the leader group. This motion provides a constant relative speed between the two moving groups. These actions provide several advantages for fusion welding, the chief of which include [157]:

- the maintenance of a relative speed between the positioner and robot arm,
- a reduction in the time required for programming,
- a continuous welding process, and
- flexible control of welding position.

2.4. Testing and measuring devices

2.4.1.Microscope

To capture macrographs, this work used the Leica DFC290 stereomicroscope, as shown in Fig. 16. This stereomicroscope can capture real-time images by means of digital color cameras with CMOS sensors and a 3.0 Megapixel resolution. The microscope is connected with a PC so that the images can be viewed directly on the PC screen. After being captured, these images can be analyzed by a means of a user-friendly application. For example, adding straight lines, selecting free-form regions, measuring distances between two objects.



Fig. 16 Leica DFC290 stereomicroscope

2.4.2.Metrology equipment

To capture profiles of additive parts, a 2D profilometer was used. This work employed a 2D scanner from QuellTech with the model Q4. This scanner uses the triangulation principle to detect the two-dimensional profile of surfaces with a maximum length of 20 mm. The device projects a blue laser line to the targeted object while a two-dimensional receiver captures the diffused light from the reflected laser line. Each laser line is defined by a few points with a resolution of 0.0133 mm.

In addition to the profilometer, a 3D scanner was used to capture the 3D geometry of metal parts, which is ATOS 5 from GOM GmbH. The ATOS 5 sensor allows for high-precision data with a short measuring time (0.2s/scan). The 3D scanner has two cameras and a blue light projector. Similar to the 2D scanner, the sensor system functions based on the triangulation principle. The projector projects a fringe pattern onto surfaces of interest and the cameras capture the reflection. Depending on the lenses, the maximum measuring volume can be up to $1000 \times 750 \times 750 \text{ mm}^3$. For each scan, the system creates up to 12 million points, meaning the larger the measuring volume is, the lower the resolution. For instance, the minimum and maximum volume experience is a resolution of 0.058 and 0.289 mm, respectively. With selected lenses, the resolution is 0.115 mm. After construction, mesh objects were analyzed and evaluated in the GOM Inspect software.



Fig. 17 ATOS 5 system - 3D scanner

2.4.3. Uniaxial tensile testing machine

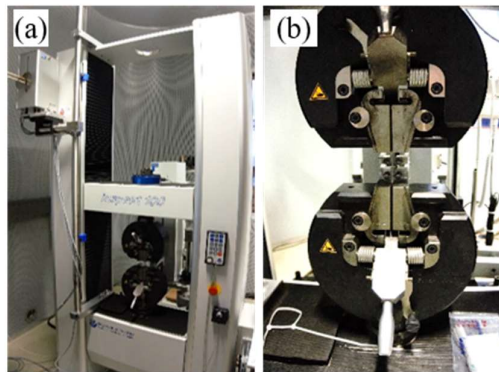


Fig. 18 Uniaxial tensile testing machine 'Inspekt 100'

To examine the strength of materials, uniaxial tension testing was performed on the tensile testing machine “Inspekt 100”, as shown in Fig. 18. Specimens were machined with dimensions defined according to a standard. To perform the tension test, specimens were clamped on both sides by wedge clamps and pulled to failure to determine important material parameters. These parameters consisted of Young’s modulus, yield strength, ultimate strength, and elongation. To eliminate elongation errors, this study used a contact extensometer.

2.5. Materials

This work used mild steel and aluminum to manufacture examined parts. Metal parts with mild steel were deposited on C45 carbon steel substrates with 5.0 mm thickness. An electrode wire (ER70S-6) with a 1.0 mm diameter was used. The chemical composition of the electrode wire and the substrate are presented in Table 5, according to DIN EN 10083-1 [158] and AWS standard [159], respectively. Table 6 presents the mechanical properties of as-welded metal.

Table 5 The chemical composition of ER70S-6 and C45

Material	Element (Wt.%)						
	C	Mn	Si	P	S	Cr + Mo + Ni	Fe
C45	0.42	0.5	0.3	0.03	0.03	0.63 max	Remainder
ER70S-6	0.073	0.97	0.51	0.009	0.013	--	Remainder

Table 6 The as-welded metal properties of ER70S-6

Tensile Strength (MPa)	537.8
Yield Strength (MPa)	448
Elongation (%)	24%

Metal parts with aluminum were made from AlSi5 with an electrode wire of 1.2 mm in diameter. The chemical composition and mechanical properties of as-welded metal are presented in Table 7 and Table 8 respectively according to the ISO 18273 and AWS A5.10 standard.

Table 7 The chemical composition of AlSi5

Material	Element (Wt.%)								
	Si	Fe	Cu	Mn	S	Cr	Zn	Ti	Al
AlSi5	5.2	0.19	0.1	0.02	0.03	0.001	0.021	0.015	Remainder

Table 8 The as-welded metal properties of AlSi5

Tensile Strength (MPa)	>120
Yield Strength (MPa)	40
Elongation (%)	8%

3. Multi-bead overlapping models

3.1. Chapter introduction

When bulky structures are generated using standard layer-by-layer tool paths, the build rate in the outer contours of the part may lag the build rate within the interior. However, hybrid patterns consist of zigzag patterns surrounded by contour lines, reducing the processing time and enhancing geometrical accuracy. Nonetheless, it must be noted that contour beads grow slower in height than zigzag beads due to the fact that the boundary contour only overlaps on one side with other weld beads [53]. As a metal part requires the deposition of several layers, uneven layer surfaces may lead to accumulated errors along the growth direction, resulting in unstable deposition after a few layers. Therefore, it is essential to establish robust models that flatten the deposition surface within hybrid patterns.

In the GMAW-CMT process, the profile of a single weld bead resembles a parabola. Optimal overlapping distances can be determined in order to keep a consistent build rate at each point of the layer. This chapter introduces a robust method to compensate for the shortage of material in the outer beads with the overall aim of levelling the upper surface. This chapter presents new multi-bead overlapping models for tool path generation. Mathematical models are established to minimize valleys between adjacent weld beads by accounting for the overlapping volume. The proposed models are validated by manufacturing solid blocks from mild steel with the recommended overlapping distances. The approach is compared to standard tool path strategies by means of capturing boundary profiles. The specimens with the proposed overlapping distances showed an even profile in contrast to specimens made using the standard strategy. The following section details the proposed overlapping models and verifies the proposed models.

3.2. Establishment of multi-bead overlapping models

A weld bead cross-section profile is usually represented as parabola, cosine, or arc model. The parabola model was applied in this study to establish the overlapping models as it experiences the best fit to actual weld bead profiles [45, 46]. There are two parameters to consider when modelling weld bead geometry: weld bead height (h) and weld bead width (w). Fig. 3 in section 1.3.1 illustrates a symmetrical parabolic model of the form Eq. (3.1).

$$z = ay^2 + b \tag{3.1}$$

According to Ref. [43], the two parameters a and b can be expressed by the height and width of the profile via $a = -4h/w^2$ and $b = h$.

The proposed models are established by the following assumptions:

- The cross-sectional profile of a single weld bead is a parabolic profile.
- With constant process parameters, the weld bead geometry is unchanged.
- The density of the material is unchanged before and after deposition.

Weld beads are formed by the solidification of molten material whilst the weld bead geometry inherits the dimension from the weld pool. According to existing studies [160, 161], the weld pool yields an elliptic form when depositing at low and moderate travel speeds, and yields a tear drop shape when at high travel speeds, as illustrated in Fig. 19. The front of weld pool is supposed to be an arc with radius r [139].

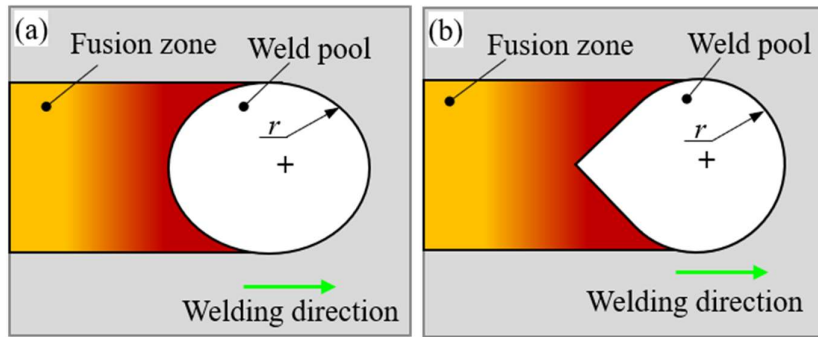


Fig. 19. Schematic of weld pool shape: (a) elliptical shape; (b) tear drop shape

Applying a substitution from Eq. (3.1), the parabolic model can be expressed as:

$$z = -\frac{4h}{w^2}y^2 + h \quad (3.2)$$

The cross-section area of a single weld bead profile is calculated from an integration equation via the weld bead geometry:

$$A = 2 \int_0^{w/2} \left(-\frac{4h}{w^2}y^2 + h \right) dx = \frac{2h \cdot w}{3} \quad (3.3)$$

w and h can be computed by the process parameters illustrated in Eq. (3.4) and Eq.(3.5), respectively [162].

$$w = \frac{3\pi \cdot v_w \cdot d_w^2}{8h \cdot v_t} \quad (3.4)$$

$$h = C_1 \cdot v_w^2 + C_2 \cdot v_t^2 + C_3 \cdot v_w \cdot v_t + C_4 \cdot v_w + C_5 \cdot v_t + C_6 \quad (3.5)$$

Where d_w is the wire diameter, v_w is the wire-feed rate, and v_t is the travel speed and C_x are constants. Further details can be seen in Ref. [162].

Fig. 20 depicts the schematic of a multi-bead profile for hybrid tool path patterns. Bead 1 and bead 2 are for zigzag patterns, and bead 3 is deposited by following a contour pattern. The overlapping length (l) for the zigzag patterns equals to $0.738w$ [45] and d_l represents the distance from edges to zigzag patterns.

A weld seam is manufactured by creating a weld pool along a certain path. When the welding torch changes the direction, the weld seam has a fillet with the radius of r introduced wherein r equals half of the weld bead width:

$$r = \frac{w}{2} \quad (3.6)$$

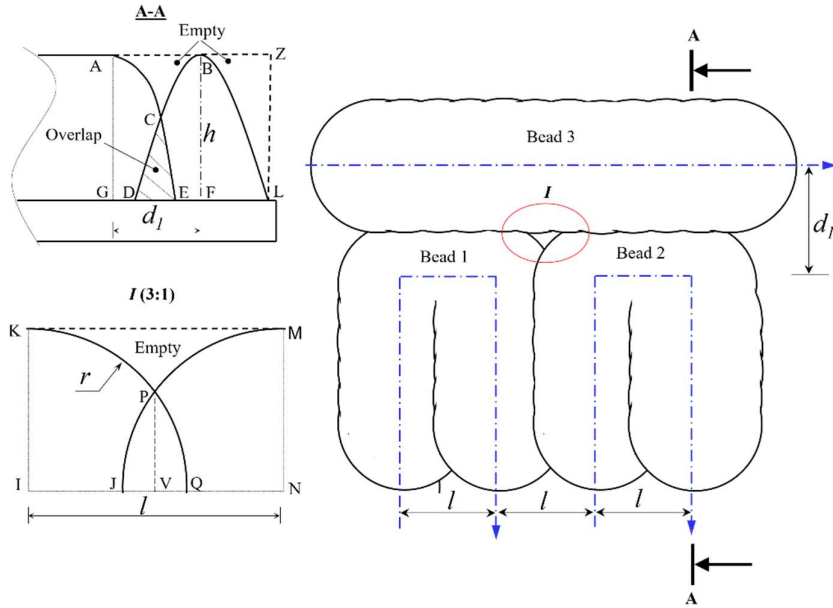


Fig. 20. A schematic of a multi-bead profile for zigzag and contour patterns

A function $f(d_l)$ is introduced, which denotes the difference of the empty and overlapping volume in $2l$:

$$f(d_1) = \sum V_{empty} - \sum V_{overlap} \quad (3.7)$$

The empty volume includes three volumes, which are V_{ABC} , V_{BLZ} , and V_{KMP} .

$$\sum V_{empty} \approx 2l.S_{ABC} + 2l.S_{BLZ} + h.S_{KMP} \quad (3.8)$$

S_{ABC} is the area of the valley between a zigzag and a contour pattern.

$$S_{ABC} = S_{ABFG} - (S_{AEG} + S_{BDF}) + S_{DCE} = h.d_1 - \frac{2}{3}h.w + S_{DCE} \quad (3.9)$$

S_{BLZ} is the right-side area of a contour pattern.

$$S_{BLZ} = S_{BZLF} - S_{BFL} = \frac{h.w}{2} - \frac{h.w}{3} = \frac{h.w}{6} \quad (3.10)$$

S_{KMP} is the area created from the borders of zigzag and contour patterns.

$$\begin{aligned} S_{KMP} &= S_{KMNI} - 2S_{IKQ} + 2S_{PQV} \\ &= l.r - \frac{\pi.r^2}{2} + 2 \int_{l/2}^r \sqrt{r^2 - x^2} dx = 0.036w \end{aligned} \quad (3.11)$$

The overlapping volume formed by zigzag and contour patterns.

$$\sum V_{overlap} = 2l.S_{DCE} \quad (3.12)$$

Combining Eqs. (3.6 - 3.12), the deviation function $f(d_1)$ can be specified as:

$$\begin{aligned} f(d_1) &\approx 2l.h.d_1 - \frac{4}{3l.h.w} + 2l.S_{DCE} + \frac{l.h.w}{3} + 0.036h.w^2 \\ &\quad - 2l.S_{DCE} \\ &\approx 2l.h.d_1 - l.h.w + 0.036h.w^2 \end{aligned} \quad (3.13)$$

To smooth welding surfaces, the overlapping and empty volume should be equal, therefore making the function $f(d_1)$ equal to zero:

$$2l.h.d_1 - l.h.w + 0.036h.w^2 = 0 \quad (3.14)$$

$$\Rightarrow d_1 = 0.47w \quad (3.15)$$

The growth rate of outer beads lags at the interiors. This can be explained by boundary weld beads only having a one-sided overlap while the interior beads have two-sided overlap, as illustrated in Fig. 21. To smooth the last welding surface, the overlapping distance (d_2) should be optimized. Utilizing the same method to determine d_1 , the empty areas are compensated by more material from the overlapping area. A function $f(d_2)$ denotes the difference between the empty and overlapping area:

$$\begin{aligned} f(d_2) &= \sum A_{empty} - \sum A_{overlap} \\ &= S_{ABCD} - S_1 - S_2 - A_{overlap} \\ &= S_{ABCD} - S_1 - (0.5S_1 - A_{overlap}) - A_{overlap} \\ &= h(d_2 + 0.5w) - 1.5S_1 \\ &= h(d_2 + 0.5w) - h.w \end{aligned} \quad (3.16)$$

To smooth welding surfaces, the empty and overlapping area should be equal, thus the function $f(d_2)$ equals to zero.

$$d_2 = 0.5w \quad (3.17)$$

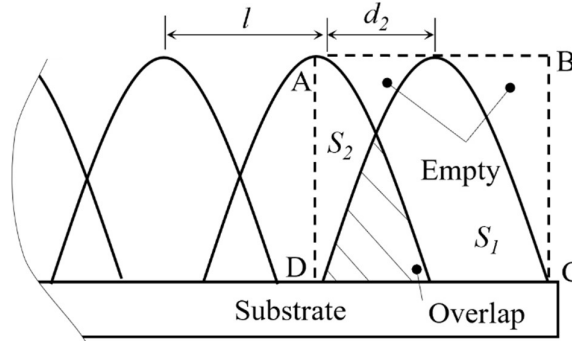


Fig. 21. A schematic of the cross section of the multi-bead profiles

The optimal overlapping distances for hybrid patterns can be determined from the bead width. For instance, the overlapping distance between zigzag and contour patterns equals to $0.47w$ and $0.5w$ in parallel weld beads.

3.3. Validation of the proposed overlapping models

This section presents an experimental method to verify the proposed models. Metallic blocks were manufactured with an existing overlapping distance and the proposed distances. To have an objective comparison, three sets of travel speeds and wire-feed rates were used, as illustrated in Table 9. Other process parameters, such as the wire electrode (ER70S-6) and shielding gas composition, were unchanged.

The blocks were deposited on carbon steel substrates (C45) with a thickness of 5.0 mm. The shielding gas composition was 80% Ar and 20% CO₂ with a flow rate of 15L/min. Stick-out is the length of solid electrode extending from the nozzle tip and was consistently kept at 12.0 mm. Six metal blocks were fabricated for comparison.

The hybrid tool path pattern and the dimensions of examined blocks are shown in Fig. 22. The blocks were deposited with seven deposited layers. The weld beads number must be integer with a constant weld bead geometry to allow for the dimensions to change slightly, thereby maintaining the overlapping distances. With the proposed models, d_1 and d_2 equal to $0.47w$ and $0.5w$, respectively, and l is set to $0.738w$; the corresponding values are shown in Table 9. For the existing model, all overlapping distances are equal to $0.738w$, for instance, $d_1 = d_2 = l = 0.738w$.

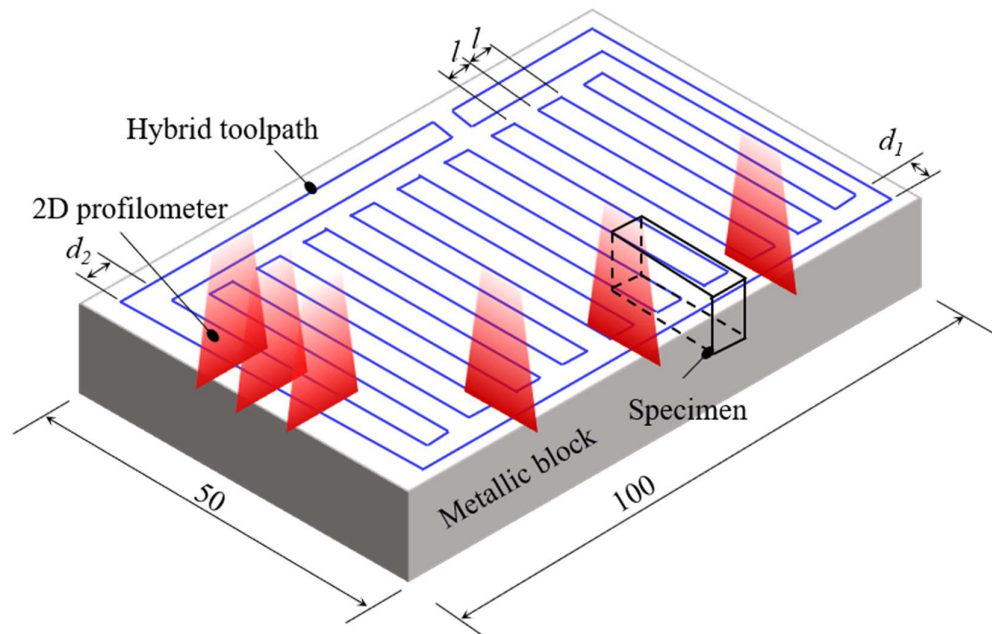


Fig. 22. A schematic of examined blocks

Table 9. Variation of welding parameters

No.	Welding parameters		Bead width	Proposed overlapping distances			Existing overlapping distances		
	v_w (mm/min)	v_t (mm/min)	w (mm)	l (mm)	d_1 (mm)	d_2 (mm)	l (mm)	d_1 (mm)	d_2 (mm)
1	5700	400	6.77	5.0	3.18	3.38	5.0	5.0	5.0
2	6600	600	6.32	4.7	2.97	3.16	4.7	4.7	4.7
3	7600	400	7.42	5.5	3.49	3.71	5.5	5.5	5.5

The two methods used to evaluate the waviness in boundary areas were a macrograph and a 2D profilometer. The former is intuitive for showing weld bead layers, but this destructive method needs a great deal of effort for the preparation of specimens. Consequently, it was just applied for the first case when v_w and v_t were 5700 mm/min and 400 mm/min, respectively. With a low cutting speed, a band saw was used to extract the specimens for macrographs from blocks. Sequentially, the specimens were first ground with grade P4000 sandpaper then polished with a 3.0 μ m polishing paste before applying Nitric acid with a 3% solution onto the polished surfaces. Macrographs were captured by means of the Leica DFC290 stereomicroscope and the DFC209 HD camera with a magnification $\times 0.65$ (Fig. 16).

The second method used a 2D profilometer and is a non-destructive method that can evaluate surface profiles without damaging metal blocks. The measuring procedure for this method is also more effective when compared with the destructive method.

3.4. Performance of the developed overlapping models

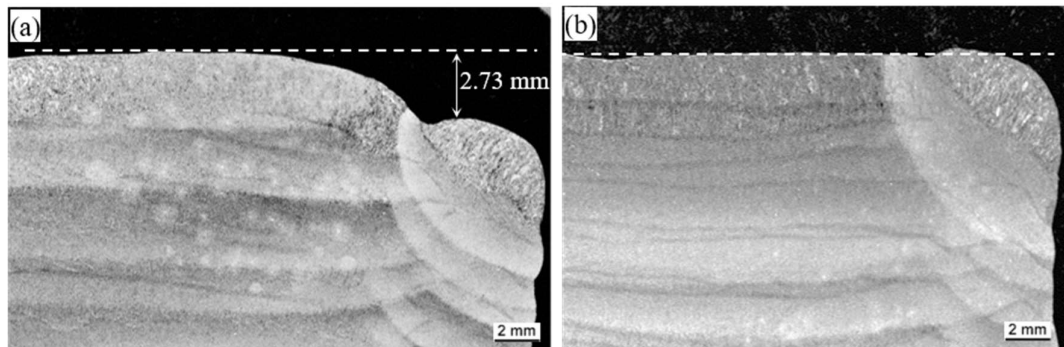


Fig. 23. Macrographs of specimens: (a) existing overlapping distance ($d_1 = 0.738w$); (b) proposed overlapping distance ($d_1 = 0.47w$)

Fig. 23 compares macrographs from the existing overlapping distance ($d_1 = 0.738w$) and the proposed overlapping distance ($d_1 = 0.47w$). The existing model yields an uneven surface, with a boundary that grows less than the interior area by about 2.7 mm after seven layers. Contrarily, the proposed model results in a smooth surface since the shortage of material in the boundary is compensated for by a smaller overlapping distance.

With the non-destructive method, surface profiles were able to be captured three times. Median profiles are illustrated in Fig. 24. The existing model yields considerably lower heights in boundary weld beads. The proposed models, by contrast, resulted in much better surface profiles.

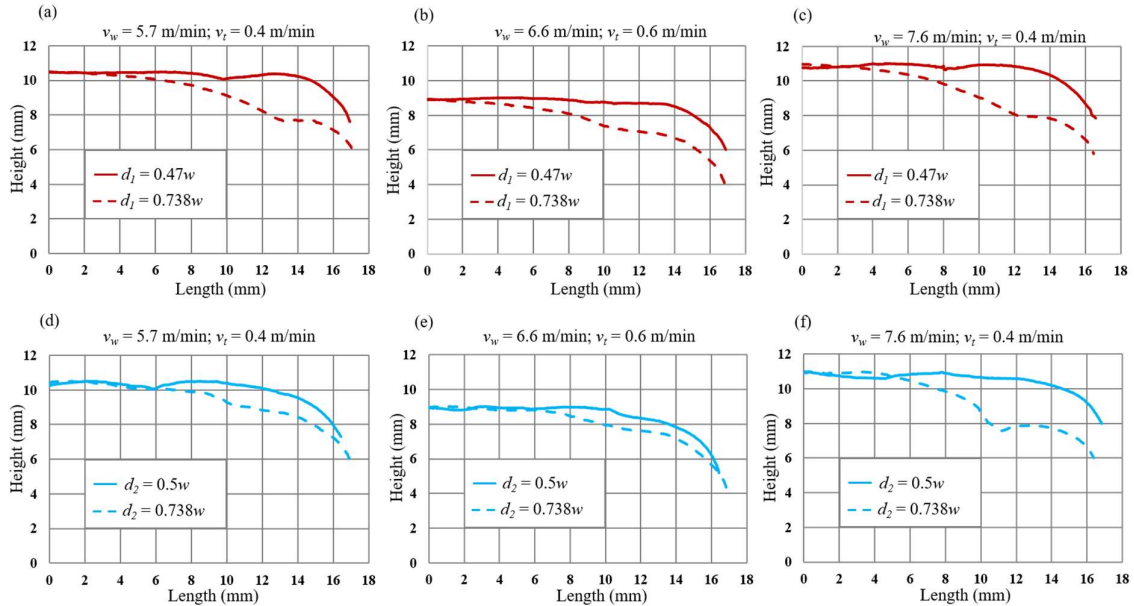


Fig. 24. A comparison of surface profiles between the proposed models and the existing model

3.5. Summary of findings within the chapter

This chapter addressed the problem of uneven deposition surfaces due to the build rate within the outer contours possibly lagging the build rate within the interior. Optimal overlapping distances between adjacent weld beads were determined in order to smooth the surface. With the overlapping volume approach, the mathematical models for multi-bead overlapping in boundaries were developed to compute the overlapping rates. The distances can be calculated from the weld bead width, e.g., zigzag and contour patterns have the optimal overlapping distance of nearly half of bead width while the overlapping distance for zigzag patterns is half the bead width. The proposed models were verified on mild steel, which shows promising results.

4. Tool path generation for lightweight structures

4.1. Chapter introduction

In many industrial sectors, e.g., transportation and construction, weight reduction plays an essential role in reducing harmful gas emissions, energy usage, operational costs, and also helps maintain sustainable development. When it comes to weight reduction, some lightweight materials such as magnesium alloys, aluminum alloys, titanium alloys, or composites are mostly employed. However, these materials when utilized alone are not always economic due to their high expense. It has been reported that using lightweight structures can achieve weight savings of 50% and shorten development times [163]. Therefore, a combination lightweight structures can lead to a significant weight reduction.

Lightweight structures achieve a strength-to-weight ratio superior to that of solid structures, but the processes of manufacturing these structures are complicated and costly due to their complex shape and intricate geometry. For instance, high-performance components are typically produced by forging and subsequent milling. Forged ribs are created by forming work pieces between two dies, a process that usually results in high tooling costs. Some structures like rib-web structures are manufactured by removing material from solid blocks, yielding a very high buy-to-fly ratio and material waste. Here it comes with a trade-off between weight reduction ratio, material costs, and manufacturing costs. As mentioned above, the WAAM process has the potential to manufacture medium and large-size parts with high deposition rates at low costs. In addition to this, the process has a low buy-to-fly ratio and no tooling costs. Hence this process is highly suitable for components such as rib-web, thin-walled or honeycomb structures. This chapter introduces another method of producing of lightweight structures, using the additive material method instead of machining or forging. This new manufacturing method can lead to better designs, efficient manufacturing and quality end products.

In WAAM, the welding strategy greatly influences the properties and quality of deposited parts. With an increasing number of starts and stops, the danger of uneven material build-up and welding defects increases. Unfortunately, most rib-web structures do not represent Eulerian paths, i.e., they cannot be manufactured with a continuous welding motion, in which every edge is visited only once. It has been found that doubling the number of welding passes on each edge of the rib-web structure turns non-Eulerian paths into Eulerian paths, which can be welded continuously. When two or more weld beads are deposited on each edge, the vertices of the rib-web structure may suffer from underfilling.

To realize this new manufacturing method, an efficient tool path strategy is required. To answer this need, a new tool path strategy for lightweight structures is put forward within this report with the aim of improving the deposition quality for rib-web components while mitigating the disadvantages of discontinuous welding paths, such as welding defects and uneven build-up. The welding torch follows a continuous contour pattern defined as a Eulerian path for arbitrarily connected rib-web structures, thus avoiding the drawback of starting and stopping in a layer. To avoid underfilling, a correction strategy has been developed to allow for dense vertices.

This chapter begins with section 4.2, a detailed analysis of the waviness and achievable wall thickness in single and double-bead strategies. It demonstrates that achieving a certain wall thickness in ribs requires two or more overlapping beads per layer. Moving from a single bead to a double-weld bead strategy is shown to pave the way for creating Eulerian paths from any connected rib-web structure. This forms the continuous tool path strategy that is detailed in section 4.3. The correction strategy is described in section 4.4, where a machine learning method is also employed to predict the void length. Section 4.5 presents the testing procedure to examine the mechanical properties for metal parts that have been produced by the proposed method. The performance of the developed method is illustrated in section 4.6. The last section presents a summary of the new manufacturing process.

4.2. Waviness and deposition efficiency

Unlike powder-based process, the WAAM process is suitable for near-net shape deposition. Post-processing, such as milling operations, must be applied to areas which require accurate dimensions and good surface appearance. It is necessary to adapt CAD models for machining allowances before fabrication [164]. The removal depends on the roughness and waviness of the surface. To this end, the quality of the surface is evaluated through the waviness. When it comes to a WAAM process, the weld bead geometry will affect the surface properties, as a bigger weld bead leads to a rougher surface [165]. To investigate the waviness, five walls of the mild steel ER70S-6 were deposited with a constant wire feed rate of 5200 mm/min with different levels of travel speed that ranged from 1000 to 200 mm/min. Each single-bead wall is 100.0 mm length and is deposited with 20 layers. The deposition direction alternated after each layer with an idle time of 10s before resuming the deposition process.

According to the DIN EN ISO 4287 standard, waviness (W_t) is the greatest difference of amplitudes. The waviness in this work was evaluated using macrographs. As illustrated in Fig. 25, specimens with a thickness of 10.0 mm were extracted from the middle of the wall in the 4th layer upwards to avoid thermal instabilities within the first few layers [59]. The specimens

were ground and polished with grade P4000 sandpaper then polished with a 3.0 μ m polishing paste. Macrographs were taken by means of the DFC209 HD camera and the Leica DFC290 stereomicroscope with a magnification $\times 0.65$.

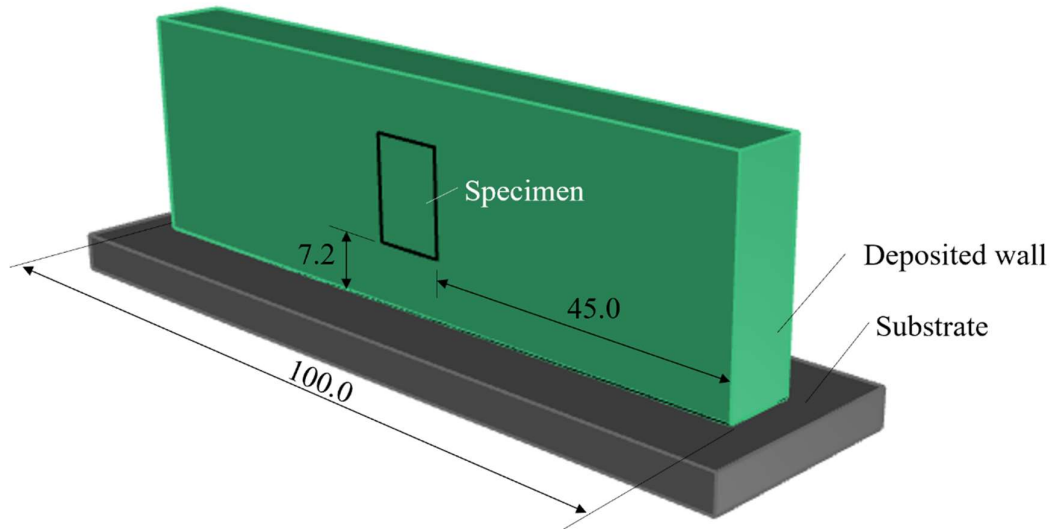


Fig. 25. A schematic of specimen extraction for the waviness investigation

4.3. Establishment of Eulerian paths

Fig. 26 illustrates a schematic graph for the representation of a tool path for a rib-web structure wherein the four nodes are represented as four vertices. The welding torch follows a certain sequence of vertices to build the rib-web structure. As can be seen, no Eulerian path is feasible in this case. For example, the geometry can be deposited with two welding passes (Fig. 26a) and, because of the discontinuous process, the processing time increases resulting in the possibility of uneven weld beads at the junctions. Furthermore, the wall thickness is also limited to a certain range. Tool paths for arbitrary rib-web structures can be transformed into Eulerian paths if the number of incoming and outgoing edges are equal at each vertex. This can be realized by moving twice along each edge, hence each vertex is visited twice as often as with single-bead deposition and turned into a vertex of even degree, as illustrated in Fig. 26b. The tool path is continuous within a layer and the welding torch can start at an arbitrary position and end at this position. Although the approach is promising in terms of mathematics, problems might occur when path lines cross at vertices. As illustrated in Fig. 26c, this issue is overcome by introducing connector lines. Two path lines working on the same edge are cut and connected, generating four new vertices of degree two. The proposed method results in continuous tool paths while avoiding imperfections at vertices which can be encountered with the direct crossing strategy.

It should be noted that the path length is doubled with the proposed strategy. This can cause for a longer processing time compared to a single bead strategy. For real applications, it seems justified to deposit more weld beads to achieve the desired thickness. Typical wall thicknesses and machining allowances need a minimum wall thickness in as-deposited rib-web structures.

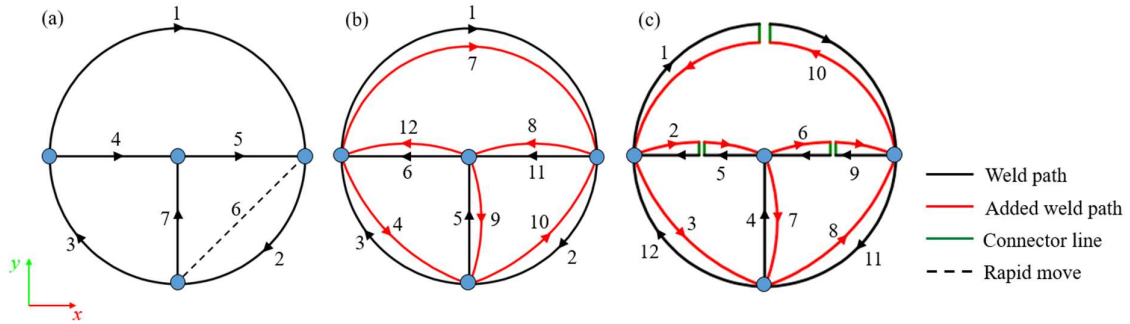


Fig. 26. A representation of the tool path by a graph: (a) single pass; (b) double pass without connector lines; (c) double pass with connector lines

The approach described above paves the way for constructing continuous paths from the viewpoint of graph theory. To realize this approach, the tool path lines are calculated from part geometry. Parts are manufactured from the bottom to the top, layer-by-layer. Tool paths are also planned in this sequence. Cross sections can be obtained by slicing the CAD model along the +Z direction but the step size depends on the layer thickness until there is no more intersection between the slicing plane and the CAD model, as shown in Fig. 27a. A typical cross section between the slicing plane and the CAD model is illustrated in Fig. 27b. It includes a single outer contour curve and three inner contour curves. A corresponding offset curve was generated for each contour curve, as depicted in Fig. 27c, and the offsetting distance was calculated on the wall thickness and overlapping distance (l). The geometry can be deposited by moving the welding torch along the offsetting contours, but the deposition process is discontinuous, i.e., the welding torch needs to jump between contours which means these contours should be connected. In order to connect the two contours, two connector lines are added, which are labelled as ‘connector lines’ in the aforementioned Fig. 26. With n as offset curves, the number of connector lines required is $2(n - 1)$. A random segment/edge of each offset curve is selected at a random location, which is in-between one-third and two-thirds of the length of the selected segment. The random allocation of connector lines mitigates the possibility of traces on the part that occur if the connector lines are at the same position. As can be seen in Fig. 27d, a single closed curve is generated which can be represented as a Eulerian path. It is worth to mention that adding two connector lines on the same edge is not possible, as

illustrated in Fig. 27e. For this situation, two connected offset curves and a closed sub-path is generated on an edge. Such closed sub-paths must be avoided since it would break the continuity of the deposition process. To overcome this problem, a condition is added when selecting random edges for the generation of a connector line: each edge is chosen one time only.

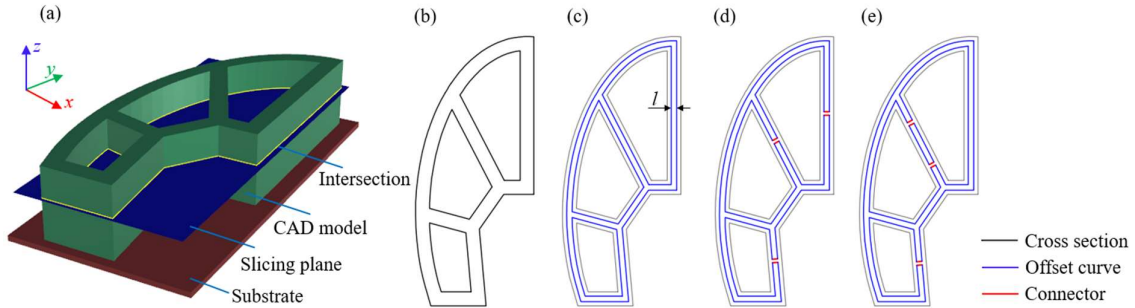


Fig. 27. Eulerian path generation: (a) illustration of the slice procedure; (b) cross section; (c) offset curves; (d) valid path; (e) invalid path

4.4. Solutions for void filling in junctions

4.4.1.A geometric solution for void filling

Fig. 28 shows an example of a junction built by three single weld beads. It is possible that deposited material may insufficiently fill the vertex, causing possible underfillings (voids) inside the vertex of the rib-web structure. Additionally, sharp turning angles can lead to an inaccurate motion of the welding torch, thereby enlarging voids. As demonstrated in Fig. 29, the command FINE in the FANUC robot ensures the precise motion of the welding torch while the robot arm can decelerate and stop at the target before moving on to the next point. This can increase heat density and lead to overheating or excess material [166]. Consequently, it is vital to maintain a constant travel speed. The FANUC robot used in this work allows for this task to be realized via the continuous motion command (command CNT100) [155]. The target point (V_i) cannot be reached by the tool center point (TCP) in order to maintain the welding velocity. Instead of reaching the target, the robot arm interpolates to a nearby position.

Developing physics-based models to effectively resolve this problem is challenging. The void area depends on process parameters, configuration of vertices, material behavior, and part geometry. A heuristic method was developed to compensate for these kinds of underfillings. The approach is to modify the tool path at sensitive vertices, i.e., the TCP is adjusted to move deeper into the center of the junction by changing the position of the vertices of the tool path.

The following section will solve the question of how to determine the shifting length of the vertex with the aim of avoiding underfillings.

As can be seen in Fig. 28, \overline{APB} represents the tool path for a weld bead. Supposing that this section is selected to correct the deposited material volume, $\overline{A_oP_oB_o}$ is an offset curve to \overline{APB} with l . The position of P is used to shift the turning point from P to P_N in the direction of P_o . The shifting distance relies on the vertex angle (θ) and is larger when θ is smaller.

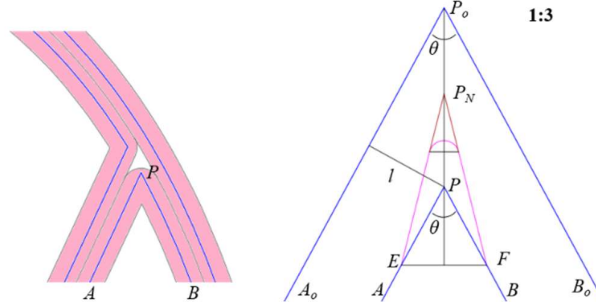


Fig. 28. A schematic of a basic adaptive void-filling path

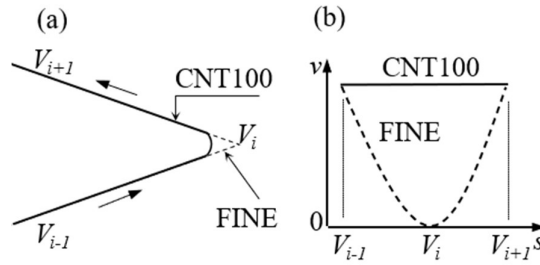


Fig. 29. A welding speed diagram at a turning point: (a) tool path pattern; (b) velocity diagram

In terms of geometry, the offset distance can be calculated as:

$$\overline{PP_o} = \frac{l}{\sin(\theta/2)} \quad (4.1)$$

P_N is between P and P_o . To have a multi-bead wall with even deposition surface, $\overline{P_oP_N}$ is equal to l .

$$\overline{PP_o} = \overline{P_oP_N} + \overline{PP_N} = l + \overline{PP_N} \quad (4.2)$$

From Eqs. (4.1) and (4.2), P_N can be estimated as:

$$\overline{PP_N} = l \left(\frac{1}{\sin(\theta/2)} - 1 \right) \quad (4.3)$$

The two points (E and F) denote the start and end point of the modified path. These points are located on the original path and their distance equals to l . Their coordinates can be calculated as:

$$\overline{PE} = \overline{PF} = \frac{l}{2 \sin(\theta/2)} \quad (4.4)$$

The TCP follows the path $\overline{AEP_NFB}$ instead of \overline{APB} to avoid the aforementioned underfilling. However, voids depend on many factors, and so a geometrical solution might not be valid for an arbitrary situation. To enhance the capability and reliability of the proposed approach, the empirical weight λ is introduced, which adapts the position of the point P_N properly:

$$\overline{PP_N^*} = \lambda \cdot l \left(\frac{1}{\sin(\theta/2)} - 1 \right) \quad (4.5)$$

An experimental approach is used to determine the value of λ as well as to evaluate the voids created from the welding experiments. L denoted the measured length of the void from the deficit of material and the empirical weight was predicted from L and θ_{min} (the smallest angle of the conjunction) as:

$$\lambda = \frac{l \left(\frac{1}{\sin(\theta_{min}/2)} - 1 \right)}{L} \quad (4.6)$$

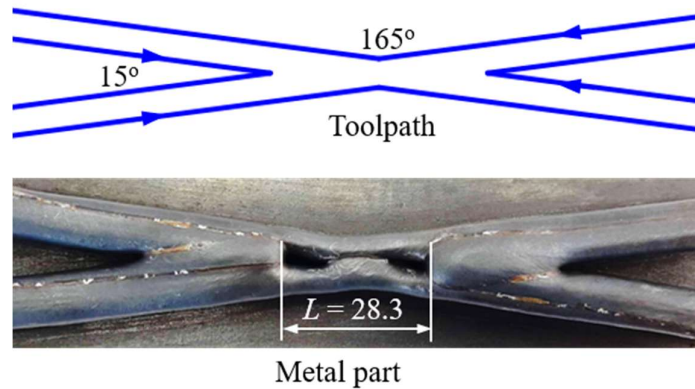


Fig. 30. An illustration of determining L with standard contour

Fig. 30 shows the procedure of L determination. The example has four arms with symmetrical geometry. The junction was deposited with 12 layers with a layer thickness of 1.8 mm. Table 10 reports the process parameters. The metal part has a valley and two voids. A digital caliper was used to determine the valley's length, which equals to 28.3 mm. The empirical weight was calculated once using the geometrical relation expressed by Eq. (4.6), and then once again later, using (\overline{PP}_N^*) to compute the shifting distance for the selected turning point.

To have a more objective insight into the proposed method, more experiments were implemented to investigate the feasibility and efficiency of the geometrical correction. Different junction geometries were deposited with and without the correction. Four different configurations were examined, as shown in Fig. 31. Metal parts were deposited, and face milled to observe and analyze surfaces. To investigate the existence of voids, other non-destructive methods can be also used, such as radiography [167] and ultrasonic inspection [168]. With these methods, the process of quality control can be integrated in quality control during production.

Table 10 Process parameters for rib-web structures

Process parameters	Value
Material	Mild steel
Wire-feed rate (mm/min)	5200
Travel speed (mm/min)	400
Wire diameter (mm)	1.0
Shielding gas	80% Ar + 20% CO ₂
Gas flow (L/min)	15.0

Using defect welded geometries to determine the distance L is cumbersome in practice. The correction factor (λ) cannot be estimated by a model without using experimental data due to the complex dependence of L on the junction geometry, material, and process parameters. Each junction type was first produced to get the geometrical error. This approach seems feasible for mass production. However, it is not justified to deposit a part so that a corrected part can be produced in case of small batch size. Sacrificing these parts is unnecessary and costly. The challenge here was to develop a rule-based model which can predict L from unknown junction geometry. The following section details a heuristic approach for the prediction of L , wherein the correction factor λ can be achieved without scarifying any part. For instance, a data-driven neural network performs defect-free welding for arbitrary rib-web geometries. To simplify the procedure of generating experimental training data as low as possible, process parameters were unchanged and the number of ribs at a junction was limited to four at most.

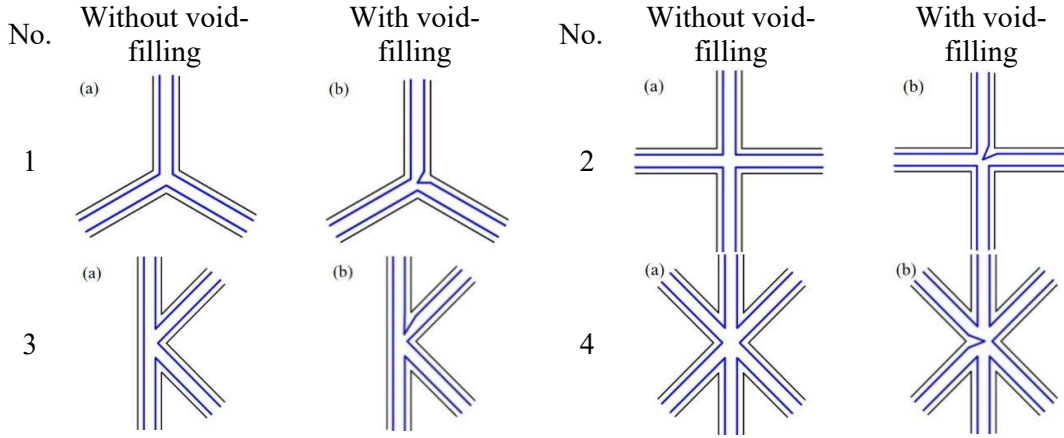


Fig. 31. A comparison between (a) standard contour tool path and (b) corrective contour tool path

4.4.2. Machine learning approach for void filling

4.4.2.1. Tolerance for the shifting distance

As mentioned in the previous section, the deficit of material can be compensated through measuring L from experimental results. When \overline{PP}_N^* is larger than L , voids can be filled. It is essential to find the smallest value of \overline{PP}_N^* that enables void filling at the conjunction. To estimate the lower limit, the junction in Fig. 30 was used, and \overline{PP}_N^* increased gradually from 0.0 to 30.0 mm with a step size of 1.0 mm. After 12 layers of deposition, the resulting specimens were milled flat from top to bottom with a cut depth of 0.5 mm until voids were visible. The possible void area (A_{void}) was measured by means of a DFC209 HD camera and a Leica DFC290 stereomicroscope at a magnification $\times 0.65$. The lower limit was used as the tolerance for the machine learning process.

4.4.2.2. Training an artificial neural network with experimental data

To estimate L from the configuration of the junction, a supervised machine learning approach was applied. The algorithm can learn from data without relying on a rules-based programming. The artificial neural network (ANN) technique was used to find the correlation between variables and enabled predictions of the new output variable. The training data includes the number of turning points (η), the configuration of junctions, and an output variable of L . The network was trained from experimental data. With three or four ribs connected at a junction, eight groups of junctions were categorized via the number of ribs and the number of equal angles. For example, there was only one case with three turning points and three equal angles. Using the ANN, L can be expressed as a function of η , and the four angles. With a three-rib junction, the last angle was set to zero.

$$L = \text{net}(\eta, \theta_1, \theta_2, \theta_3, \theta_4) \quad (4.7)$$

To parameterize an arbitrary junction, four angles were arranged in descending order, so that θ_1 was the largest angle. All 63 junction geometries were listed and deposited. The full data can be found in Appendix A1. 60 random geometries were selected to train the ANN while the remaining 3 geometries were used to validate the ANN. Each geometry was welded with five layers. The lengths of the resulting voids were measured by means of a digital caliper. To validate the proposed method, the value of L was first obtained from the experiments. Then all geometries with 12 layers were deposited with adaptive void-filling paths. The experimental results show that there was no presence of voids and valleys.

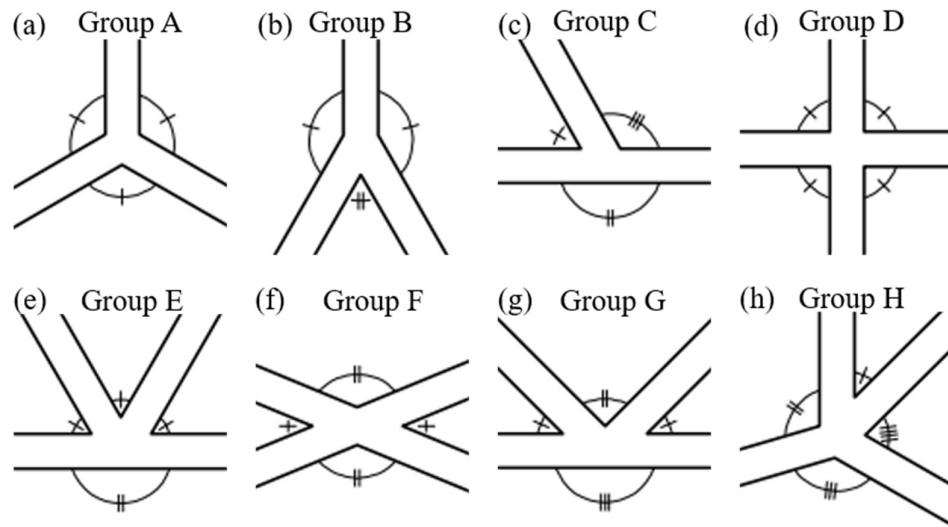


Fig. 32. The types of junctions considered: (a) three ribs with three equal angles; (b) three ribs with two equal angles; (c) three ribs with different angles; (d) four ribs with four equal angles; (e) four ribs with three equal angles; (f) four ribs with two-pair of equal angles; (g) four ribs with one-pair of equal angles; (h) four ribs with different angles (h)

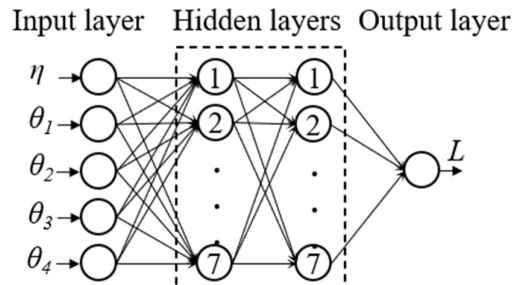


Fig. 33. A schematic architecture of the ANN

The training process was performed in MATLAB with the *nntaintool* tool. The ANN architecture is illustrated in Fig. 33. The ANN has three layers: input, hidden, and output layer.

The input layer has five variables, and the output layer performs the void length. Two hidden layers were found by means of computational experiments, with seven neurons revealing a suitable network architecture. After testing many algorithms, the Bayesian Regularization [169] was chosen for use as the training algorithm due to its superior performance.

4.5. Evaluation of tensile properties

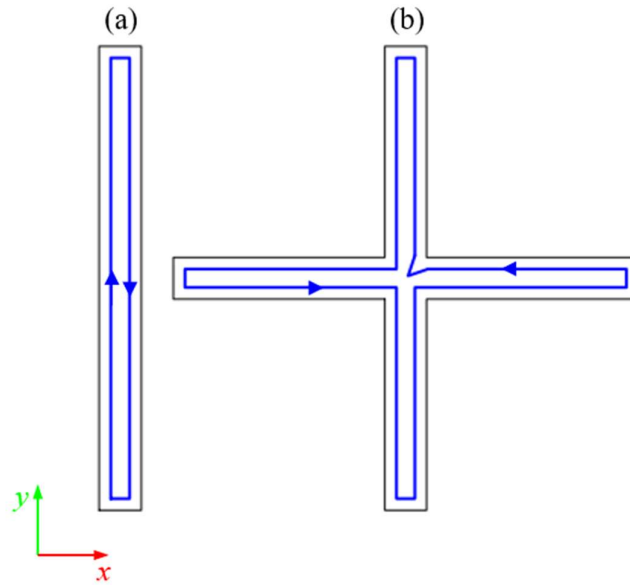


Fig. 34. The tool path for a layer of the tensile testing samples: (a) wall; (b) cross feature

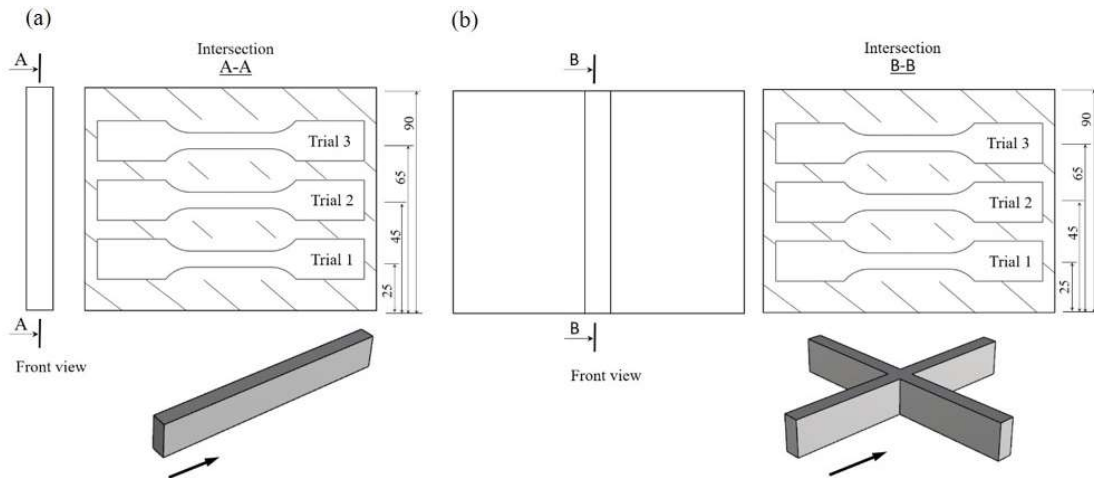


Fig. 35. Preparation of tensile specimens: for the thin wall (a); for the cross feature (b)

Tensile tests were performed in order to investigate the mechanical properties of deposited parts. These tests evaluated ultimate tensile strength (UTS), yield strength (YS) and maximum elongation. It was found that thermal history has a great impact on the anisotropy of mechanical properties [137]. Therefore, the tensile test was carried out on specimens extracted from straight

walls and from a cross structure with a single vertex at different heights. A wall and a cross shape were manufactured with the same process parameters, as is reported in Table 10. Fig. 34 depicts the tool path for the examined geometries. The cross has four turning points in the vertex area, so the void-filling function was applied. Metal parts are 90.0 mm in height, with a wall width of 9.0 mm. Tensile specimens were extracted at three positions, as illustrated in Fig. 35.

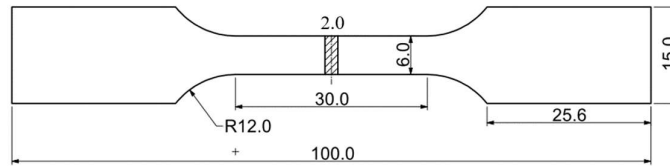


Fig. 36. A technical drawing of the tensile specimen

The dimensions of tensile specimens follow a DIN 50125 standard [170], as reported in Fig. 36. The tensile tests were carried out by means of a uniaxial tensile testing machine called ‘Inspekt 100’ with an extensometer at room temperature.

4.6. Experimental results of the tool path generation for lightweight structures

4.6.1. Evaluation of waviness and effective wall thickness

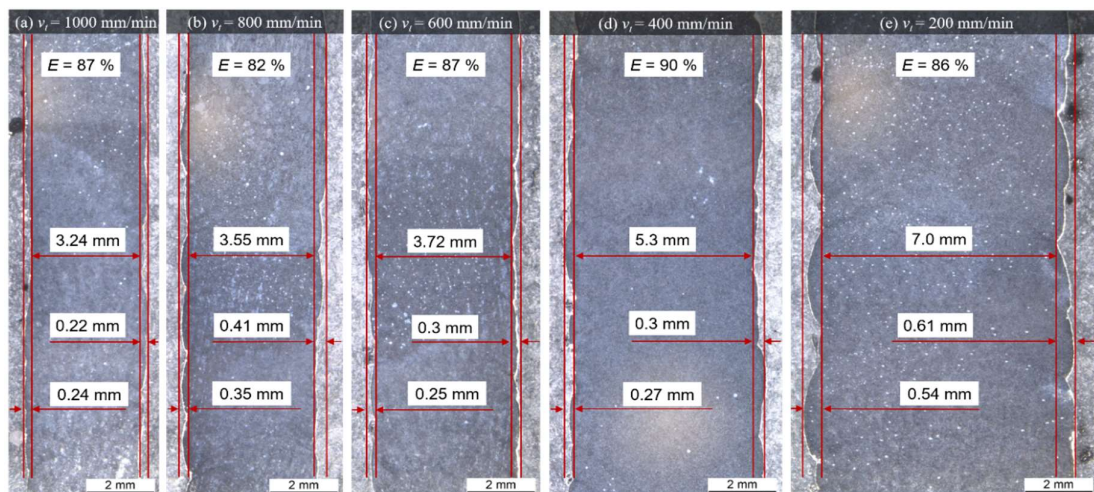


Fig. 37. Macrographs of the wall cross sections

Fig. 37 shows macrographs of single-bead walls welded with varied travel speeds (v_t). The bead width is in the range of 3.0 to 7.0 mm and the waviness increases accordingly from around 0.3 mm to 0.6 mm. With double beads, the wall thickness will be from about 5.4 to around 11.7 mm. For instance, for multi-bead deposition the bead width is at about 5.3 mm at a travel speed of 400 mm/min with an overlapping length of about 3.6 mm ($l = 2/3w$). As a result, the computed wall thickness is approximately 9.0 mm with two overlapping beads. A two-bead

wall was deposited using two adjacent weld beads with 20 layered. Fig. 38 illustrates a macrograph for the two-bead wall at the selected travel speed. The wall thickness was evaluated to be about 9.0 mm, and the waviness compares to those obtained with a single bead. To conclude, the experimental results prove that multi-bead deposition does not affect waviness.

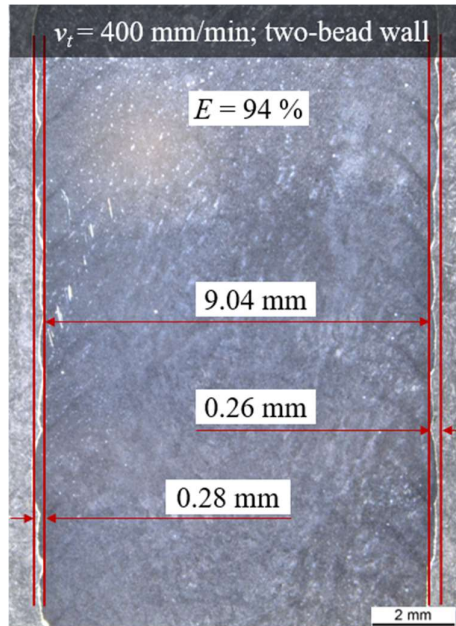


Fig. 38. Macrographs of the two-bead wall cross sections

According to Jhavar et al. [171], the deposition efficiency (E) is calculated as the ratio of the total remaining material to the deposited material. As can be seen, the deposition efficiency is above 82% for single-bead walls and is even higher for multi-bead deposition. In fact, two-bead walls value at 94% efficiency where v_t equals to 400 mm/min.

4.6.2. Evaluation of the geometrical void filling criterion

A comparison of performances can be found in Fig. 39 between the standard contour tool path and the adaptive void-filling tool path. The former yields a valley and two voids. From the measured value, λ is computed. One of the four turning points on the examined junction was chosen to perform the correction onto each layer. Voids can be compensated with the adaptive void-filling tool path.

Fig. 40 depicts the side view of the metal part. The height at the junction of the two strategies was compared using Δh as the deviation. It is important to note when employing the standard strategy that there is a valley and Δh is negative. Contrarily, the proposed strategy yields a peak due to an excess of deposited material. The development of peaks might not add up to a height

that would jeopardize the deposition process. Small peaks are tolerable when the height of the rib-web structure is low, but voids are not.

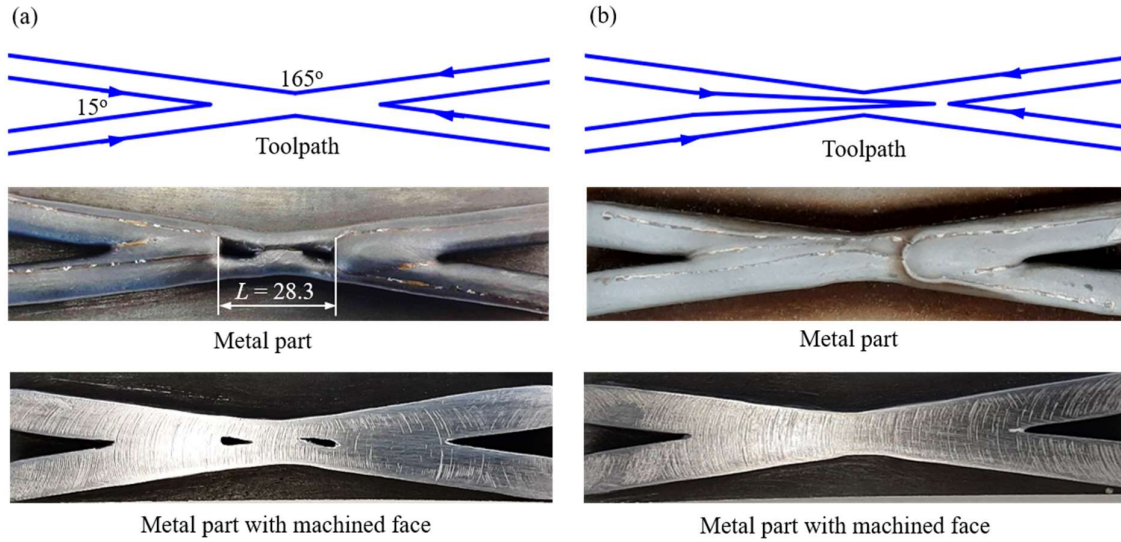


Fig. 39. Performance of an example: (a) tool path without correction and (b) tool path with correction

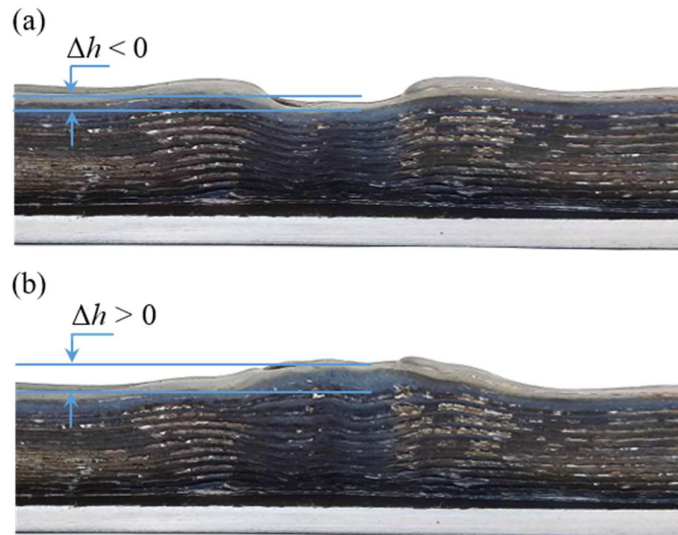


Fig. 40. A side view of the metallic part: (a) without correction; (b) with correction

The metal parts, which were examined and deposited with 12 layers, are presented in Fig. 41. The process parameters for these parts are reported in Table 10. The metal part could not be filled in the junction with the standard contour tool path, thus introducing voids in all cases. The first configuration with three ribs yielded a small void and the configuration with six ribs produced a much larger void. For junctions with four ribs, the k-shaped configuration revealed

a larger void than was seen for cross-shaped geometry. Voids are compensated for when the adaptive tool path strategy is utilized, confirming the correction strategy as a sufficient choice.

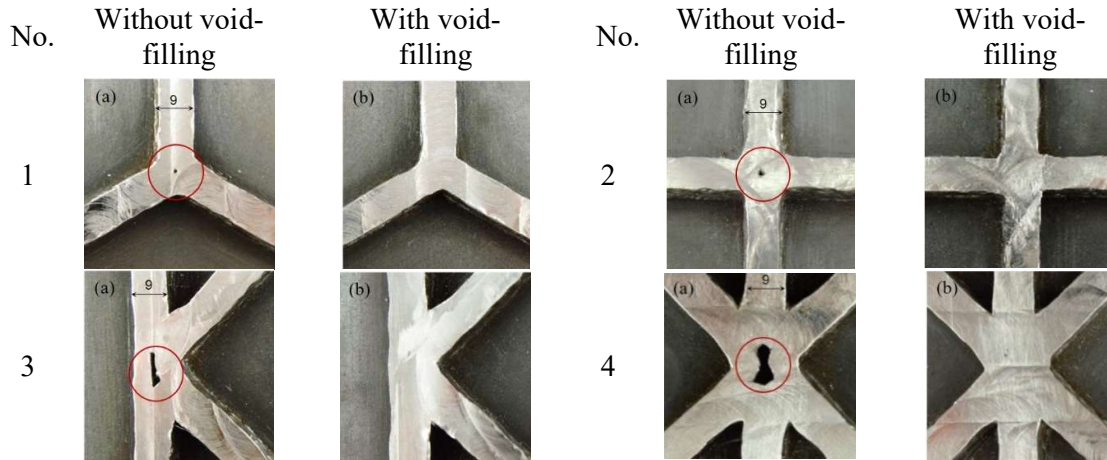


Fig. 41. Results for various junction geometries: (a) standard contour tool path and (b) adaptive void-filling tool path

4.6.3. Performance of the ANN

4.6.3.1. Tolerance

Fig. 42 illustrates four typical cases with different \overline{PP}_N^* . The void gets smaller when \overline{PP}_N^* is increased. The metal part had two large voids with the original tool path, and a small void for \overline{PP}_N^* equaling 26.0 mm. For one step size further, the metal part revealed no voids. The lower tolerance was the deviation of the most suitable value (27 mm) for \overline{PP}_N^* and L (28.3 mm), which is -1.3 mm.

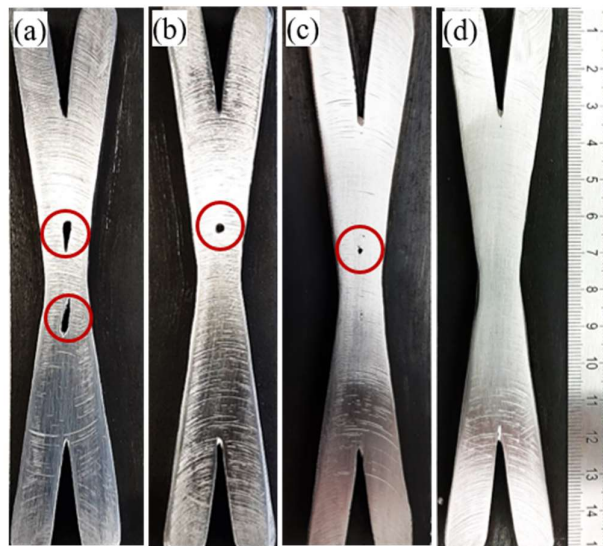


Fig. 42. Junctions with different \overline{PP}_N^* : (a) 0.0 mm; (b) 25.0 mm; (c) 26.0 mm; (d) 27.0 mm

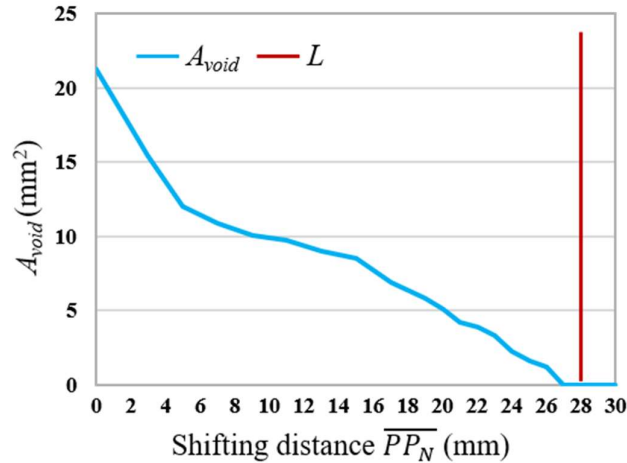


Fig. 43. The influence of the shifting distance on void area

Fig. 43 indicates the implications of the shifting distance on the void area with L is the measured void's length by a caliper. As can be seen, there is a drop in the void area from about 21.0 to 0.0 mm^2 when increasing \overline{PP}_N from 0.0 to 27.0 mm. This example can be considered as one of the most essential junctions in rib-web structure, suggesting that the lower tolerance that was calculated from this situation is also the general lower tolerance for all conjunctions, yielding the most outcomes with the selected process parameters.

4.6.3.2. Training ANN with experimental data

Fig. 44 indicates the relationship between the output and the target through regression plots. The scatter plot presents values of two variables for a set of data. The horizontal axis shows the desired value, which is experimental data, while the predicted values obtained from ANN are represented in the vertical axis. The experimental values and the predicted values are ideally equal, with the perfect trend line developing as an inclined line at an angle of 45° (dashed lines in Fig. 44). In this case, the line is quantified by an R-value of 1.0. However, even a significant value does not indicate that the trained network is realizable. The side effect of large R-values is an issue with overfitting. This problem occurs when the transfer function creates weights and biases that can only estimate existing data but not foreign data [172, 173]. Overfitting of ANN is problematic in machine learning. To investigate whether the ANN is overfitted or not, three junctions were randomly chosen from the full training data that were not used in the training process and other 60 training junctions were used to establish the ANN and the three remaining junctions were used for validation, as reported in Appendix A2. It can be concluded from the

trend line and R-value from Fig. 44 that the ANN established proper rules between the input and output layer.

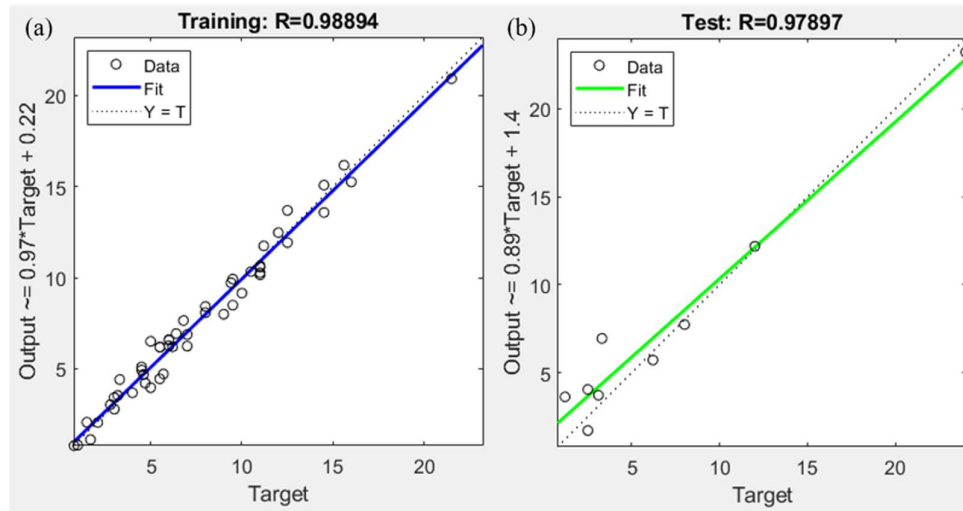


Fig. 44. Regression: (a) training; (b) test

Table 11 Validation of the ANN

No.	Group	Target (mm)	Output (mm)	ΔL (mm)
1	F ₇	24.5	24.42	-0.08
2	H ₃	5.5	6.3	0.8
3	H ₁₅	7.0	7.93	0.93

Table 11 presents the validation result for three geometries. The difference between the output and target is denoted as ΔL . The ANN can compute new data, and the deviation is within 1.0 mm. With significant R-values and no overfitting, this means that the trained ANN can predict the void length of foreign configurations.

4.6.3.3. The determination of an optimal training data set

In machine learning, the more sample data there is, the more accurate the network. However, experimental data is costly and time-consuming. This section presents a procedure to optimize the number of training samples based on the full data set gathered from 63 welded junctions. The reason for this approach was to establish a training data set that satisfies specific conditions. As stated in the previous section, -1.3 mm is the maximum lower tolerance that is allowable. Every prediction that produced a prediction error (ΔL) higher than this allowance was also accepted. To determine the sample size, samples are randomly drawn from the full data without repetition. Those selected were then applied to train the ANN while the rest was used to validate the ANN. A maximum of 1000 repetitions took place during the process of picking and training. As soon as ΔL satisfied the condition, the process ended. 60 junctions were employed for

training, and three for the validation. The process continued by reducing one unit at a time until ΔL could not satisfy the condition. At 45 junctions, a qualified ANN could not be established, thereby proving 46 samples to be the optimal sampling size, as reported in Appendix A3. The first 46 samples were for the learning process and the remaining were for validating.

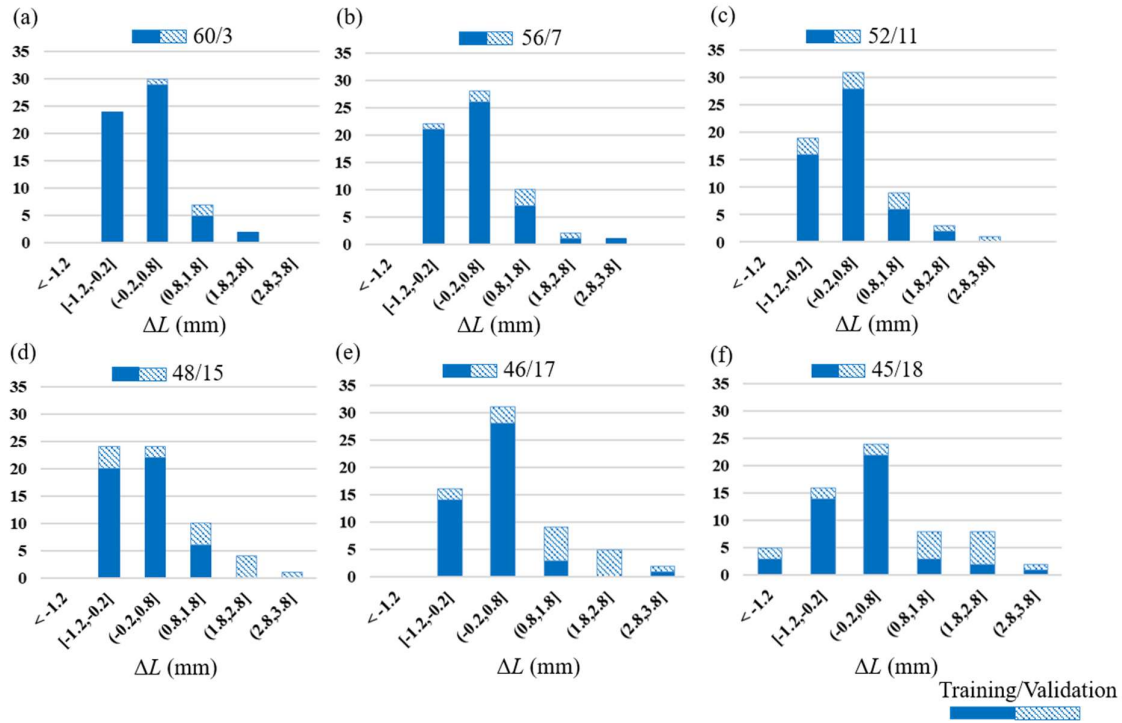


Fig. 45. Error histograms for various sets of training / validation data

Fig. 45 indicates the error histogram for six typical trials in the optimization process. The majority distributes from -1.2 to 0.8 mm. The first trial had the best performance, with errors ranging from -1.2 to 2.8 mm. The error distribution became larger when the number of sample data decreased. By reducing the amount training data from 63 to 46, the process of generating training data became simpler and less expensive.

The proposed classification scheme for junction types is applicable to arbitrary rib-web structures. However, the optimal training data number may not be sufficient when applied to other materials and experimental set-ups. Nonetheless, the process of generating training data can begin with the optimum training set in case of a new material or a different experimental set-up. Some extra validation cases are needed to ensure void-free deposition. If these circumstances are not achievable, one additional sample can be added to the training data set and the validation repeated. The procedure repeats until the desired model accuracy for void-free deposition is achieved.

The ANN should only be established if a variety of part geometries are produced. When the WAAM system is used within variant-rich production of rib-web parts, all possible cases must be covered by training an ANN. This can help produce a new variant with minimal lead time. To produce the same rib-web geometry, a defect product can first be deposited to produce the error, which will yield underfillings. Measuring the length L of the void in each vertex for the correction that will enable void-free fabrication.

4.6.4. Tensile properties

The mechanical properties of the straight wall were used as a reference to evaluate the cross shape. Fig. 46 plots the three charts of YS, UTS and elongation along the growth direction from the bottom to the top. Table 12 summarizes their average values and shows that the average values of the cross shape are slightly higher than those of the straight wall.

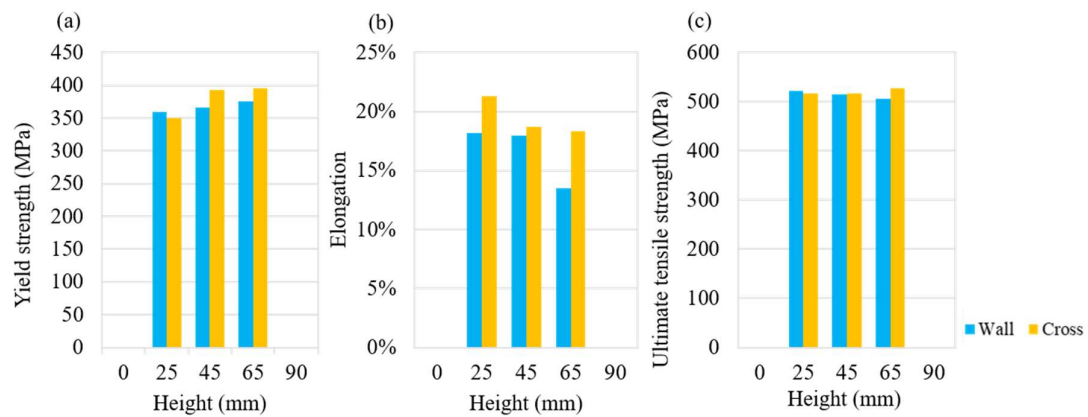


Fig. 46. A comparison of (a) yield strength, (b) elongation, and (c) ultimate tensile strength

The yield strength produces an upward trend over the height. For instance, the YS of the deposited wall increases from 366.0 MPa to 375.0 MPa while the one from the cross shape begins with 350 MPa and increases by 45 MPa. The single weld seam formed by the solidification of the weld pool was hard and brittle [174] due to the self-quenching effect [175]. Parts manufactured by WAAM were built up gradually layer-by-layer as the heat source heated formerly deposited layers. The existing layers were affected by an annealing and softening phenomenon [126]. As such, the tensile specimens extracted at lower positions yielded lower YS than those extracted at higher positions [137]. Elongation experiences a downward trend during this experiment, with the wall decreasing by about 5% and the cross-feature decreasing by about 3%. This phenomenon can be explained by the aforementioned self-quenching effect as well as the annealing and softening effect. Contrarily, the UTS remains stable when all specimens are above 500 MPa.

Table 12 A summary of tensile properties results in rib-web structures

Sample	YS (MPa)	Std.	UTS (MPa)	Std.	Elongation (%)	Std.
Wall	367.0	6.2	513.8	6.5	16.6	2.2
Cross shape	379.3	20.8	520.8	4.9	19.4	1.3

4.6.5. Realization of the proposed method for rib-web structures

The proposed tool path generation method was validated through a rib-web structure, the dimensions of which are reported in Fig. 47. The tool path was planned using the developed algorithm. First, the slicing plane sliced the CAD model with a layer-wise manner. Then inner and outer contours were obtained based on the cross section between the slicing plane and the CAD model. The proposed algorithm calculated the offset curves from cross sections and generated a continuous tool path for each layer. The proposed method was used in each intersection until there were no more intersections left.

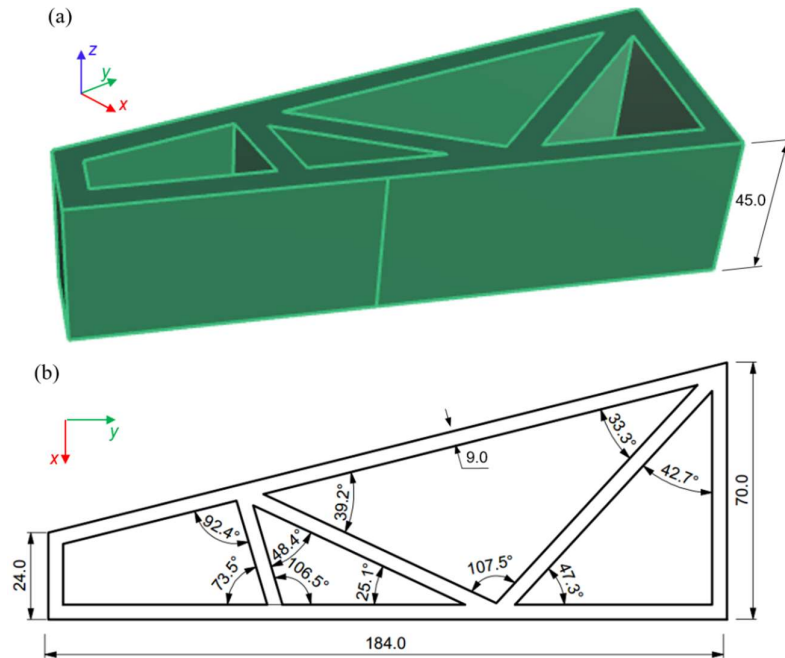


Fig. 47. The CAD model of the case study: (a) perspective view of the CAD model and (b) a typical intersection

Fig. 48 compares both the conventional and the proposed Eulerian tool path strategies. The standard method requires a great number of passes to produce the part. Each layer has four rapid moves, and the welding torch has to be frequently switched on and off, leading to defects or imperfections due to uneven weld beads. Furthermore, the part was susceptible to voids at junctions that could degrade the performance of the part. In contrast, the proposed method deposits the part by following only one welding pass within a layer, allowing for basic contours

to be transformed into a Eulerian path. The adaptive void-filling strategy is also applied to deal with void problem at junctions.

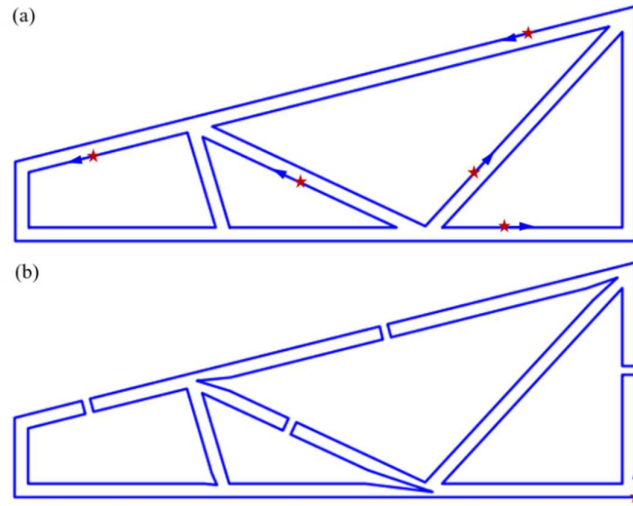


Fig. 48. A comparison of the standard contour tool path (a) and the Eulerian tool path (b). The red stars show start/stop positions.

Table 13 quantifies the number of welding passes and the process time for both tool path strategies. Due to the rapid movements between basic contours, the processing time with the standard tool path is approximately 21% longer than the one with the proposed Eulerian tool path. Occasionally machine errors occurred due to slag, wherein Human intervention was needed to clean the surfaces. On the other hand, the Eulerian tool path did not utilize any non-welding moves and the movement efficiency reached 100% without any human intervention.

Table 13 The number of welding passes and the processing time for one layer

Tool path patterns	Weld passes	Processing time (s)
Traditional tool path	5	230
Proposed tool path	1	190

Fig. 49 shows the different metal parts manufactured by using standard and Eulerian tool path. Tool paths and process parameters are indicated in Fig. 48 and Table 10, respectively. A single weld bead geometry is 5.3 mm wide and 1.8 mm high. With two-overlapping weld beads, the wall thickness was about 9.0 mm. Both parts are about 45.0 mm high. The deposition rate is over 3.0 kg/h. The metal part with the standard tool path yielded voids at all junctions. The volumes needed to fill the junctions were greater than the volume deposited for straight walls. Therefore, the standard contour tool path was unable to fill up these areas. Moreover, traces of the start and end positions (marked by red circles) could be observed on the metal part. The

developed strategy displayed a better performance when the metal part was void-free. Rib-web structures could be manufactured by following single weld beads. Due to discontinuous weld paths, the possibility for imperfections such as peaks, voids or binding errors occurred at the junctions [115] while non-welding movements could prolong the processing time. As mentioned above, the width of a single weld beads limits the rib thickness to a certain value. A zigzag motion or multi-bead deposition can be applied to applications with thicker ribs. With a zigzag welding motion, metal parts yielded worse surface quality than the ones deposited with contour paths [98], and created a high possibility of warpage [176]. The tool path strategy developed in this work transformed any arbitrary contours into a Eulerian path, which can deposit a layer with only one welding pass. Multi-bead deposition was the solution for thick walls. In this situation, a shortage of material in the junction might occur and a tool path correction would be required.

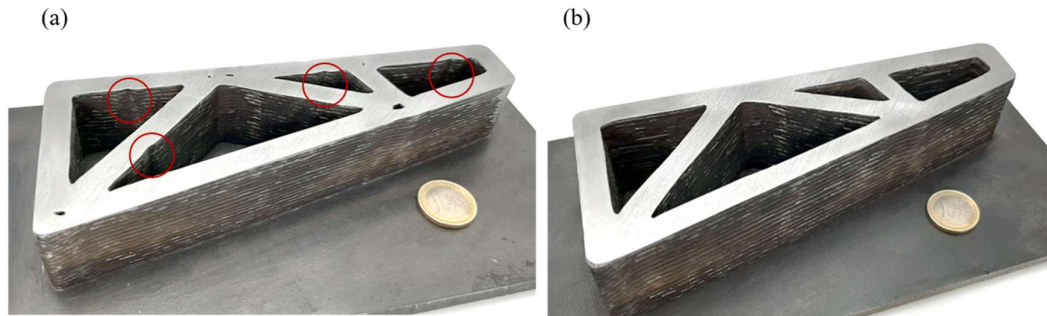


Fig. 49. The metal parts after face milling: (a) standard tool path and (b) proposed tool path

4.7. Discussion of the proposed tool path for rib-web structures

This chapter studies a correction strategy that drives the welding torch into the center of the junction with the aim of compensating underfillings. It was found that the correction step size, i.e., the correction length, can be achieved by experimentally welding a part. Identifying the correction factor for each individual junction type can be a cumbersome task. The results indicate that machine learning can be applied to learn from the experimental data and to train a neural network that represents the correction as a function of junction geometry. The network can be trained with 46 junction geometries of degrees three and four. For more complex junctions, a larger number of experiments are necessary. However, a neural network can be trained that uses a suitable correction to avoid voids for a specific material. Combined with the developed strategy to establish Eulerian paths, a tool path strategy for the deposition of arbitrary rib-web geometries seems feasible. The drawback of the proposed approach is that although voids can be compensated, peaks, i.e., excess material, occur, possibly restricting the feasible

build height. The network can be further improved by considering the peak height, i.e., by including peak information. In addition, this work should be applied when the desired wall thickness cannot be achieved with a single bead deposition and if it yields a more stable process or improves the welding motion efficiency. Some parts might not be pure rib-web structures but rather combinations of different rib-webs and bulky features. In such cases, the developed method can be extended by accounting for transitions between the varying part features.

The proposed strategy could also be applied to other AM variants, such as laser metal deposition or electron beam additive manufacturing. For such processes, the deposition process is largely different from WAAM and other correction strategies, e.g., re-melting of the junction, are possible. The process of collecting experimental data is costly and time-consuming but seems infeasible when one uses simulated results as alternative data. When experimental methods are used, noises and disturbances are included in the results making it possible to obtain accurate results for form filling. It would be much faster to conduct 46 experiments than the same number of simulations. The scope of this chapter is to introduce a continuous tool path strategy to avoid rapid movements as well as multiple starts and stops within a layer. This approach might, however, cause unfavorable temperature gradients. An interesting topic for future work would be to analyze whether the random choice of locations for reversing the welding direction should be replaced by another strategy, e.g., taking temperature distribution into account.

4.8. Summary of chapter findings

This chapter presents an innovative tool path planning strategy for the deposition of rib-web lightweight structures by wire-arc additive manufacturing processes. The main results can be summarized as follows:

- The proposed algorithm can generate a continuous tool motion for arbitrary rib-web structures by establishing Eulerian paths.
- Uneven weld beads can be avoided altogether with continuous tool motion. The welding torch is turned on at the beginning of the process and remains switched on until the part is finished.
- Due to this continuous tool motion, movement efficiency reaches almost 100%.
- To avoid underfillings in junctions, a geometrical correction strategy is developed which the aim of depositing precisely the amount of material required to fulfill the junction. The optimal path correction is produced by welding the given junction once with the geometrical correction, evaluating the void length, and updating the correction factor.

- The machine learning approach is applied to establish the relationship between junction types and void length; an adaptive void-filling strategy has been proposed, which shows a promising result.
- Using experimental data to train the network for larger production demands is tedious and unnecessary. Alternatively, superior benefits can be realized by applying the developed correction for variant-rich production. However, applying the developed correction for variant-rich production reveals superior benefits.
- For the experimental set-up, the junctions are categorized, and the optimal training data set is determined. The 46 test geometries can train a neural network, which qualifies for 17 validation cases. Sufficient training data can be gathered in just one day, which allows for welding other rib-web structures without defects.
- It should be noted that the presented methodology is transferable, and so can be directly used on other materials and set-ups, although training with dedicated geometries welded with the given set-up might be necessary.
- For the selected welding parameters, the deposition rate is over 3.0 kg/h.

Junction geometry has a complex dependence on several factors, including the deposition process that occurs within junctions, material and process parameters and multi-objective optimization (e.g., voids and peaks). Therefore, a geometrical model is not generally feasible. There is a trade-off between these two features, the work has shown that it is not possible to achieve void-free and flat surfaces in junctions. The higher the peak is, the smaller is the possibility of voids and vice versa.

5. Multi-axis deposition for WAAM processes

5.1. Introduction of the chapter

AM technology enables a free-form design and increases the complexity of parts. In conventional WAAM process, the welding torch normally moves in the x-y plane with a growth direction of +Z in the Cartesian system. Due to the properties of the WAAM process, the use of support materials and scaffold structures is inapplicable [114]. This limits the usefulness and applicability of the AM process, particularly in the fabrication of parts with overhanging or inclined features. However, it is possible to combat this drawback by using a higher degree of freedom, i.e., adding additional axes to the work piece or orienting the welding torch inline to the deposition direction. This work uses a robot-based WAAM system with additional axes of the positioner. The hardware's capability allows for the fabrication of overhanging and inclined features to be within reach.

However, a multi-axis CAM program is required to operate the multi-axis system. This chapter presents a tool path strategy to generate this kind of CAM program. With the means of multi-axis kinematics system, the welding position is maintained as a neutral position whenever possible. Details are presented in section 5.2. The control of multi axes is then introduced in the following step. New control points, angular displacements of the positioner, and the orientation of the welding torch are also explained. These data can be computed based on a normal vector of the position plane, which is perpendicular to the slicing plane. The procedure of getting this normal vector is explained in section 5.4. Derived from the CAD model, overhanging features are decomposed into subparts, each with a distinct growth direction. Section 5.5 illustrates the construction of an overhanging feature to examine the feasibility of the proposed strategy. The last section summarizes the main points of this chapter.

5.2. Welding position for WAAM

In GMAW deposition, weld seams can be produced using the pull or push method, which refers to the way the torch is moved in front of or behind the weld pool. The pull technique creates more penetration, and the push method yields a wider weld bead. The electrode wire should be perpendicular to the welding surface [53], thereby keeping the deposition angle at a neutral position.

Fig. 50 presents possible techniques for maintaining the welding position with the gun placed perpendicular to the deposition plane. In the case of the 2D layer (Fig. 50a), the gun does not need to incline. The existing hardware allowed for two ways of maintaining the relative neutral

deposition position in 3D layers. One procedure oriented the gun and the other tilted and rotated the positioner. The weld pool was in a liquid state, permitting it to flow to its surroundings due to internal forces [177]. With the first method, as seen from Fig. 50b, the weld seam is formed on an inclined surface on which fluids tend to slip due to gravitational force. Weld beads can be uneven, which can lead to rough surfaces.

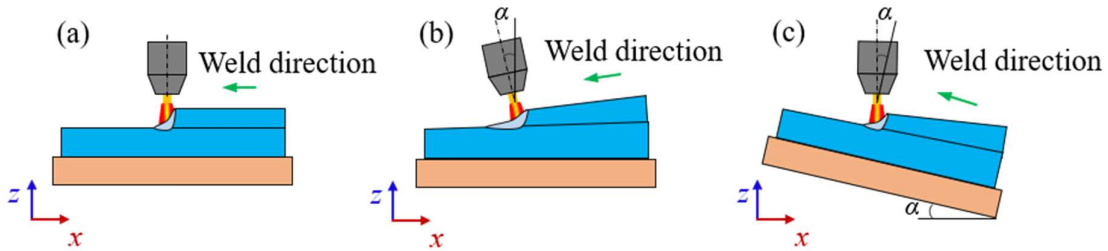


Fig. 50. The deposition angle: (a) neutral without incline; (b) neutral with torch incline; (c) neutral with positioner incline

The disturbance depends on the inclination angle (α) and the mass of the weld pool. Controlling the weld pool size is complicated and relies on many factors, such as shielding gas composition, wire-feed rate, and travel speed. Moreover, these welding parameters were chosen based on selected specification which means that changing the inclination angle was ultimately the best option. It was therefore important to reduce this angle as much as possible in order to mitigate the implication of noise. As is illustrated in Fig. 50c, a positioner could also be used to mitigate noise issues. The positioner could reorient the deposition plane to be perpendicular to the gun, reducing the impact of gravity. Both methods are used in the developed algorithm but tilting/rotating the positioner is preferred whenever feasible. The procedure of calculating the positioner's angles, new control points, and the new welding torch's orientation is presented in the coming section.

5.3. Multi-axis control for FANUC robot

A tool path is determined by moving the TCP through a series of control points. In the world frame, the position and orientation of the TCP represents those of the robot end effector or, in other words, the last part of the robot to interact with the surrounding environment. In the WAAM system, the welding torch acts as the end effector, inheriting the position and orientation from the TCP. Fig. 51 illustrates the schematic of the WAAM system with a control point (P_{RUF}) and the frame system. The RUF was virtually attached onto the positioner but reorienting the positioner to reach the neutral welding position leads to a shift in the RUF. Therefore, new coordinates of control points should be recalculated with angular displacements of the positioner and the Euler's angles for welding torch's orientation.

The relative distance and orientation of these two systems can be obtained from the previously stated specifications. Each system also has a customized frame called the user frame. The robot arm's user frame can be configured by operators, but not the positioner's user frame. The relative distance and orientation between the two frames can be represented as a homogenous matrix. The homogenous matrix includes a rotation matrix (R_{zyx}) and a translation matrix (d), as expressed by Eq. (5.1).

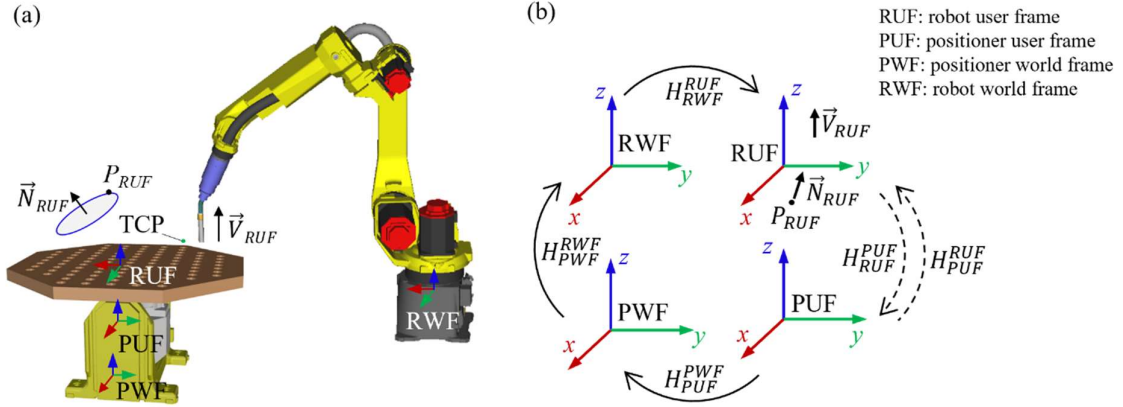


Fig. 51. A representation of the WAAM robotic system in the Cartesian coordinate: (a) representation of a control point and (b) representation of the frame system

$$H = \begin{bmatrix} R_{zyx} & d \\ 0 & 1 \end{bmatrix} \quad (5.1)$$

The basic rotation equations are indicated in Eqs. (5.2 -5.4):

- Rotation matrix, along the x-axis:

$$R_x(\theta_1) = \begin{bmatrix} 1 & 0 & 0 \\ 0 & \cos \theta_1 & -\sin \theta_1 \\ 0 & \sin \theta_1 & \cos \theta_1 \end{bmatrix} \quad (5.2)$$

- Rotation matrix, along the y-axis:

$$R_y(\theta_2) = \begin{bmatrix} \cos \theta_2 & 0 & \sin \theta_2 \\ 0 & 1 & 0 \\ -\sin \theta_2 & 0 & \cos \theta_2 \end{bmatrix} \quad (5.3)$$

- Rotation matrix, along the z-axis:

$$R_z(\theta_3) = \begin{bmatrix} \cos \theta_3 & -\sin \theta_3 & 0 \\ \sin \theta_3 & \cos \theta_3 & 0 \\ 0 & 0 & 1 \end{bmatrix} \quad (5.4)$$

- R_{zyx} can be calculated from the basic rotations. These matrices are not permuted, so any other sequences lead to different results, meaning they must adhere to the following order:

$$R_{zyx}(\theta_1, \theta_2, \theta_3) = R_z(\theta_3) \cdot R_y(\theta_2) \cdot R_x(\theta_1) \quad (5.5)$$

When the positioner changes its angles in its world frame, the coordinate of control points is different in the robot world frame, transforming the control points from RUF to PUF by H_{RUF}^{PUF} . At PUF, a new coordinate is calculated with rotation angles, consequently transforming the control points back to RUF by H_{PUF}^{RUF} . As illustrated in Fig. 51b, the homogeneous matrices between RUF and PUF can be established when there are connections between them [178]. In fact, three transformation matrices can be computed from the system. The first of these matrices is between the positioner user frame and the positioner world frame (H_{PUF}^{PWF}), the second between the positioner world frame and the robot world frame (H_{PWF}^{RWF}), and the third between the robot world frame and the robot user frame (H_{RUF}^{RWF}).

- H_{RUF}^{PUF} can be computed by multiplying known matrices:

$$H_{RUF}^{PUF} = H_{PWF}^{PUF} \cdot H_{PWF}^{RWF} \cdot H_{RUF}^{RWF} = (H_{PUF}^{PWF})^{-1} \cdot (H_{PWF}^{RWF})^{-1} \cdot H_{RUF}^{RWF} \quad (5.6)$$

- From Eq. (5.6), H_{PUF}^{RUF} can be calculated as an inverse of H_{RUF}^{PUF} :

$$H_{PUF}^{RUF} = (H_{RUF}^{PUF})^{-1} \quad (5.7)$$

- If a homogenous transformation of matrix H is represented by $\begin{bmatrix} R & d \\ 0 & 1 \end{bmatrix}$, its inverse can be expressed by:

$$H^{-1} = \begin{bmatrix} R^1 & -R^{-1} \cdot d \\ 0 & 1 \end{bmatrix} \quad (5.8)$$

With the existing hardware, the positioner manipulates the neutral welding position by rotating along its x- and z-axis. The rotation is represented as a rotation matrix. Because the z-axis places on the x-axis, any motion with respect to the x-axis will lead to a different z coordinate. The rotation matrix is denoted as R_{xz} .

- Rotation matrix R_{xz} is constructed from two basic rotation matrices Eqs. (5.2) and (5.4), with θ_x , and θ_z are unknown variables:

$$R_{xz}(\theta_x, \theta_z) = \begin{bmatrix} \cos \theta_z & -\sin \theta_z & 0 \\ \cos \theta_x \cdot \sin \theta_z & \cos \theta_x \cdot \cos \theta_z & -\sin \theta_z \\ \sin \theta_x \cdot \sin \theta_z & \sin \theta_x \cdot \cos \theta_z & \cos \theta_z \end{bmatrix} \quad (5.9)$$

To compute two unknown variables, the normal vector and the torch orientation in the positioner user frame are used. For instance, the normal vector is transformed to align with torch orientation, as represented in Eq. (5.10). With three equations, two rotation angles can be found.

$$\vec{V}_{PUF} = R_{xy}(\theta_x, \theta_z) \cdot \vec{N}_{PUF} \quad (5.10)$$

- Rotation of the substrate occurs in the positioner user frame, transforming the torch orientation from the robot user frame to the positioner user frame:

$$\vec{V}_{PUF} = H_{RUF}^{PUF} \cdot \vec{V}_{RUF} = \begin{bmatrix} a \\ b \\ c \end{bmatrix} \quad (5.11)$$

- To transform the normal vector from the robot user frame to the positioner user frame:

$$\vec{N}_{PUF} = H_{RUF}^{PUF} \cdot \vec{N}_{RUF} = \begin{bmatrix} d \\ e \\ f \end{bmatrix} \quad (5.12)$$

Substituting Eqs. (5.11) and (5.12) into Eq. (5.10), θ_x and θ_z are computed from Eq. (5.13) with a, b, c, d, e, and f are constant, and R_{xz} can be established. Details of this procedure are reported in Appendix B.

$$\begin{cases} d \cdot \cos \theta_z - e \cdot \sin \theta_z = a \\ d \cdot \cos \theta_x \cdot \sin \theta_z + e \cdot \cos \theta_x \cdot \cos \theta_z - f \cdot \sin \theta_x = b \\ d \cdot \sin \theta_x \cdot \sin \theta_z + e \cdot \sin \theta_x \cdot \cos \theta_z + f \cdot \cos \theta_x = c \end{cases} \quad (5.13)$$

- To transform the control point from the robot user frame to the positioner user frame:

$$P_{PUF} = H_{RUF}^{PUF} \cdot P_{RUF} \quad (5.14)$$

- The positioner tilts and rotates in the positioner user frame with angles of θ_x , and θ_z , respectively, the control point is transformed by:

$$P_{PUF_Rot} = R_{xz} \cdot P_{PUF} \quad (5.15)$$

After tilting and rotating, the control point is transformed back to the robot user frame, as expressed in Eq. (5.16); P_{RUF_Rot} is the final coordinates.

$$P_{RUF_Rot} = H_{PUF}^{RUF} \cdot P_{PUF_Rot} \quad (5.16)$$

When the positioner exceeds its limits, the welding torch will compensate for this shortage by maintaining a neutral welding position.

- The normal vector is in the positioner user frame after tilting and rotating:

$$\vec{N}_{PUF_Rot} = R_{xy} \cdot \vec{N}_{PUF} \quad (5.17)$$

- After tilting and rotating, the normal vector is transformed back into the robot user frame:

$$\vec{N}_{RUF_Rot} = H_{PUF}^{RUF} \cdot \vec{N}_{PUF_Rot} \quad (5.18)$$

\vec{N}_{RUF_Rot} should be aligned with \vec{V}_{RUF} . A rotation matrix is introduced to align those two vectors by reorienting the welding torch. The robot tool frame is transformed along the z, y, and x-axes with respect to the robot world frame, as A , B , and C . The rotation angles are Euler angles. The theory can be expressed as Eq. (5.19).

$$\begin{aligned} \vec{V}_{RUF} &= R_{zyx}(A, B, C) \cdot \vec{N}_{RUF_Rot} \\ \Rightarrow \vec{V}_{RUF} &= \begin{bmatrix} R_{zyx(11)} & R_{zyx(12)} & R_{zyx(13)} \\ R_{zyx(21)} & R_{zyx(22)} & R_{zyx(23)} \\ R_{zyx(31)} & R_{zyx(32)} & R_{zyx(33)} \end{bmatrix} \cdot \vec{N}_{RUF_Rot} \end{aligned} \quad (5.19)$$

According to LaValle [179], A , B , and C can be computed from the rotation matrix, as expressed in Eqs. (5.20-5.22):

$$A = \tan^{-1} \left(\frac{R_{zyx(21)}}{R_{zyx(11)}} \right) \quad (5.20)$$

$$B = \tan^{-1} \left(\frac{-R_{zyx(31)}}{\sqrt{R_{zyx(32)}^2 + R_{zyx(33)}^2}} \right) \quad (5.21)$$

$$C = \tan^{-1} \left(\frac{R_{zyx(32)}}{R_{zyx(33)}} \right) \quad (5.22)$$

To summarize, the new coordinates of the control points can be obtained from Eq. (5.16), the angular displacements of the positioner are calculated from Eq. (5.13), and the Euler's angles of the gun are computed from Eqs. (5.20-5.22).

5.4. The decomposition algorithm

To support multi-axis deposition, each overhanging feature of the complex geometry should be sliced with a distinct direction. As such, the CAD model should be decomposed into subparts. This section presents a method to decompose complex geometries into subparts and a way to

establish a central axis for each subpart in Grasshopper/Rhinoceros. The approach consists of analyzing the differences between two consecutive layers that had been obtained by slicing the CAD model. By the nature of AM processes, there is always a default layer at the bottom of AM parts. Every cross section created from the slicing process will have a predecessor, which is called the bottom layer while the current layer is called the top layer. Each layer may contain many section curves inside. When analyzing the outer geometrical shapes between two adjacent layers, it is important to remove all section curves which were encompassed by another. Therefore, a *simplification module* was equipped with the aim of getting rid of inner section curves. A normal vector was used to guide the slicing plane. A CAD model, which contains curved feature, was an important means of manipulating the slicing direction. A *normal vector identification* module was adopted to track the curvature of the CAD model. For instance, when projecting the bottom layer onto the top layer possible scenarios included unrelated, not uniform, and uniform. Split planes were constructed to split overhanging features apart from the main body in the *decomposition module*. At the end of the process, a centroidal axis for each subpart was constructed.

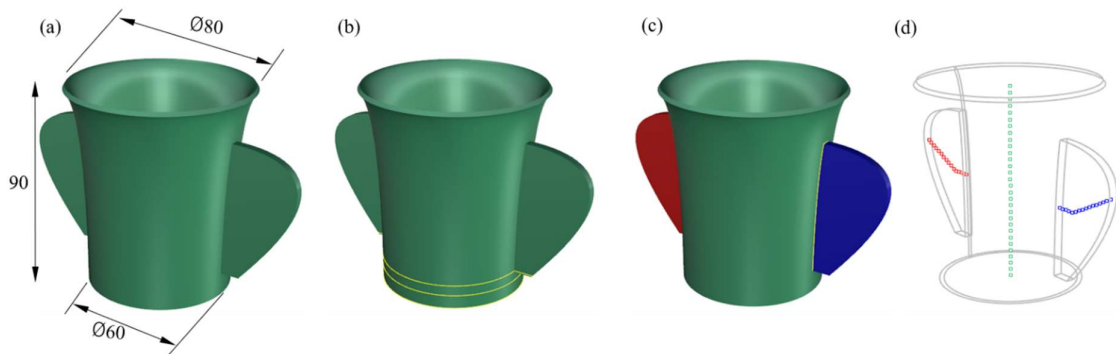


Fig. 52. An example of part decomposition: (a) CAD model; (b) model slicing; (c) split overhangs; (d) centroidal axes

The decomposition algorithm is illustrated through an example in Fig. 52. The cup has two handles, which are considered overhanging features. The algorithm first sliced the CAD model, and then split these handles. Finally, a centroidal axis was constructed for each subpart. Details of each module are explained below:

❖ Simplification module

In order to construct the centroidal axis, only the outer cross sections were taken into account. Therefore, it is important to remove all inner curves, as shown in Fig. 53. This module makes the geometrical data simpler to analyze.

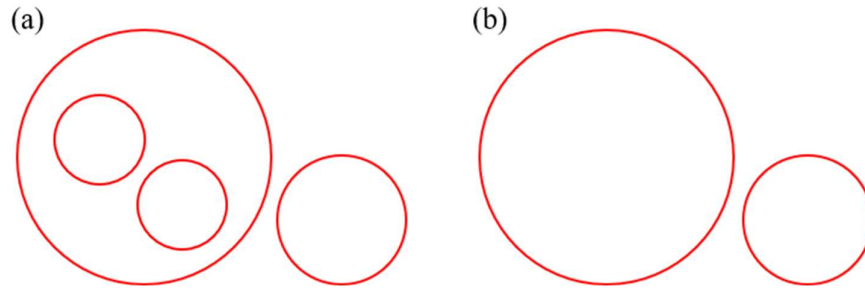


Fig. 53. A simplification: (a) before removing inner cross sections and (b) after removing inner cross sections

❖ Normal vector identification

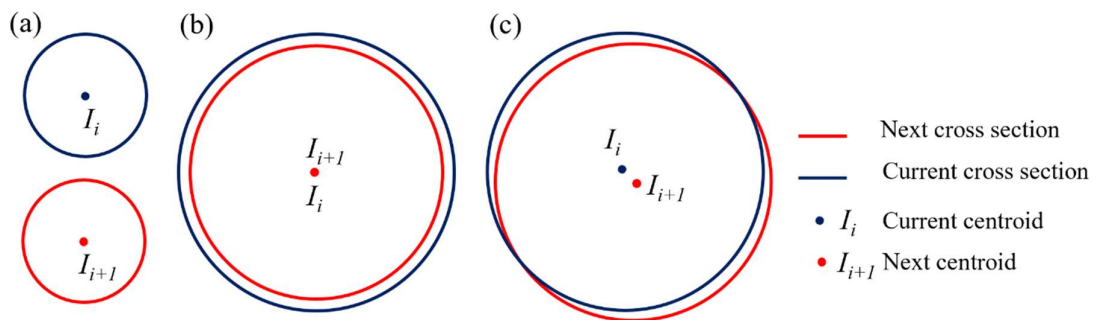


Fig. 54. Scenarios between two consecutive cross sections (a) unrelated; (b) uniform; (c) not uniform

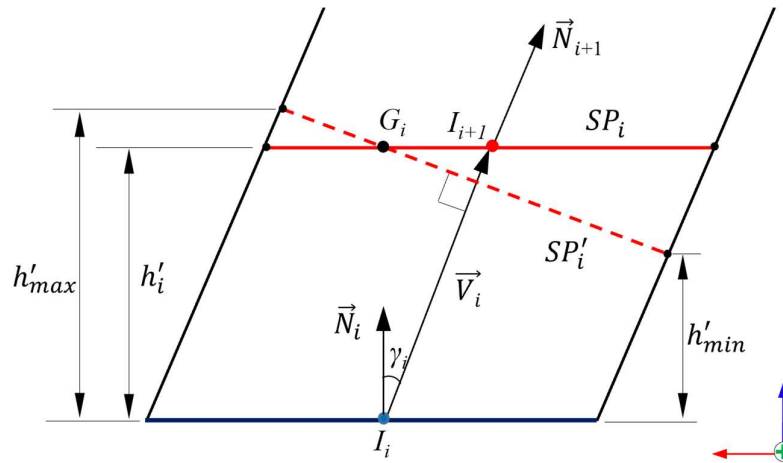


Fig. 55. Normal vector identification

To track the curvature of a CAD model, the slicing is manipulated based on the local geometry. After removing all inner cross sections, the bottom layer is projected onto the plane of the top layer. There are three main scenarios. Fig. 54a reveals that two layers are not related to each other. Fig. 54b indicates that I_i and I_{i+1} are coincident, hence the slicing direction remains unchanged. On the other hand, Fig. 54c shows differences when I_i and I_{i+1} are not coincident.

In this scenario, the slicing plane might change the slicing direction. I_i obtained from each slice is used to construct the centroidal axis.

Fig. 55 illustrates two adjacent slices from Fig. 54c. The normal vector (\vec{N}), which is always perpendicular to the slicing plane (SP), is used to navigate SP through the slicing process. This normal vector may change when I_i and I_{i+1} are not coincident.

- \vec{N} of the current layer is the \vec{V} of the predecessor layer:

$$\vec{N}_i = \vec{V}_{i-1} \quad (5.23)$$

- G is a guessed point, which is used to determine the slicing plane (SP), and G is defined by transforming I_i a certain thickness (t) with the direction of \vec{N} :

$$G_i = I_i + t_i \quad (5.24)$$

- After intersecting SP and the CAD model, the centroid of the top layer was determined, allowing for the angle vector to be computed, as expressed in Eq. (5.25):

$$\vec{V}_i = I_{i+1} - I_i \quad (5.25)$$

Algorithm: pseudo code for adjusting moving distance h'

h'_{max} and h'_{min} are the maximum and minimum height within a CAD slice

h_{max} and h_{min} are the maximum and minimum height that can be deposited

If $h'_{min} < h_{min}$ then

$$h' = h' \frac{h_{min}}{h'_{min}}$$

Else if $h'_{max} > h_{max}$ then

$$h' = h' \frac{h_{max}}{h'_{max}}$$

End if

Fig. 56. Pseudo code for adjusting moving distance

In this way, the angle between two vectors is calculated. If γ is larger than β , then the SP is transformed to be perpendicular to the angle vector with a center point at G . The new slicing plane (SP') intersects the CAD model and new parameters are recalculated such as I_i and \vec{V} , so that γ is close to zero.

$$\gamma_i = (\vec{N}_i, \vec{V}_i) \quad (5.26)$$

When γ is too small, it is not necessary to transform the slicing plane, thereby limiting the angle of γ . In this section, β is 0.10. When the slicing thickness (h') is large, the procedure executes productively, but for large curvature features, the normal vector can be inaccurate. To optimize the process, conditions should be set to adjust the moving thickness automatically, as expressed below:

❖ CAD model decomposition module

Fig. 57 depicts a showcase of how to take off overhanging features. At every slice, the bottom layer is projected onto the top layer (Fig. 57a). This is executed with the assumption that the projected curve has n control points, and each control point has an associated point on the top curve (Fig. 57b). Two split lines are constructed based on these associated points, as shown in Fig. 57c. The top layer is divided into three regions (A_1 , A_2 , and A_3). For the following slice, A_1 is considered as the bottom layer. Moreover, the first and the last split lines are used to establish a split plane so as to split the overhanging feature apart from the main body.

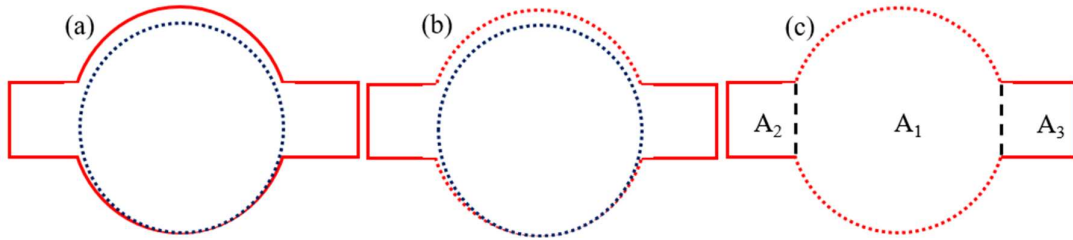


Fig. 57. Split lines determination: (a) step 1; (b) step 2; (c) step 3

5.5. Experimental results for the multi-axis deposition strategy

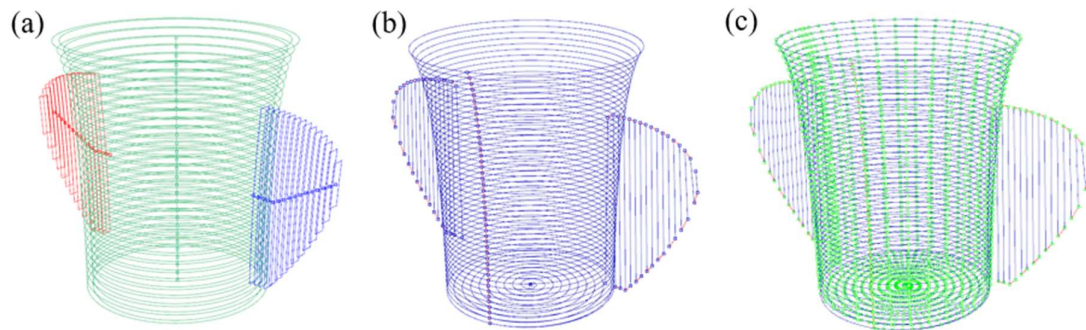


Fig. 58. Trajectory planning: (a) slicing sub-parts; (b) tool path; (c) control points extraction

The CAD model from Fig. 52 was used as a case study for the multi-axis deposition strategy. After decomposing the CAD model, each sub-part was sliced with a distinct direction. Fig. 58

shows the sequence of obtaining the coordinates of control points and the normal vector. The examined part was manufactured by a single weld bead, and the average curves between cross sections were used as the tool path patterns, as shown in Fig. 58b (blue lines). After that, control points and corresponding normal vectors were extracted into a text file as seen in Table 4. A MATLAB script was developed to calculate data for the CAM program such as new coordinates, angles for the positioner, and the Euler's angles for the torch's orientation, as illustrated in Table 14.

Table 14 The input data for a multi-axis CAM program

Layer index	TCP coordinates			Positioner angle		Torch's orientation			Weld_En
	X (mm)	Y (mm)	Z (mm)	θ_z (degree)	θ_x (degree)	A (degree)	B (degree)	C (degree)	
1	50.0	0.0	0.0	0.0	0.0	0.0	0.0	0.0	On
1	49.8	-3.6	0.0	-3.085	-0.447	0.0	0.0	0.0	On
...
n	-37.2	0.0	80.32	0.0	0.0	0.0	0.0	0.0	Off

Table 15 Material and process parameters for the experiment in multi-axis deposition

Process parameter	Value
Material	AlSi5
Wire diameter (mm)	1.2
Shielding gas	100% Ar
Flow rate (L/min)	18
Travel speed (mm/min)	600
Wire feed rate (mm/min)	2200
Stick-out length (mm)	12

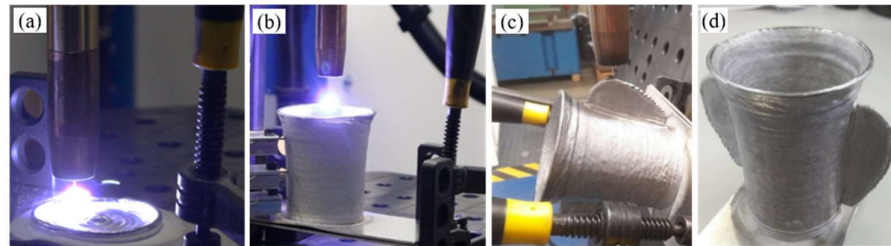


Fig. 59 Building overhanging features: (a) building the bottom; (b) building the cylinder; (c) building the handles; (d) finished part

Table 15 presents the material and process parameters for the case study. The part was deposited on an aluminum substrate ($80 \times 160 \text{ mm}^2$) with a thickness of 2.0 mm. The robot user frame was set at the center point of the substrate with the tick-out length of 12 mm. Initially, the wire feed rate was set to 4.6 m/min for the first layer and the substrate was at room temperature making the welding energy higher than normal. Fig. 59 presents the manufactured steps of the case study. The bottom of the part was built by following a spiral pattern, and the cylinder was

manufactured by following contour pattern with a layer thickness of 1.1 mm. The two overhanging features were deposited by moving the positioner to maintain the neutral welding position.

5.6. Summary of chapter findings

This chapter introduced a tool path strategy to generate CAM programs for WAAM multi-axis deposition. The proposed strategy was developed in Grasshopper/Rhinoceros and MATLAB. Due to the nature of the WAAM process, support materials and scaffold structures were inapplicable for the fabrication of overhanging and inclined features. To overcome this limit, a multi-axis deposition strategy was developed on the robot-based WAAM system that consisted of a six-axis robot arm equipped with the CMT welder. The substrate was mounted onto the positioner. Each overhanging or inclined feature should be deposited with a distinct direction; hence, the decomposition algorithm has been proposed to detect overhanging features. New coordinates of control points, positioner's angles, and torch's orientation were calculated to maintain the neutral welding position for each subpart. In addition, homogeneous matrices between the robot arm and the positioner were established then used to convert the relative position of control points between these groups. This theory has been validated by the construction of an overhanging feature. For small overhangs, such as the cylinder, the part is executed on a three-axis planar deposition. For large overhangs, such as the handles, the positioner tilts/rotates to a certain angle to ensure a neutral welding position. The multi-axis deposition strategy provides another choice to manufacture overhanging features while reducing processing time, material waste, and small production batch sizes.

6. Tool path generation for curved thin-walled structures with shrinkage compensation

6.1. Chapter introduction

This chapter further extends the application of the multi-axis deposition through a novel method of producing curved thin-walled hollow structures by WAAM. With shapes including bent pipes and pipe elbows, these structures can be used as fittings, lightweight space frames in vehicle, machine structures, and construction engineering. Bent hollow profiles are typically produced by metal forming processes such as press bending [180], rotary draw bending [181], three-roll push bending [182], and induction bending [183]. These forming processes require tooling and appropriate semi-finished products produced by extrusion, shape rolling or roll-forming [184, 185]. Complicated profile cross sections cannot be produced due to wrinkling and fracture. Although casting can deal with these kinds of shapes, the process of doing so requires substantial lead time to ensure the complete filling of the mold and to achieve a defect-free solidification. Limited castability of thin-walled sections restrict the range of geometries that can be produced.

A new manufacturing process using WAAM can produce complex bent hollow structures. These structures can be manufactured by welding non-uniform layers, meaning the travel speed is manipulated to change the melting volume. A slow travel speed causes more injected material and vice versa. To realize this, curved hollow structures were deposited with multi-axis deposition using the FANUC robot system with a GMAW welder from Fronius. The tool path was generated by slicing the CAD model along the curved profile. The slicing plane was perpendicular to the central axis, producing non-uniform slices. Material shrinkage and distortion are common issues in GMAW processes. A novel compensation algorithm was developed to ensure geometric accuracy.

The next section of this chapter will present the geometries used to examine and validate the proposed method. Section 6.3 introduces WAAM process with multi-axis deposition and non-uniform layers. The subsequent section will cover evaluation methods used for welding defects and geometric accuracy are presented. Section 6.5 details an offline compensation approach based on experimental data to compensate for material shrinkage and distortion. Experimental results for the developed methods are presented in section 6.6. The following section discusses about the combination of multi-axis deposition and non-uniform layers as well as a compensation strategy. The final section concludes findings, achievements, and the novelty of the proposed strategy.

6.2. Examined geometries

The proposed algorithm was examined through four curved thin-walled hollow structures, as shown in Fig. 60. The test geometries were designed with different dimensions and geometries. For example, Part I is a bent pipe with a uniform circular cross section of 100 mm diameter and a bending radius of 150 mm. Part II is an irregular circular cross-section and a bending radius of ~ 314 mm while part III is a combination of a rounded-square section and a bent tube. Part IV has a hexagonal cross section with the curvature of 250 mm. The algorithm will be described using the bent tube of part I.

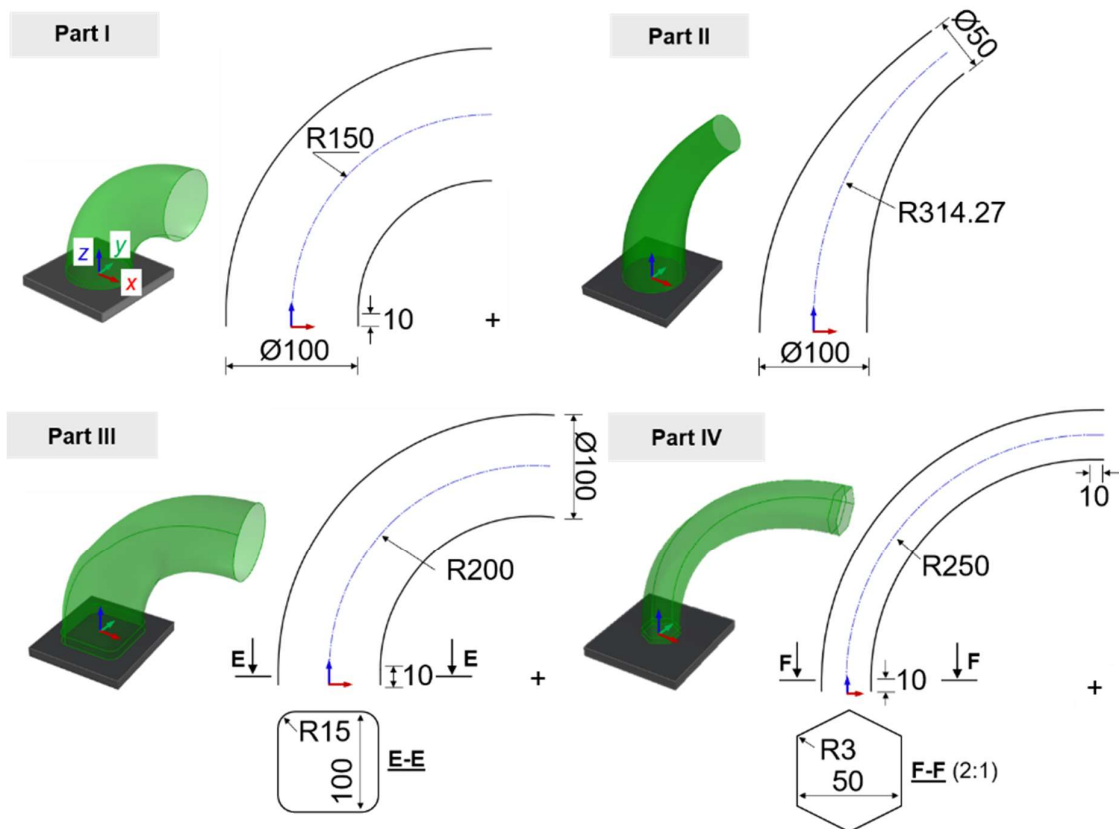


Fig. 60 A nominal model and technical drawing of examined structures

6.3. Multi-axis deposition with layers of non-uniform thickness

6.3.1. Tool path generation by means of the adaptive slicing algorithm of CAD geometry

Since the geometries presented in Fig. 60 are overhanging features, the slicing plane should follow the skeleton of CAD models to get cross sections, using \vec{N} to denote the normal vector of the slicing plane. Based on the local geometry, the slicing plane was adapted so that it was

perpendicular to the axis of the profile as slicing proceeded along the geometry. The working principle of the adaptive slicing algorithm is illustrated in Fig. 61. The initial normal vector is equal to the unit vector of the z-axis. I_i denoted the area centroid of a cross section and G is a point defined by moving I_i at a distance of h' along the normal vector, so $G = I_i + h' \cdot \vec{N}$. The slicing plane is transformed with its normal vector at a distance of $\overline{I_i G}$. The slicing process ends when there is an intersection in the CAD model. Otherwise, the cross section creates an area centroid denoted as I_i . The slicing plane is transformed to be perpendicular to $I_i I_{i+1}$ at I_{i+1} . The next cross section is created by repeating this procedure. At the end of the slicing process, the layers are of irregular thicknesses.

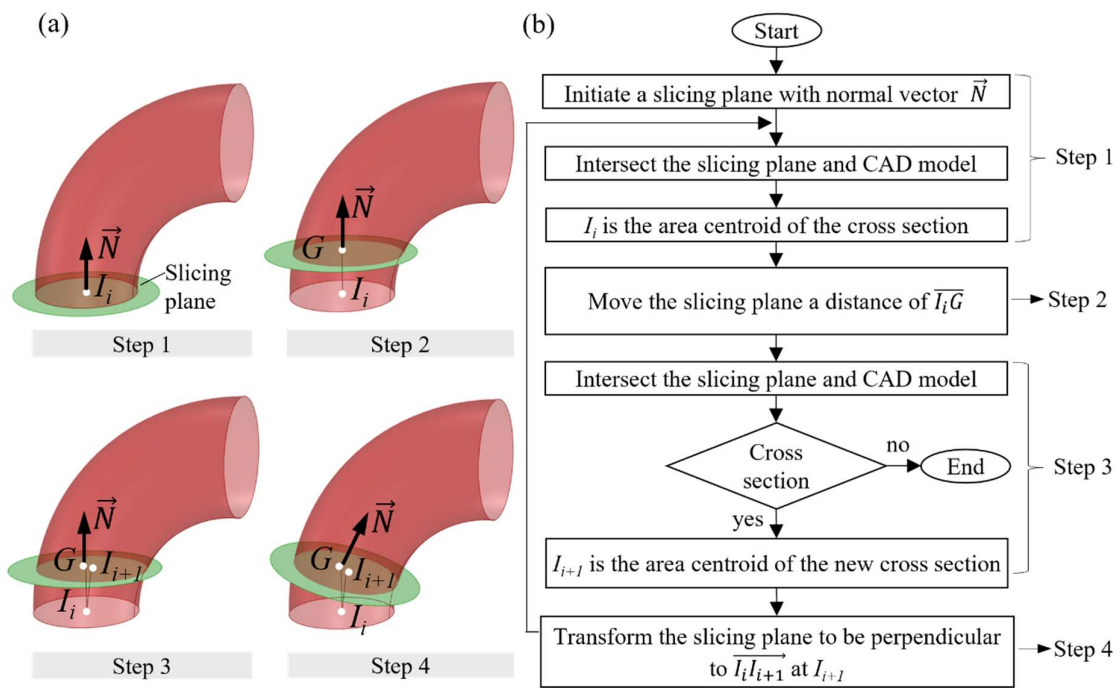


Fig. 61 The procedure of adaptive slicing algorithm: (a) schematic and (b) flowchart

It is important to note that the dimension of the non-uniform layer is limited by the nature of welding process. The bead height was reported to be in the range of from 1.0 - 2.0 mm [39]. Any layers beyond this range are not able to be deposited. The displacement distance ($\overline{I_i G}$) is consequently adjusted. When the minimum slicing thickness is smaller than the feasible minimum weld bead height, the scaling factor h' is scaled up. Contrarily, the scaling factor is scaled down when the maximum slicing thickness exceeds the maximum weld bead height, as described above in Fig. 56.

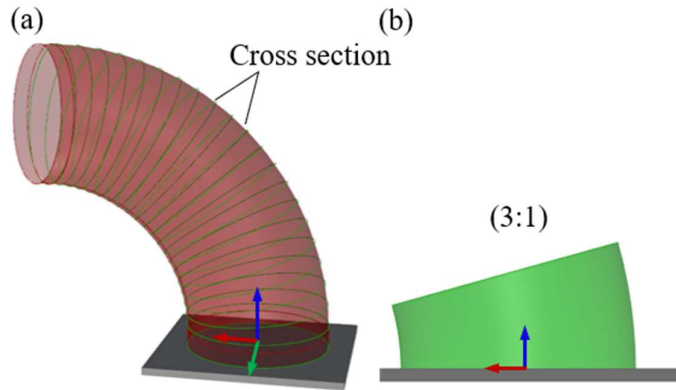


Fig. 62 A representation of the creation of 3D slices: (a) cross section and (b) 1st 3D slice

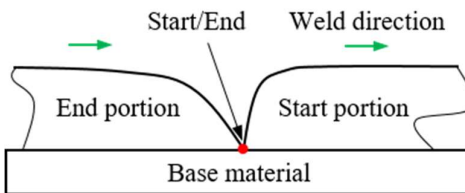


Fig. 63 A schematic of the start and end portion in a closed weld pass

Fig. 62 shows the typical non-uniform layers that result from the adaptive slicing process. These cross sections act as basic tool paths to deposit the structure, but the deposition process is discontinuous. As aforementioned, uneven weld beads are inevitable in a GMAW process when the number of welding passes increases. Defects can occur at the start and end portion of each layer, as illustrated in Fig. 63. The process is disrupted after finishing a layer and imperfections may occur. A simple strategy to overcome this problem is to establish a continuous path from the basis cross sections, which can enhance the productivity and product quality.

To evaluate the feasibility of the adaptive slicing algorithm with experimental results, four test geometries were manufactured. The setting minimum and maximum layer height are reported in Table 16.

Table 16 The maximum and minimum layer thickness for slicing the curved thin-walled models

Part	h_{max} (mm)	h_{min} (mm)
I	2.0	1.0
II	1.7	1.1
III	1.4	1.1
IV	1.6	1.1

6.3.2. Deposition of a non-uniform thickness layer

The distance between consecutive cross sections is not uniform, requiring full control over the amount of deposited material following changes in desired thicknesses. To realize this aim, a precise model should be established for the influence of the process parameters on the weld bead geometry. This section presents a procedure to construct the corresponding relationships between process parameters and weld bead geometry.

6.3.2.1. The relationship between weld bead geometry and travel speed

Weld bead geometry is controlled locally within a layer to create non-uniform layers. The dimensions of the weld depend primarily on welding parameters such as power, the wire-feed rate, shielding gas composition, and travel speed [39]. In fact, there are many factors which can be adjusted.

In the CMT process, the welding power and wire-feed rate follow the synergic line, hence the welding power is automatically manipulated according to the wire-feed rate. Moreover, a minor adjustment of the shielding gas composition can have a great, complicated impact on weld bead geometry [186] and mechanical properties, thus the shielding gas composition is unchanged during processing. There are mainly two controllable parameters: the travel speed (v_t) and the wire-feed rate (v_w). To simplify the model, only one parameter is manipulated, and the other is kept unchanged. Due to the fact that the travel speed has a greater effect on the weld bead geometry than the wire-feed rate [111], the travel speed was selected as the control factor. The geometry of a weld seam can be represented as its height (h) and width (w), but they cannot be controlled independently as only one dimension can be controlled at a time. To produce bent hollow structures, the height must be controlled, and the width of the deposited weld bead achieved accordingly.

To establish the prediction model, a function for the relation between the travel speed and the bead height is needed, as shown in Eq. (6.1). This work applies the interpolation proposed by Kosaki [187], an estimation method is used to obtain new data points within the range of a discrete set of known data points. An algebraic equation is constructed from known data points.

$$v_t = f(h) \tag{6.1}$$

To collect a set of discrete data points, single-bead walls were deposited with 20 layers in various travel speeds. The wire-feed rate was 3200 mm/min for all experiments. The travel speed varied in steps of 50 mm/min in the range of 100 mm/min to 1000 mm/min. The idle time

between two adjacent layers was 10 s and the welding direction alternated with every layer. The dimensions of the weld bead were obtained by means of a digital caliper at three positions (Fig. 72): 10.0 mm, 50.0 mm, and 90.0 mm. The measurements were carried out at room temperature.

Regarding to Eq. (6.1), a continuous function $f(h)$ was computed by a non-linear least squares regression [188]. To evaluate how well the function fits to the sample data, the R^2 (coefficient of determination) was determined. A perfect fit was indicated by going through all points and yielding the R^2 value of 1.0. In other words, the closer the R^2 value was to 1.0, the more accurate the interpolation was.

As mentioned above, the wall thickness cannot be controlled directly though the design requires a certain wall thickness. This condition must be considered in the deposition process to ascertain a suitable width. Consequently, a relationship between bead height (h) and bead width (w) was required, as expressed in Eq. (6.2).

$$w = f(h) \tag{6.2}$$

The test geometries shell models and the wall thickness are not indicated. Deriving from the relationship in Eq. (6.2), CAD models with thickness information can be constructed.

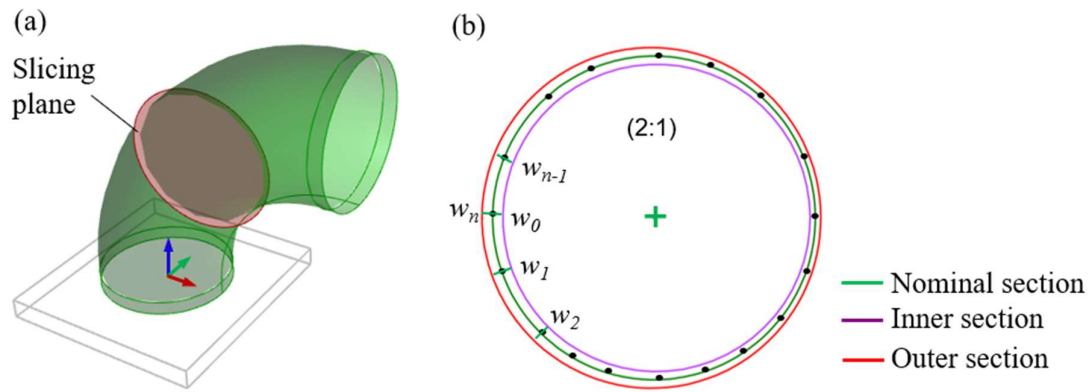


Fig. 64 The construction of inner and outer shells: (a) nominal CAD model; (b) a cross section between the slicing plane and the shell model

Fig. 64 shows a schematic the construction of a volume CAD model from a shell model. Each section of an irregular layer was obtained based on a 3D layer containing height information. The relative distance between the two adjacent layers was calculated and expressed as the weld bead height. The distance resolution between two control points was 2.0 mm. Further details will be described in section 6.3.3. Based on the height information, the bead width at each

control point was obtained from Eq. (6.2). Control points of inner and outer sections were computed by shifting the nominal control points to half of the predicted width. The point shifting operations occurred on the slicing plane with the direction set perpendicularly to the nominal section at each control point.

6.3.2.2. The correlation between the tube curvature and diameter

In the proposed approach, a metal part is deposited from a sequence of layers containing a thickness variation. The deviation of this variation depends on the degree of curvature. For example, a larger difference between the maximum and minimum thickness in a layer results in more curvature or a smaller diameter. With a bead height in the range of 1-2 mm [39], the curvature (R_{min}) and the diameter (d) are dependable. Fig. 65 shows a 3D slice from the bent tube. The achievable degree of curvature can be calculated as:

$$\begin{cases} \alpha = \frac{h_{min}}{R_1} \\ \alpha = \frac{h_{max}}{R_2} \end{cases} \quad (6.3)$$

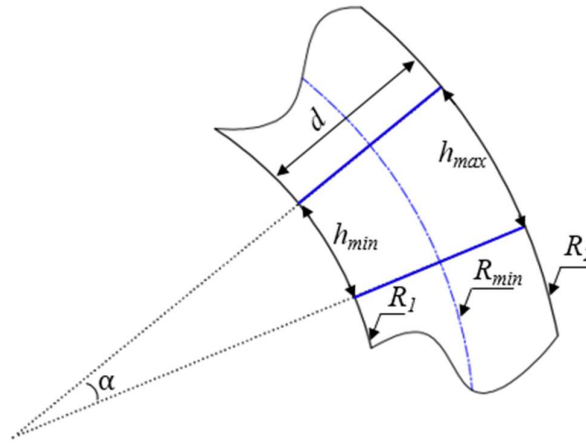


Fig. 65 Representation of a 3D slice on a bent tube

where h_{min} and h_{max} are the arc length, h_{min} and h_{max} are small segments of a curved line, so that they are supposed to be straight lines. R_1 and R_2 are the inner and outer radii, and α is the angle representing the curvature of the profile. Let denote $\lambda = h_{max}/h_{min}$. Since the height varies from 1-2 mm, λ is equal to 0.5. The limit curvature radius of the section can be obtained as follows:

$$R_{min} \geq 1.5d \quad (6.4)$$

6.3.3. Multi-axis programming of the welding robot

A tool path is defined by the control points which guide the welding torch to perform a specific motion. To do so, the tool path must transform into robot program. Fig. 66 indicates a flowchart that demonstrates the sequence from CAD to a metal part. This section presents the procedure of extracting points information and the composition of multi-axis programs for FANUC robot.

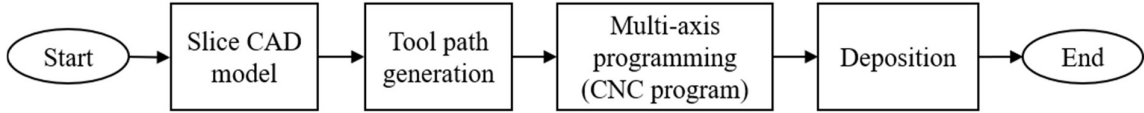


Fig. 66 Process procedure for a metal part

A multi-axis program for the robot system was needed with the aim of maintaining the neutral deposition position. The trajectory of the robot system was controlled through the information extracted from non-uniform thickness layers. Each layer was described by three attributes: control points defining the path, the normal vector of each point, and the relative distance to the previous cross section, as indicated in Fig. 67. When n control points were within a cross section, there were $n-1$ segments, and adjacent segments yielded a slight height variation. In other words, a 3D layer is a collection of individual segments with height variation. The deposition process manipulated the travel speed to achieve the design dimensions, which is reported in section 6.3.2.1. Each segment is short at only 2 mm, allowing for a continuous manufacturing process without breaks between adjacent segments.

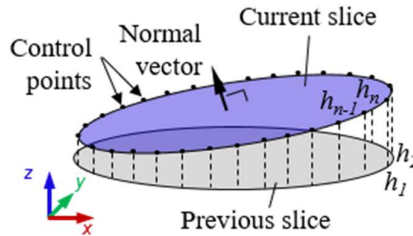


Fig. 67 Data acquisition from a 3D slice

Table 17 The raw data for robot program generation

Layer index	X	Y	Z	Roll	Pitch	Yaw	Height	Weld Enable
1	-5.0	0.0	0.0	1.0	0.0	0.0	2.00	TRUE
1	-4.8	-3.6	0.0	1.0	0.0	0.0	1.95	TRUE
...
n	-3.2	0.0	8.3	0.9	0.0	0.34	1.8	FALSE

Table 17 reports a data matrix for the robot program generation in the robot user frame. X , Y , and Z are coordinates of control points in the Cartesian coordinate system that define the coordinates of the tool center point (TCP). $Roll$, $Pitch$, and Yaw are Euler angles defined by the

orientation of the normal vector. *Height* constitutes the layer thickness of individual points. The last column is a Boolean variable, which describes the welding function. A script was developed in MATLAB to process the data from Table 17. Details can be seen in section 5.3. The outcomes of this script are ultimately the new coordinates of the TCP, the angles of the positioner (θ_x and θ_z), the orientation of the gun (A, B, C), and the desired travel speed (v_t),

6.4. Macrostructure and dimensional accuracy of the welded hollow sections

6.4.1. Bonding quality and waviness (destructive test)

This section presents a destructive test to investigate the quality of a welded structure. Fig. 68 illustrates a schematic of the three specimens that were extracted to examine the macrostructure, i.e., waviness, bonding quality, and defects. The specimens were grounded with grade P4000 sandpaper and polished 3.0 μm paste. Nitric acid with a 3% solution was applied on the polished surfaces for 40 sec. Macrographs were taken by means of a Leica DFC290 stereomicroscope and a DF C209 HD camera at a magnification of $\times 0.65$. The waviness (W_t) was calculated as the greatest difference of amplitudes, according to the DIN EN ISO 4287 standards.

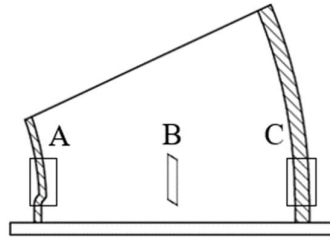


Fig. 68 A schematic of the CAD intersection with three extracted specimens

6.4.2. Geometric accuracy (non-destructive test)

6.4.2.1. Surface deviation between actual geometries and target geometries

Although CMT technology can reduce the thermal energy to the weld pool, metal parts still yield non-uniform thermal expansion and contraction. This leads to shrinkage and distortion in the bent hollow structures. To evaluate the accuracy of metal parts, the 3D scanner ATOS 5 from GOM GmbH was used to digitize the part surfaces in a scanning process that took place at room temperature (21°C). Metal parts were stored at ambient temperature for one day before being digitized. The digitized model and the CAD model were aligned, based on the origin of the CAD model. The surface deviation was evaluated in the GOM Inspect software. Besides the surface deviation, the deviation of the central axis and cross sections at three positions were also investigated. For instance, the central axis of the digitized model was obtained by applying the adaptive slicing algorithm that was reported in section 6.3.1. As presented in Fig. 69, the

slicing plane intersected with both models at three positions: the bottom, middle, and top, to get cross sections.

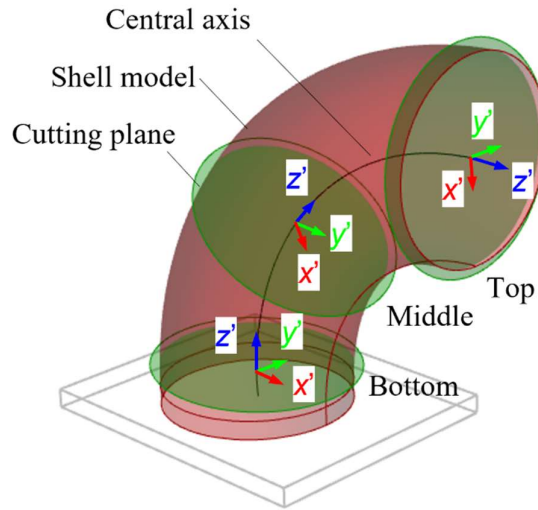


Fig. 69 A representation of three cutting planes at three positions

6.4.2.2. Ovality of welded hollow sections

With non-uniform thickness deposition, the cross-section profile of metal parts becomes an oval instead of a circle. The ovality is computed to find the conformity of the oval-shaped profile, which is deformed and distorted during solidification and cooling. This criterion was performed on geometries with circular cross sections at the top sections (Fig. 69). The TT-WN 010 standard for hollow bent tubes was used and the ovality is calculated via Eq. (6.5)

$$OV = \frac{200(d_{max} - d_{min})}{d_{max} + d_{min}} \quad (6.5)$$

OV is the percentage of ovality, and d_{max} and d_{min} are the maximum and minimum measured diameters, respectively. The accepted tolerance for the examined dimensions is 12.5% [189].

6.4.2.3. Reproducibility of metal parts

Due to the complexity of thermal expansion and contraction, metal parts might yield significant deviation. When this happens, it is not possible to design an offline correction for shrinkage and distortion. Examining reproducibility of this process makes the offline correction possible. To examine this condition, the reproducibility was investigated in part I from the test geometries with three metal parts produced using the same process parameters. The first part plays as a reference for the others. Three points on the central axis were selected to evaluate reproducibility. The positions of these three points are reported in Fig. 69.

6.5. Off-line compensation approach for material shrinkage and distortion

6.5.1. The evolution of part geometry

This section focuses on an experiment that had been implemented to gain insight into the evolution of temperature distribution and the geometry of a part during processing. An infrared camera from InfraTec GmbH with a resolution of 1024×768 was applied to capture the thermal gradient. Fig. 70 illustrates the experimental setup. The workpiece was captured from the side view on the y-z plane. A scale unit was established in order to obtain images at actual dimensions without image distortion. A plate was placed at the middle of the substrate and was used as a reference frame for the image correction. This reference plate was removed before starting the deposition process. The camera position and the positioner were left unchanged when taking the thermal gradient. The part was split into six subparts; after finishing each subpart, the positioner was returned to its original position, and a temperature gradient was captured. The idle time was about 2 minutes between subparts.

Based on the existing work from the Ref. [190], a MATLAB script was developed to correct the image distortion and detect the edges of the metal part. Four corners of the reference plate were selected as the reference points to establish a transformation matrix. Since the dimensions of the plate were identified as 248×248 mm, the outer contour of the part could be represented to actual scale.

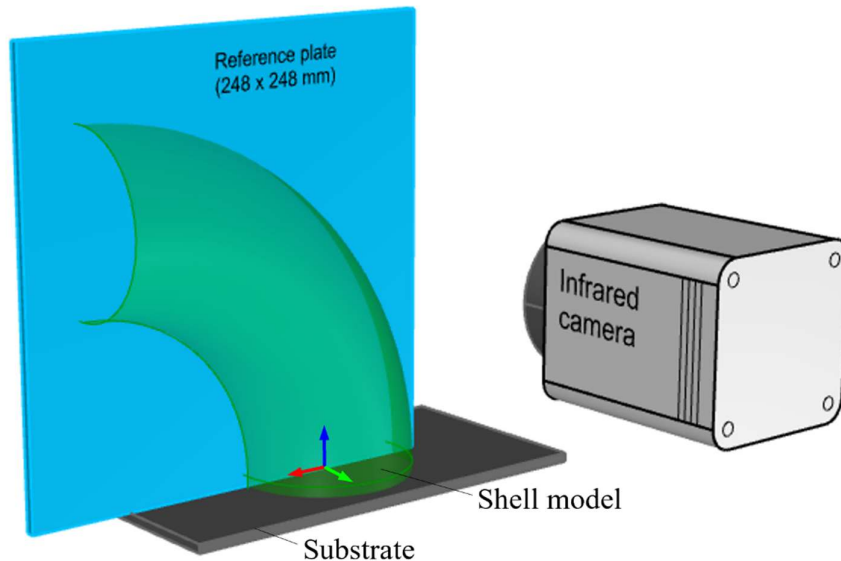


Fig. 70 A schematic of the infrared camera set-up with a reference plate

6.5.2. Compensation strategy

This section presents an experimental method to compensate for the shrinkage and distortion of deposited parts. The main idea is that the residual stresses form a bending moment, which jeopardizes the actual central axis. It is assumed that the right actual central axis can be obtained by applying a virtual bending moment to the original CAD geometry. It is challenging that the bending moment is unknown in advance. To determine this moment, the geometry after deposition with shrinkage and deformation data should be available, which can be achieved by a numerical method or an experimental method. The performance of the finite element model is not effective [191]. Thereby, it would be faster and more accurate with the experimental method. In this work, the tool path for the metal part is generated based on the original CAD model. After being deposited, the metal part is digitized. The virtual bending moment can be obtained, and an inverse bending moment is applied to the CAD model, as shown in Fig. 71. Differing from the casting process, the WAAM process deposits each layer, and the deformation of each deposited layer has an implication on the global deformation and distortion. Thereby, the approach is that the correction strategy is applied on each layer locally.

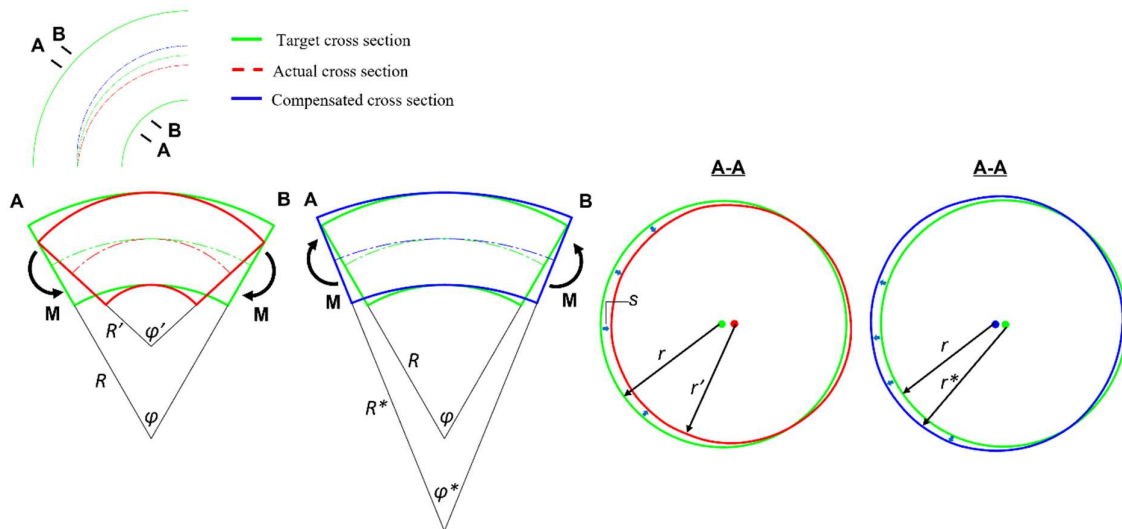


Fig. 71 Representation of distortion caused by the virtual bending moment

During the welding process, the bending moment changes along the part, which distorts the central axis locally, for instance, the curvature radius varies from R to R' . Thereby, the local correction is implemented on the way that bending the central axis to the opposite direction, which creates a new curvature radius (R^*). To realize this approach, each layer is shifted to the new curvature radius and a cross section, which has the nominal radius r , denoted as a layer in the tool path planning process. After the deposition process, the cross section is shrunk to a

smaller radius than the nominal one ($r' < r$). For each reference point (i), the actual profile is obtained, which has $r_i = r_i' + \vec{S}_i$, where \vec{S}_i is the deviation information measured at i . The distance between two reference points is 2 mm. For the correction strategy, a new cross section is computed when the deviation data is taken into account. In particular, the new profile is calculated in the way that $r_i^* = r_i - \vec{S}_i$.

The proposed approach might need to iterate until converging to the target geometry. For instance, the iteration of constructing a metal part, digitizing the surface, and tool path correction is repeated until the actual geometry meets the tolerance requirements. The critical points here are that whether the proposed algorithm is feasible and how fast it converges. To answer this research question, part I, which owns the thickest layer thickness, plays as termination condition. For instance, whenever the surface deviation is within the maximum waviness, the correction method converges, and no further iteration is implemented.

6.6. Experimental results of tool path generation for curved thin-walled structures

6.6.1. Relationship between weld bead geometry and travel speed, and computed CAD model

Fig. 72 shows a typical wall welded with a travel speed of 500 mm/min. Weld bead geometries with varying travel speeds are reported in Table 18. The value is the average of three positions. When the welding torch moves too slowly, e.g., 100 mm/min, the straight wall yields a wavy shape. On the other hand, higher travel speeds of around 950 mm/min or faster create humps thereby restricting the deposition process. Therefore, valid travel speeds range from 150 to 900 mm/min.

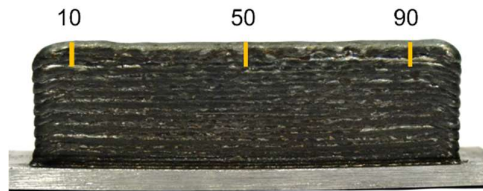


Fig. 72 A deposited wall with the travel speed of 500 mm/min

Fig. 73 illustrates the data points of the weld bead height and travel speed. A reciprocal function exists between the quantities of the weld bead height and width.

The curve of the dashed line goes through almost all data points and the goodness-of-fit $R^2 = 0.9923$. The travel speed is computed as a function of the desired weld bead height below:

$$v_t = 686.4\bar{h}^{-2.069} \text{ mm/min}; \bar{h} \in [1.0, 2.0] \quad (6.6)$$

The equation representing weld bead width as a function of bead height is expressed via Eq. (6.7). The R^2 -value of the interpolation is equal to 0.9886.

$$w = 1.5093\bar{h}^4 - 8.8702\bar{h}^3 + 18.132\bar{h}^2 - 11.823\bar{h} + 4.3077; \bar{h} \in [1.0, 2.0] \quad (6.7)$$

\bar{h} is a dimensionless parameter and $\bar{h} = h/h^*$, $h \in [1.0, 2.0]$ mm and $h^* = 1$ mm.

With the computed weld bead width, the inner and outer surface of the bent hollow structure can be constructed, as illustrated in Fig. 74.

Based on the experimental results, the relationship between the travel speed and the weld bead geometry is established. The data can be collected with the effort of a mere half day's work. With different process parameters (e.g., material, wire-feed rate, and shielding gas), can denote a different relationship between the travel speed and the weld bead geometry, requiring the experiments be repeated. The range of weldable bead height is limited, helping establish a design rule that shows a feasible curvature to the diameter.

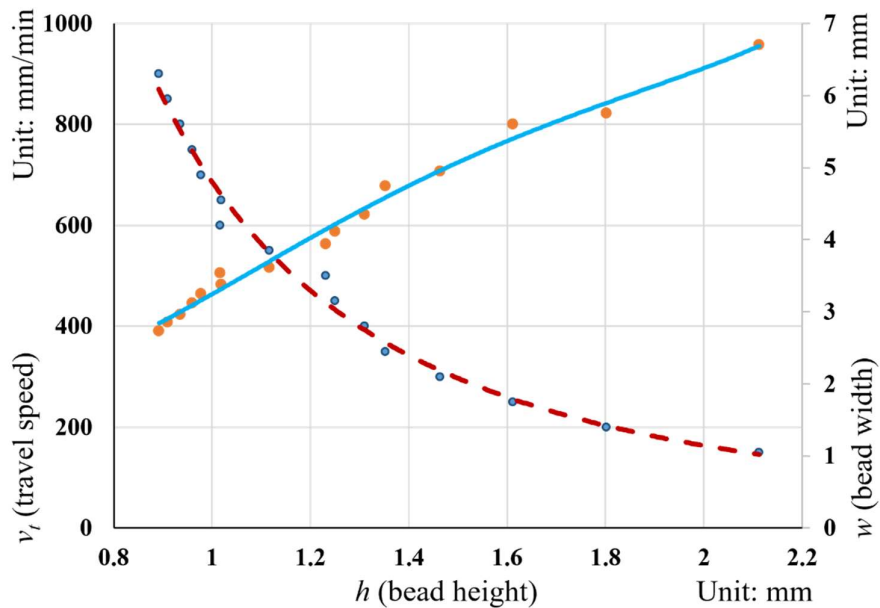


Fig. 73 A scatter chart and interpolation function between travel speed and bead height (dash line) and between bead width and bead height (continuous line)

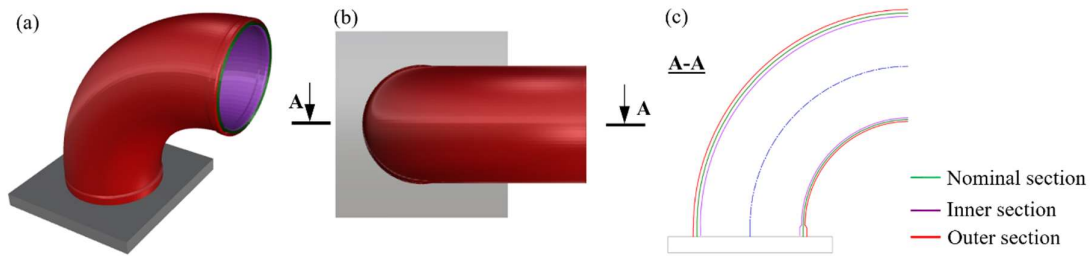


Fig. 74 Construction of a CAD model: (a) computed CAD model with inner and outer shells; (b) top view of the computed CAD model; (c) intersection of the cutting plane (A-A) and the computed CAD model

Table 18 Average height and width of a weld bead

No.	Control input	Corresponding weld bead	
	v_t (mm/min)	h (mm)	W (mm)
1	100	2.723	8.001
2	150	2.102	6.673
3	200	1.792	5.723
4	250	1.601	5.573
5	300	1.454	4.923
6	300	1.342	4.717
7	400	1.300	4.320
8	450	1.240	4.087
9	500	1.221	3.910
10	550	1.106	3.587
11	600	1.006	3.507
12	650	1.008	3.350
13	700	0.967	3.220
14	750	0.950	3.093
15	800	0.926	2.933
16	850	0.900	2.830
17	900	0.882	2.707
18	950	--	--
19	1000	--	--

6.6.2. Tool path generation and deposition performance

Fig. 75 indicates the WAAM deposition process for part I. The positioner initially starts in a horizontal position. After each layer, the positioner is gradually manipulated to maintain the neutral deposition position.

Fig. 76 and Fig. 77 compare tool paths and metal parts for discontinuous and continuous deposition strategies in part I. There are 170 cross sections in the discontinuous tool path, which act as basic tool path for each layer. The idle time between layers was about 3.0 seconds for the movement of the positioner. The metal part yielded imperfections at layer endpoints due to the

uneven weld bead phenomenon. Moreover, slag could occur on the solidified weld pool, creating an isolation layer for the electric arc in the next weld beads. The welding process was interrupted, calling for human intervention. The processing time was about 128 minutes without mean time between failures.

Contrarily, the continuous tool path yielded only one weld pass for the entire manufacturing process. This strategy avoided uneven weld beads. The positioner and the robot arm coordinated simultaneously during the process. The processing time decreased by 8.5 minutes, as compared with the other tool path. More benefits were also revealed, such as better surface quality, higher reliability, and a reduction of processing time.

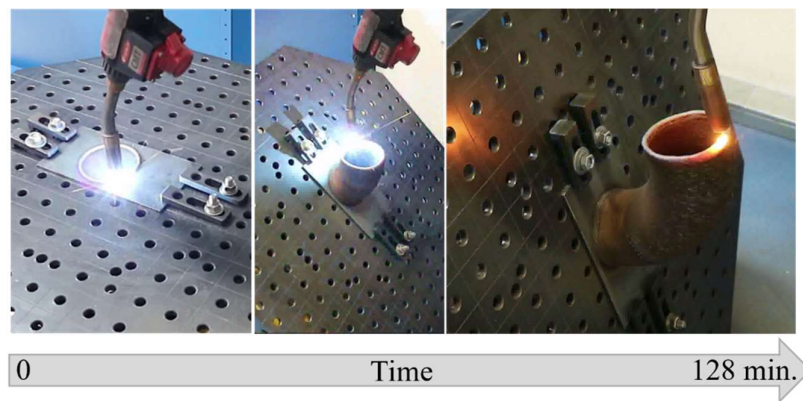


Fig. 75 A deposition process with WAAM

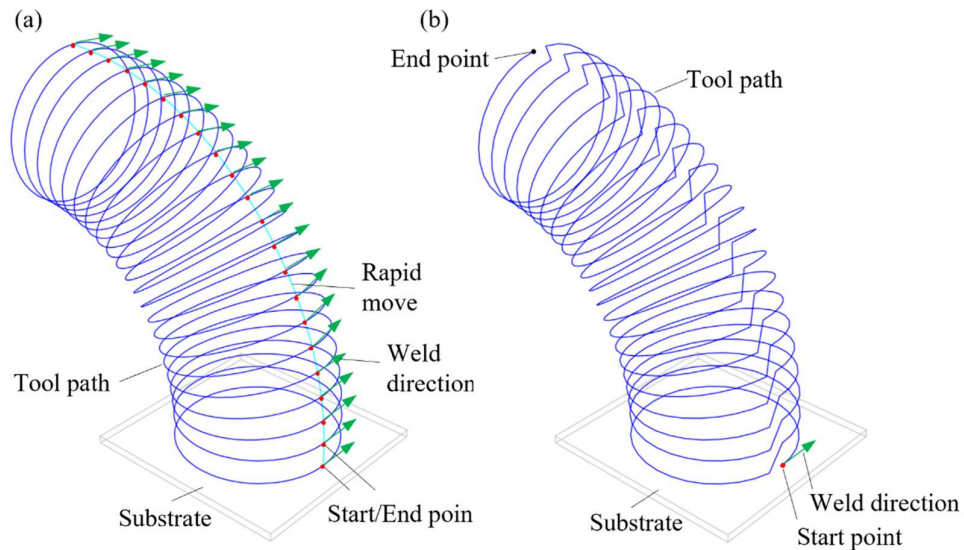


Fig. 76 An illustration of the tool paths: (a) discontinuous; (b) continuous spiral path

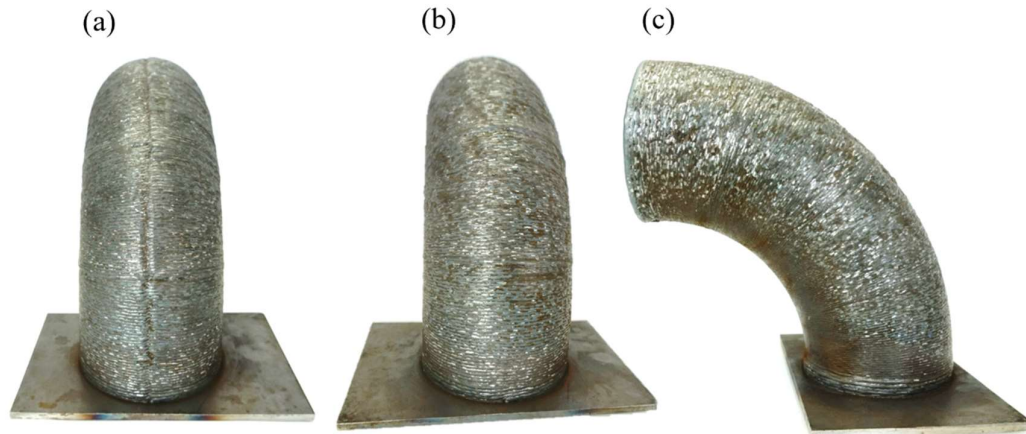


Fig. 77 Comparison of metal parts from two tool path strategies in part I: (a) discontinuous; (b) continuous; (c) side view



Fig. 78 Tool path and metal part. Only every fifth layer is displayed

The four test geometries, their tool paths and corresponding metal parts are illustrated in Fig. 78. For the sake of better visualization, the number of cross sections is decreased so that only every fifth layer is depicted. All metal parts are deposited properly without any interruptions or failure by following a continuous tool path strategy.

6.6.3. Evaluation of the macrostructure and dimensional accuracy of welded hollow sections

6.6.3.1. Macrographs and the waviness of curved thin-walled structures

The macrographs are illustrated in Fig. 79, where one can see that the macrographs reveal no defects nor any other imperfections such as cracks, humps, or uneven weld beads. A significant difference regarding the geometrical dimensions can be seen. For instance, the width and height of one layer rises from about 1.0 mm to 1.8 mm in specimen A, and from around 3.2 mm to 6.0 mm in specimen C. Proper fusion bonding between adjacent layers can generally be observed in all specimens along with a surface waviness of about 0.1 to 0.3 mm.

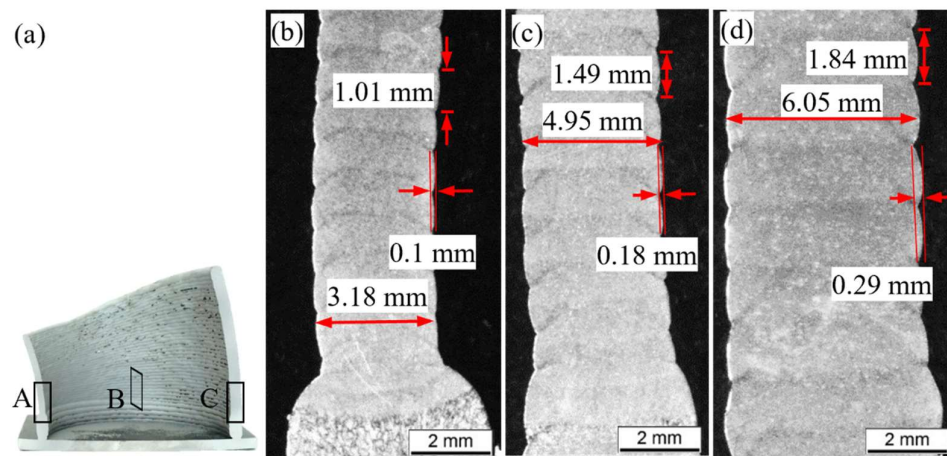


Fig. 79 The macrostructure of the metal part: (a) intersection (grey due to sand blasting); (b) specimen A; (c) specimen B; (d) specimen C

To verify the Eq. (6.7), which presents the relationship of bead height and bead width, the deviation between the measured and predicted bead width is reported in Table 19. It confirms that the deviation error is less than 3.4%.

Fig. 80 illustrates the schematic used to measure the waviness along the actual intersection profile (green curve) of part I. As can be seen, the waviness fluctuates, and limits to 1.22 mm.

Table 19 Validation results for the relationship of bead height and bead width

Measured bead height (mm)	Measured bead width (mm)	Predicted bead width (mm)	Error (%)
1.01	3.18	3.29	3.4
1.49	4.95	5.04	1.8
1.84	6.05	5.98	1.2

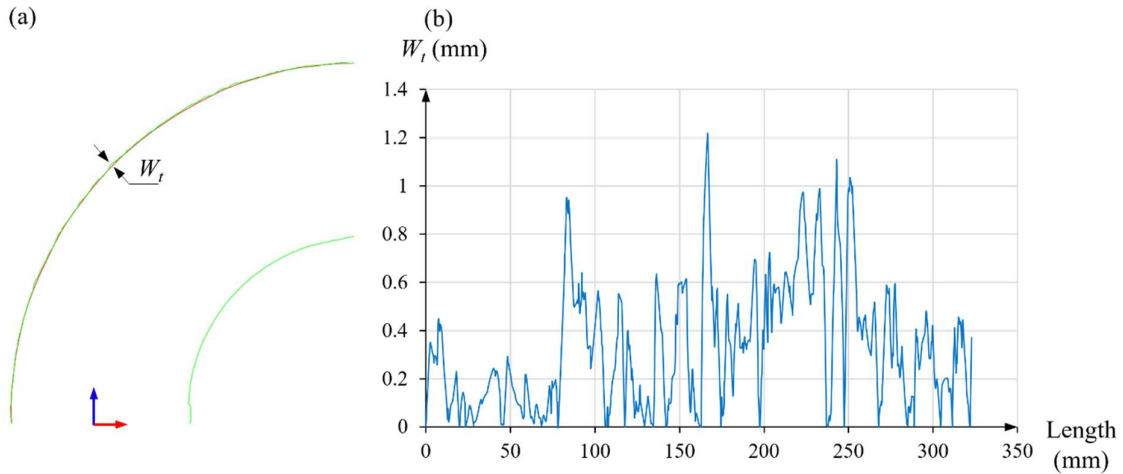


Fig. 80 Waviness along actual profile

6.6.3.2. Geometric accuracy between actual geometries and target geometries

6.6.3.2.1. Surface deviation between actual geometries and target geometries

The alignment of the CAD and the digitized models are illustrated in Fig. 81. Only outer surfaces could be captured and analyzed due to the measurement principle. The outer surfaces were constructed from shell models using the procedure reported above.

Fig. 88 reports the surface deviation between the computed CAD model and the actual part. In general, all metal parts yield deformation and distortion, a problem far more significant in larger parts. The surface deviation ranges from about -6.0 to +3.3 mm for part I, from -4.0 to +1.2 mm for part II, from -7.0 to +9.0 mm for part III, and from -6.0 to +3.0 mm for part IV. From the origin, the deviation is minor, and becomes larger towards the growth direction.

The equation representing travel speed as a function of bead height already includes shrinkage information and noise when the data is measured at room temperature. Therefore, the metal hollow structures do not assume to yield any deformation and distortion since printed parts compensate for the material shrinkage. However, the metal parts reveal a great difference to the target geometry. This means that the shrinkage rate depends on the heat transfer coefficient, which relates to the surrounding environment, shape, and geometry of a part. Straight walls cannot represent the thermal behavior of bent hollow structures.

Each deposited layer was performed on a hot surface along with its preceding layers, which were also not at room temperature. Due to the accumulated heat input, areas close to the current layer yielded higher temperatures. The current layer was placed on an inaccurate position when existing layers were later being shrunken. During cooling, the former layers pulled the later

ones, leading to a domino-like distortion effect. Therefore, metal parts yielded more deviation along the built direction.

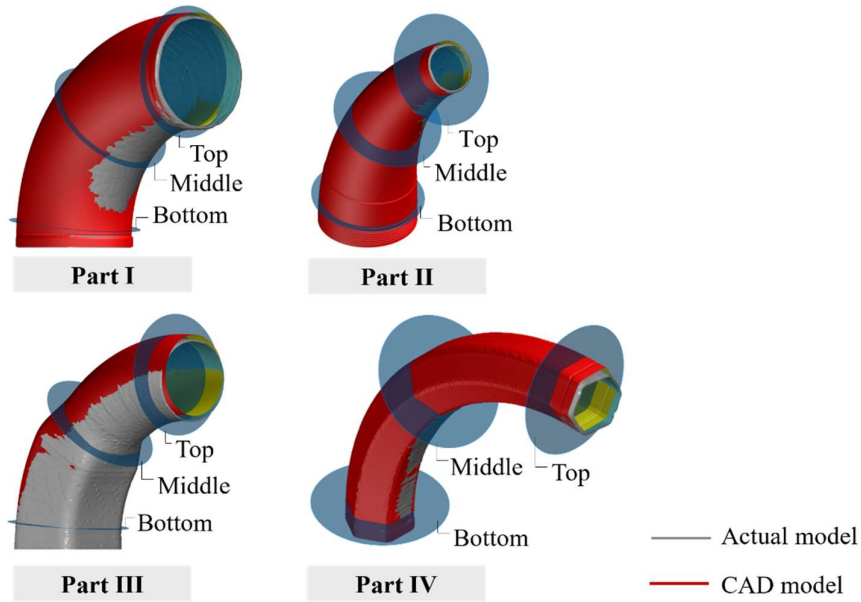


Fig. 81 The alignment of the computed CAD models and actual parts

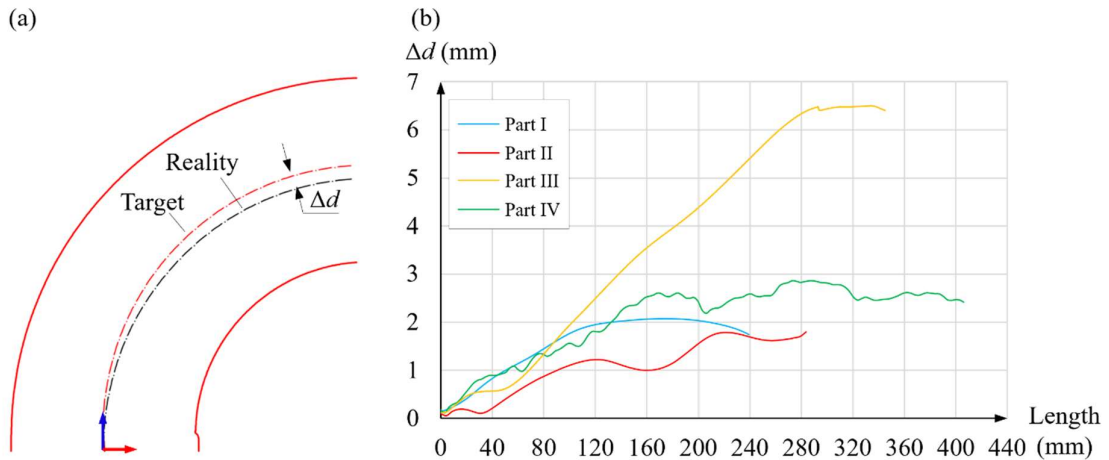


Fig. 82 A schematic of the target and actual central axis (a) and deviation along the central axis (b)

Moreover, thicker areas yielded greater deviations. Since the welding torch moved slowly to deposit more volume, the thicker portions received more thermal energy than the thinner ones. The rounded-rectangle section and hexagon had different levels of thermal expansion and material contraction. Therefore, part III, which is a combination of both a rounded-rectangle and a circular cross section, reveals the most significant distortion by about 9.0 mm. Parts that have a circular cross section experienced less deformation and distortion than the other

geometries in the experiment. From the central axis, the distortion occurs mainly in the x-z plane.

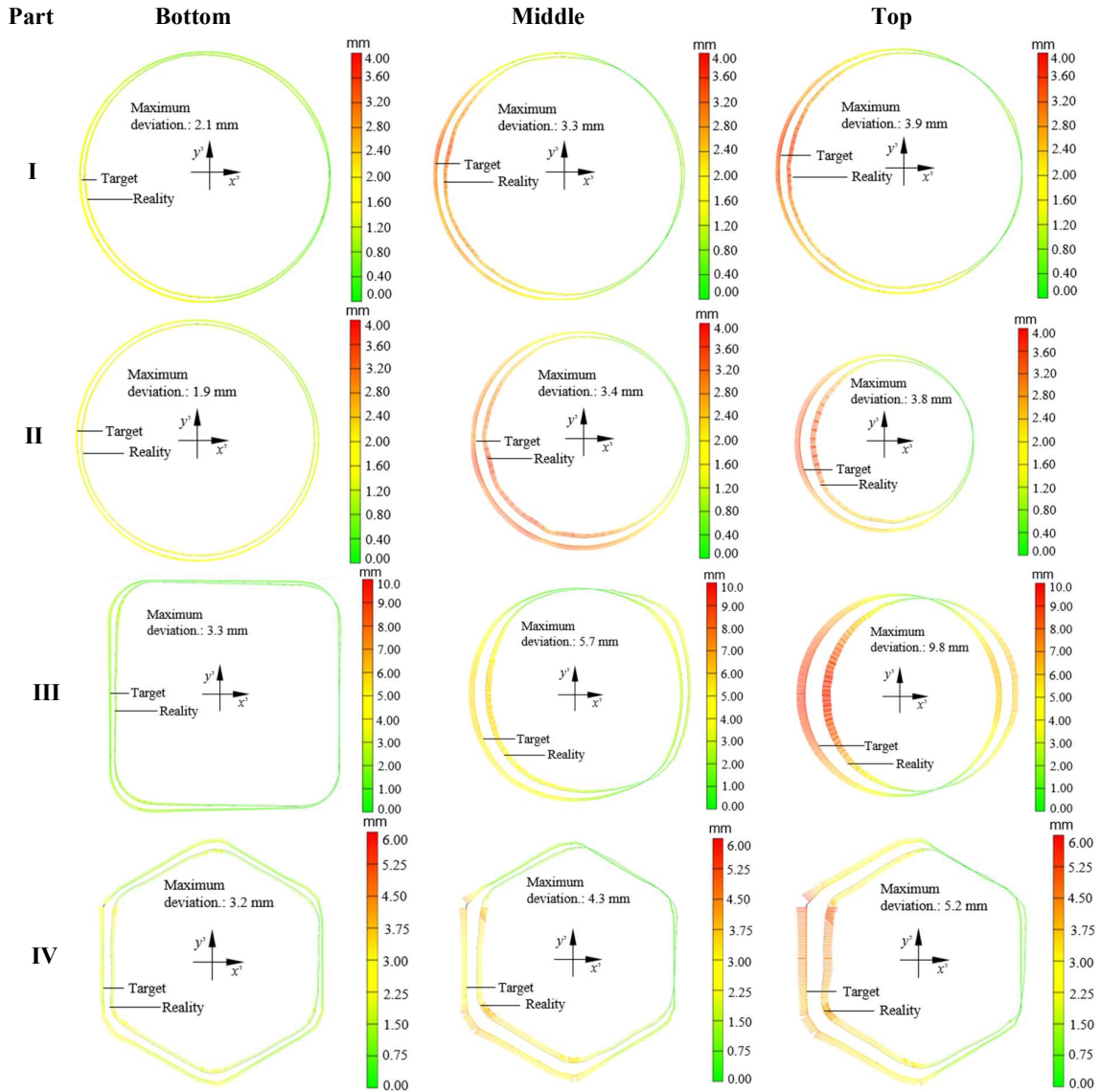


Fig. 83 Cross-section deviation between the computed CAD model and the actual part at three intersections

Fig. 82 indicates the deviation of the actual central axis to the target. For parts I, II, and IV, the deviation is below 3 mm while part III experiences a much greater value (about 6.6 mm). The deviations tend to increase along the growth direction until they reached the maximum. Cross-section deviations tend to rise along the build direction, as can be seen in Fig. 83. Within a cross section, thicker portions (left-hand side) yield more deviation than thinner ones (right-hand side).

6.6.3.2.2. Ovality of welded hollow sections

The ovality is reported in Table 20. This criterion cannot be applied for the part with a hexagonal cross section. As can be seen, the ovality is much lower than the set allowance of 12.5%. Therefore, the metal parts are acceptable only in terms of ovality.

Table 20 The ovality of welded hollow sections

Part	Measurement		Calculation
	d_{max} (mm)	d_{min} (mm)	OV (%)
I	103.33	101.682	1.6
II	53.792	52.513	2.4
III	102.71	100.93	1.75
IV	--	--	--

6.6.3.2.3. Reproducibility of metal parts

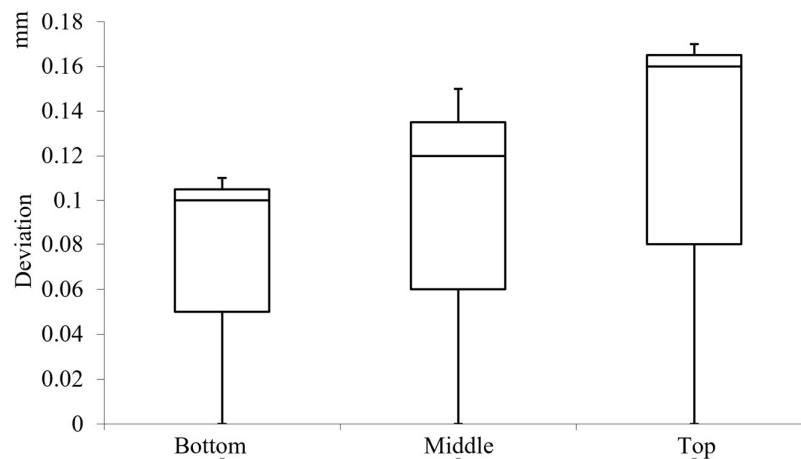


Fig. 84 A box plot for the repeatability at three positions on the central axis

Fig. 84 shows the plot for reproducibility at three positions. As reported in section 6.6.3.2.1, the WAAM process yielded inaccurate geometry due to distortions and waviness, but proved to have good repeatability when the deviation limited to 0.2 mm. Therefore, the production of bent hollow structures is stable, as with the same process conditions though the variance of the obtained geometry is smaller than the waviness. It is worth implementing a compensation strategy for inaccurate geometries, based on experimental results.

6.6.4. Compensation of shrinkage and distortion for curved thin-walled structures

6.6.4.1.1. Evolution of part geometry during welding

The temperature gradient for six stages during welding is presented in Fig. 85. Using thermal imaging, evolution of part's outer geometry can be observed in-situ. Since a great deal of thermal energy conducts to the substrate, the first subpart (segment 1) shows a small thermal

gradient. The thicker regions yielded higher temperatures due to the larger thermal mass. The temperature distribution in existing segments tended to be homogenous, while the thermal gradients took place in the last segment.

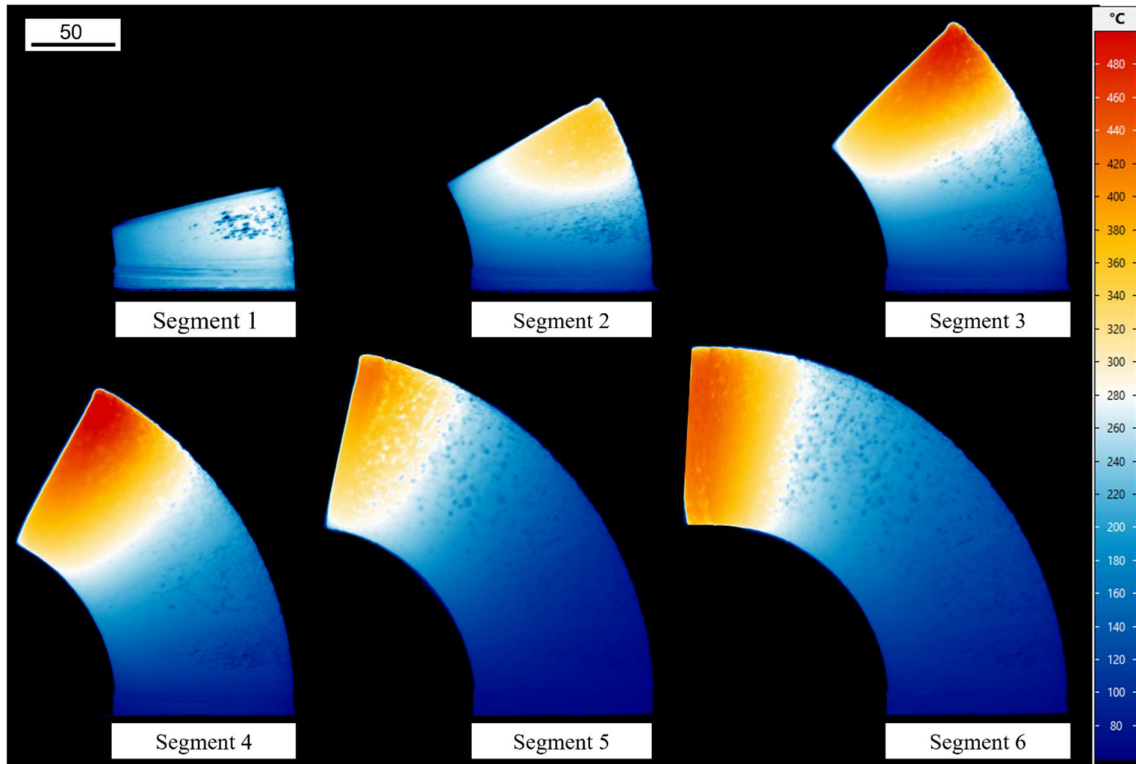


Fig. 85 Thermal gradient during processing

Fig. 86 illustrates the profile extracted after the metal is deposited and cooled down to room temperature, along with the central axis for these two states. The last deposited segment, which has a significant thermal gradient, deformed upon cooling. The deviation yielded significantly at the past segment when the temperature dropped from about 430°C to room temperature, to about 5.5 mm.

Fig. 87 shows the deviation variation of the central axis through six points after depositing each subpart. The deviation was computed between room temperature and high temperatures. There is only one subpart (segment 1) at stage 1, which means there was only one reference point at this stage (P_1). The deviation was calculated based on the position of P_1 at room temperature and high temperatures. In the next stage, two subparts were deposited, and the deviation computed at point P_2 as well as at the previous reference point. The procedure continued until the metal part was completed. As can be seen, the position of the reference points changed during the process, yielding an upward trend.

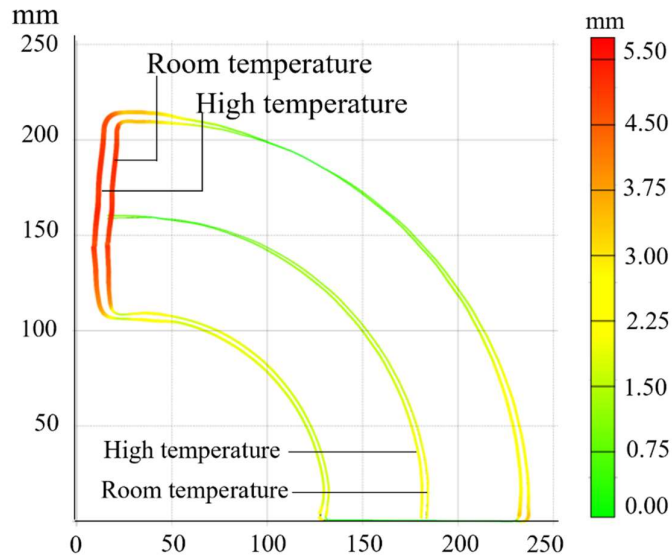


Fig. 86 Profile deviation between room temperature and high temperatures

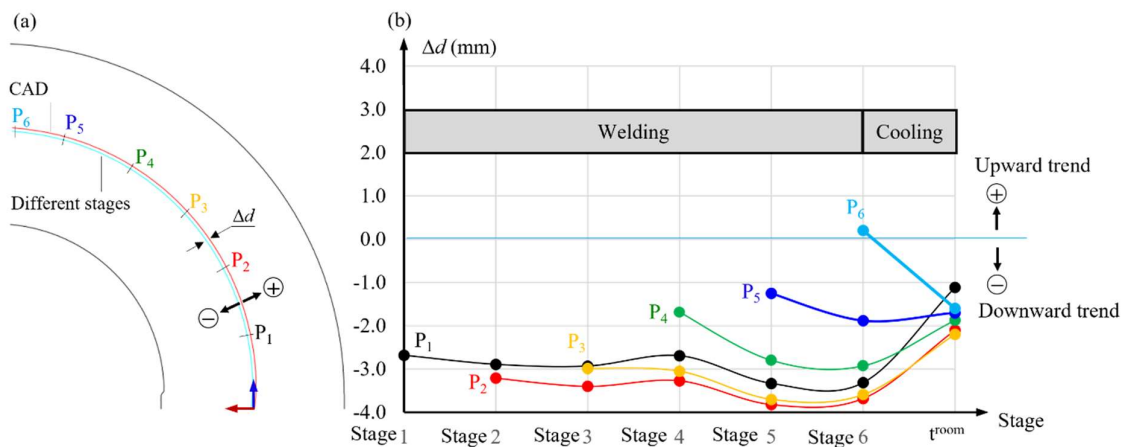


Fig. 87 A schematic of the central axis with 6 reference points (a) and deviation during the process (b)

6.6.4.1.2. Compensation strategy

Fig. 88 compares the surface deviation of geometries manufactured with and without a geometric correction. Without applying a compensation strategy, the deviations are significant in all four test cases. These inaccurate parts are used as the input data for the improvement of the tool path. In the first iteration of the compensation algorithm, all four parts reveal a much lower deviation than in the previous ones. The maximum value is less than 1.2 mm, which is smaller than the termination condition of 1.22 mm. Therefore, the correction process terminated after the first iteration.

Fig. 89 illustrates the deviation of the four parts from the central axis with and without a correction strategy. The deviation dropped significantly, in fact below 1.1 mm, for all test geometries.

The cross-section deviation of the CAD model and the actual geometry is illustrated in Fig. 90. By applying the correction algorithm, the actual cross sections ended up being close to the targets for all geometries with a maximum deviation of 1.2 mm, which is slightly lower than the tolerance of 1.22 mm.

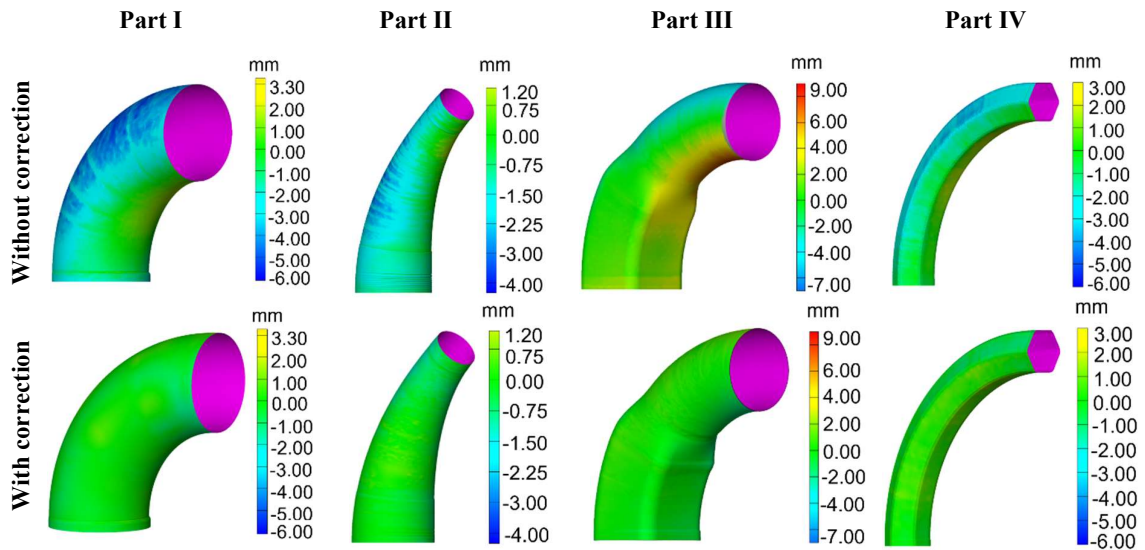


Fig. 88 A comparison of surface deviation of two strategies

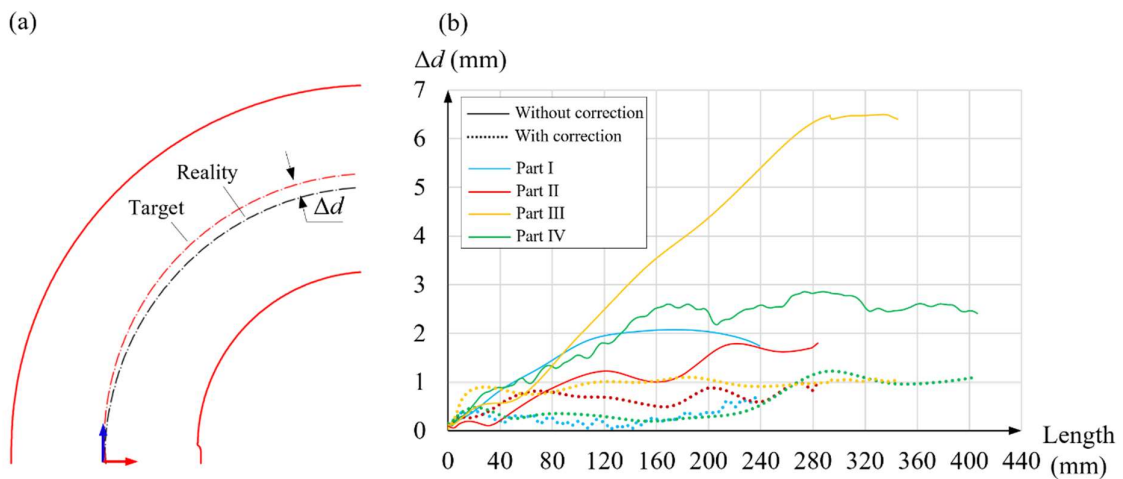


Fig. 89 A schematic of the target and actual central axis (a) and deviation between the actual and the target along the central axis (b)

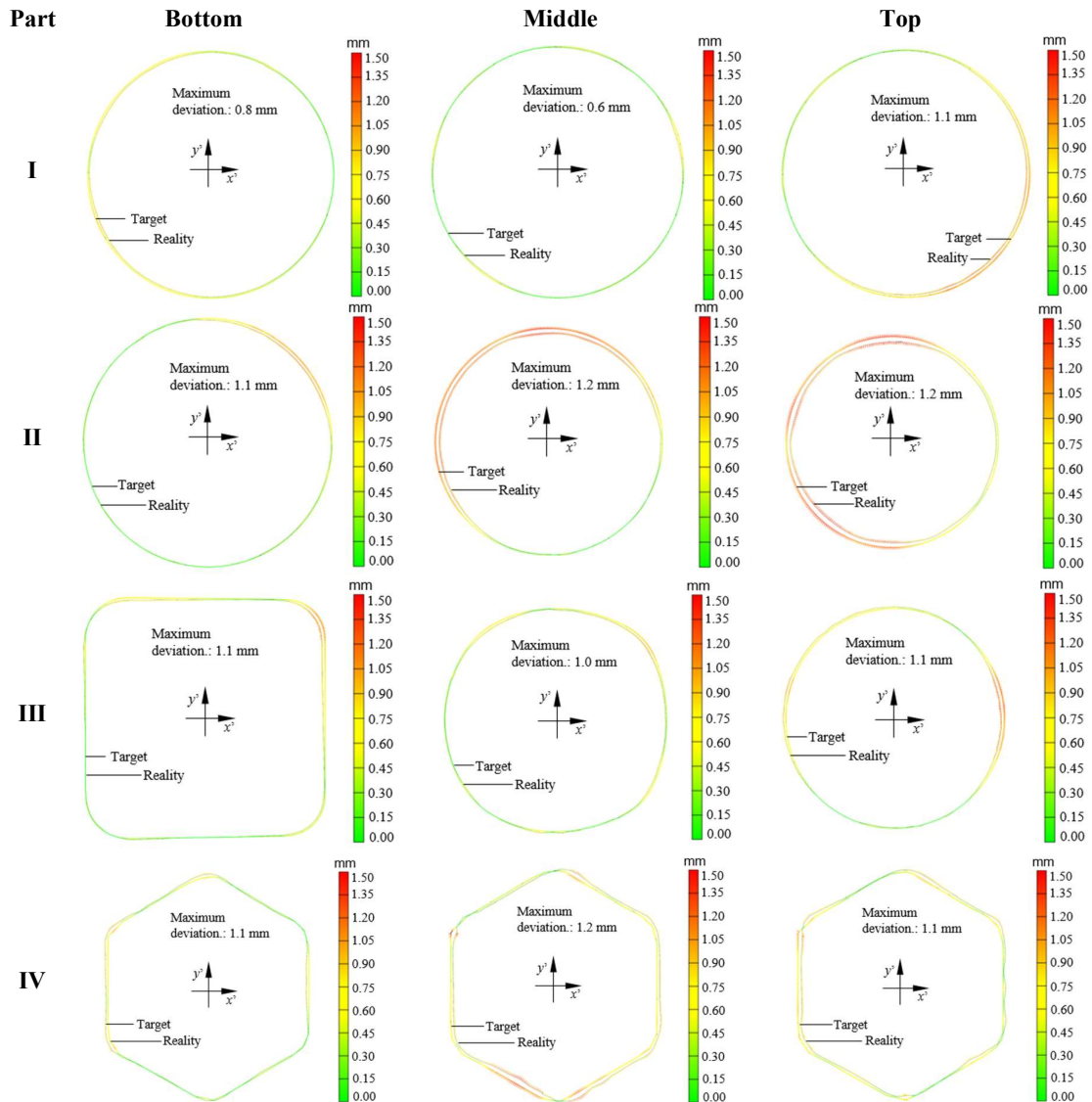


Fig. 90 An intersectional comparison of the three positions for actual and target geometry with the correction strategy

6.7. Discussion of the developed tool path generation and the compensation strategy

6.7.1. Discussion of the continuous deposition strategy and variable wall thickness

Although the multi-axis deposition strategy has been proposed in the past [114, 116, 118], none of the previous strategies can produce curved thin-walled hollow structures. In general, overhanging parts are achieved by welding straight printed profiles on an existing part. The proposed algorithm adopts different approaches to the problem. A combination of weld bead geometry control and a multi-axis deposition strategy realizes non-uniform thickness layers. Consequently, curved thin-walled hollow structures can be manufactured by WAAM process.

Unlike the existing method [111], complex functional profiles can be produced without milling operations.

Another method of constructing curved thin-walled hollow structures is to weld “incomplete” layers to make the desired curvature, as presented in Fig. 91. This strategy uses unchanged process parameters to generate a constant weld bead geometry. As it is not restricted by height variation, this approach also allows for a larger variety of section curvatures and can be applied to laser powder deposition processes wherein the layer thickness is relatively thin (0.2-1.0 mm) [192]. However, this method is inapplicable in WAAM processes due to its low geometrical resolution (1-2 mm) as well as its ‘open’ weld beads that result in a staircase effect, which may restrict the deposition of subsequent layers.

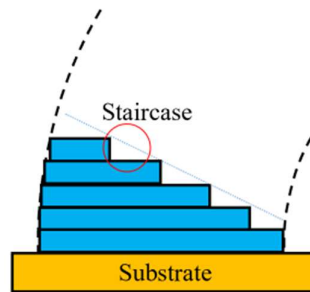


Fig. 91 Incomplete layer deposition

For fluid transportation applications, rough surfaces can make the WAAM process impracticable. This issue can be resolved by a hybrid method in which milling operations are performed in-situ after depositing a few layers.

6.7.2. Discussion of the compensation strategy

The compensation strategy contains two aspects: the compensation of shrinkage due to material contraction and the distortion of the profile due to residual stresses. Supposing that thermal distribution is uniform, all deposited areas hold a specific temperature. The compensation of shrinkage could be achieved based on the coefficient of expansion. However, a thermal gradient is also created. The former layers yielded a low temperature while the current layer yielded a much higher temperature than its surrounding areas. Thicker portions would therefore produce more heat energy than thinner portions within a layer, making the estimation and compensation of the shrinkage amount unrealistic. Distortion of the central axis is similarly difficult to calculate. Several finite element models of the WAAM process were put forward, including heat source modeling, material deposition modeling and material properties [193, 194]. Numerical models were constructed to predict thermal distribution during the manufacturing

process while considering heat loss through radiation, conduction, and convection. The material shrinkage, deformation and residual stresses could be estimated, and a compensated geometry could be performed. However, the simulation approach reveals many drawbacks. The set-up and execution of a simulation model is time-consuming and so existing studies proposed numerical models just for simplified shapes and geometries. Consequently, it is difficult to realize the predictions of shrinkage and distortion for complex parts.

This chapter presents a method to compensate for both for shrinkage and distortion from experimental information. Firstly, a metal part is manufactured to obtain geometric errors, a process that takes around 2-3 hours for the parts considered in this work, considerably less time than the computation time of a finite element simulation. Geometric accuracy is ensured with a single iteration. The deviation of the actual and target cross sections of the metal part can be used to estimate cross sections, which tend to shrink to the desired size. Many improvements can be achieved in future research. Shapes should be manufactured that might yield a larger distortion so as to test the convergence of the proposed algorithm method. The compensation process probably needs more than one iteration. Simulation methods would be an interesting approach to estimate a compensation without scarifying a metal part.

6.8. Summary of chapter findings

A new tool path generation tool has been developed in Rhinoceros/Grasshopper and MATLAB to produce curved thin-walled hollow structures by means of wire-arc additive manufacturing processes. Some main points can be drawn below:

- Curved hollow structures can be produced by using a multi-axis deposition with non-uniform thickness layers.
- Non-uniform thickness layers can be realized by manipulating the travel speed to obtain a desired weld bead height.
- The minimum curvature radius of the structure corresponds to 1.5 times the diameter of the cross section. This corresponds exactly to long-radius pipes, which is common in piping.
- A neutral welding position should be maintained to reduce the noises of gravity, which requires the use of a positioner.
- The WAAM process for complex geometries is repeatable and can be applied to a compensation strategy for shrinkage and distortion.
- Shrinkage can be compensated for by adjusting the cross sections, based on the measured deviation between the metal part and the CAD geometry. Experimental data has showed

that the proposed correction can correct the geometric deviations, which are below the waviness of the surface.

7. Summary of the main findings and possibilities for future research

This work presented tool path strategies for metal parts produced by a wire-arc additive manufacturing process. These strategies were based on the current state, development trend, and potential of WAAM. This monograph includes models for multi-bead deposition, a tool path strategy for rib-web lightweight structures, a multi-axis deposition strategy, and the application of the multi-axis deposition for the construction of curved thin-walled hollow structures. The main findings and outlook for each section are presented below.

❖ Multi-bead overlapping models

For large metal parts, weld beads are welded next to each other, and the cross-section profile of a single weld bead is presented as a parabolic shape. It is therefore vital that the optimal distance among adjacent beads is determined, so that deposition surfaces are relatively even. Existing overlapping models [43, 45] have not addressed the problem of uneven deposition surfaces. The build rate in the outer contour of the part may lag the build rate within the interior. In other words, inner beads overlapped with two neighboring beads at a higher overlapping rate than those at the part's edge where the deposited beads have only a one-sided overlap. Other groups of researchers realized this problem and intuitively added an extra bead in every two layers.

This study came up with a systematic approach when balancing overlapping and empty volumes to determine the optimal distances between adjacent weld beads. Mathematical models for multi-bead overlapping in boundaries have been developed to compute the overlapping rates. The results show that distances can be computed from the weld bead width. For example, zigzag and contour patterns have the optimal overlapping distance of nearly half the bead width, and the overlapping distance for zigzag patterns is half the bead width. The developed models are tested on mild steel and perform convincing results. For statistical insights, more materials and process parameters should be investigated in the future.

❖ Fabrication of lightweight structures

Due to the superior features of WAAM, such as a high deposition rate, large working volume, low buy-to-fly ratio, and no tooling costs, the WAAM process is well-fit for the fabrication of the lightweight structures, such as rib-web structures. High-performance parts can be manufactured by adding materials layer-by-layer instead of by forging or subtractive machining, which yield high tooling costs, buy-to-fly ratios, and material waste.

This study also addressed a tool path strategy for rib-web lightweight structures. The procedure of generating the tool path is based on two weld beads. More weld beads can be added for

applications requiring a thicker wall. Contour patterns are suitable for the construction of rib-web structures and cross sections are offset to ensure the optimal overlapping length between two adjacent weld beads. To avoid the uneven weld bead phenomenon, the number of weld passes should ideally be minimized to one. The welding torch turns on and off for transition lines between contours, increasing the danger of uneven weld beads. This work suggests a Eulerian path approach, allowing a continuous tool motion for any arbitrary geometry. The electric arc is on during the position process until the metal part is complete. Thus, the problem of uneven weld beads can be avoided, and the movement efficiency maximized. In addition to that, the continuous motion prevents machine errors from slags and surface contamination. The proposed algorithm yields a deposition rate of over 3.0 kg/h for the selected welding parameters and WAAM can be a replacement for conventional manufacturing processes.

Although the contour patterns can improve the accuracy of metal parts and mitigate the warpage problem, these patterns yield voids in junctions. This kind of defect is susceptible for the mechanical performance of metal parts. Therefore, the geometrical correction strategy was proposed in order to properly deposit the amount of material required for the junction. For instance, the turning points are modified to increase the deposition rate. Due to the complex dependence of material behavior on junction geometry, material, and process parameters, the geometrical model is not applicable to avoid voids. The optimal path correction would be to weld the given junction once with the geometrical correction, evaluating the void length, and updating the correction factor.

Optimization should draw upon this correction strategy in the production of scale, when the batch size production is sufficient. However, it can be tedious to optimize all junction types independently when the production experiences a variety of portfolios within a small batch size. The artificial neural network approach has been applied to develop an adaptive void-filling strategy as well as to reuse the knowledge for welding arbitrary junction types. The rule-based relationship between the void length and junction types is established via machine learning that is based on experimental training data. Generally speaking, the more experimental training data there is, the more precise the trained network is, but the process of generating this data is probably costly and time-consuming. The optimal number of training data ensures proper prediction and minimizes the required amount of training data. The optimal training set has been determined by gradually reducing the number of training data, resulting in 46 junction geometries. This optimal training set was used to train a neural network so that it could make accurate predictions for the 17 validation cases. Sufficient information could be gathered within

a single day that allows for welding other rib-web structures without defects. It is important to note that the methodology presented here may not be transferred directly onto other machines, materials or process parameters, but acts as a guideline or a reference with dedicated geometries.

Although voids can be compensated, peaks emerge at junction as well. There is a trade-off between the benefits of void correction and peak development. It is not possible to avoid voids and peak development at the same time, hence, one should be sacrificed. This method prioritized the avoidance of voids as a main objective. Despite this, the peak tolerates the deposition process to a certain height.

For future work, an adaptive correction tool can be further developed when various welding parameters are considered. Strategies to avoid peaks emerging at junctions should also be developed. To fully exploit the method, deformation, distortion and residual stresses should be analyzed and considered in order to optimize the welding and tool path.

❖ **Multi-axis deposition approach**

The three-axis platform limits the construction of large overhanging or inclined features due to the properties of the WAAM process, making support material and scaffold structures inappropriate. The multi-axis deposition strategy is proposed so as to explore the full use of WAAM. To realize the multi-axis deposition strategy, each overhanging or inclined feature is deposited with a distinct direction and the growth direction is aligned with the central axis of each feature. The developed algorithm detects overhanging features and slices them along their skeleton. The welding position is set to be perpendicular to the slicing plane, which denotes the normal vector of this slicing plane. To reduce the impact of gravity on an inclined surface, the FANUC robot-based WAAM system is employed. The WAAM system includes a six-axis robot arm equipped with the CMT welder, and a substrate that is mounted on a two-axis positioner. The kinematics of the robot system is established based on the normal vector, which results in the new position of control points, the positioner's angles, and the orientation of the gun. The use of the positioner is preferable whenever feasible to minimize the flow of weld pool. The suggested algorithm is developed in Rhinoceros/Grasshopper and MATLAB, resulting in a multi-axis CAM program and is validated by the construction of an overhanging feature. In small overhangs, such as the cylinder, the metal part is manufactured in a 2D manner, where the positioner remains at the setting position. For large overhangs, such as the handles, the positioner and the robot arm coordinate to ensure the neutral welding position.

❖ Fabrication of bent hollow structures

The benefits of the multi-axis deposition strategy are further extended in the fabrication of curved thin-walled hollow structures, offering another manufacturing method for applications like structural frames, wiring conduit, and gas and fluid transportation. The new tool path generation tool was developed in Rhinoceros/Grasshopper and MATLAB and the result shows that the WAAM process with multi-axis deposition can fabricate bent hollow features. The slicing plane follows the skeleton of the bent structures by manipulating its orientation from local geometry. Each slice might result a non-uniform cross section manufactured by adjusting the travel speed. With a constant wire-feed rate, higher travel speed leads to a smaller and thinner weld bead and vice versa. The positioner and the robot arm coordinate to reduce the impact of gravity on weld pool and to maintain the neutral welding position. The tool path is optimized by using the continuous pattern to avoid uneven weld beads, and the experimental data reveals that the continuous path yields a better surface quality. In addition, a guideline for designers and/or users about the correlation between tube curvature and diameter is also provided.

The feasibility of the developed strategy is validated from the fabrication of four test geometries, which can be properly manufactured. Furthermore, the performance of metal parts was evaluated from destructive and non-destructive tests. From the destructive test, macrographs show that no cracks nor welding imperfections, and a proper bonding among adjacent layers. Due to irregular material expansion and shrinkage, welded parts usually yielded high residual stresses, leading to deformation and distortion. The non-destructive test was used to examine the geometric accuracy of deposited parts. The results revealed that all metal parts experienced inaccurate geometry and are deformed. To ensure geometric accuracy, it would be worth implementing a compensation strategy. Due to complex thermal behavior, an offline method is more suitable than an online one. When repeatability was investigated, it was determined that the deposition process for complex parts is repeatable, proving the deviation among metal parts to be minor and the offline compensation strategy to be useful. A run-by-run method has been developed to compensate for the shrinkage and distortion, based on experimental information. For all considered geometries, the compensation process converges in the first iteration. The deviation between the actual parts and CAD models is within the tolerance, which is defined as surface waviness.

For future research, a simulation approach to estimate the necessary information to correct the part can be useful. Metal parts can be ensured geometric accuracy without scarifying a metal part.

8.Publications

The following documents have been produced from this monograph:

- Decomposition algorithm for tool path planning for wire-arc additive manufacturing. *Journal of Machine Engineering*. 2018, Vol.18 (No.1), 96-107. Available from: 10.5604/01.3001.0010.8827.
- Multi-bead overlapping models for tool path generation in wire-arc additive manufacturing processes. *Procedia Manufacturing*. 2020, 47, 1123-1128. Available from: 10.1016/j.promfg.2020.04.129.
- Continuous Eulerian tool path strategies for wire-arc additive manufacturing of rib-web structures with machine-learning-based adaptive void filling, *Journal of Additive Manufacturing*. 2020. Available from: doi.org/10.1016/j.addma.2020.101265.
- Analysis and compensation of shrinkage and distortion in wire-arc additive manufacturing of thin-walled curved hollow sections, submitted to *Journal of Additive Manufacturing*. 2021. Available from: doi.org/10.1016/j.addma.2021.102365.
- Producing curved thin-walled structures by control of welding speed in wire-arc additive manufacturing (*The International Journal of Advanced Manufacturing Technology*).

9.Literatures

1. Ventola CL (2014) Medical applications for 3D printing: current and projected uses. *PT* 39:704–711
2. Associates W (2019) Wohlers report 2019: 3D printing and additive manufacturing state of the industry. Wohlers Associates, Fort Collins, Colorado
3. Mohd Yusuf S, Cutler S, Gao N (2019) Review: The Impact of Metal Additive Manufacturing on the Aerospace Industry. *Metals* 9:1286. <https://doi.org/10.3390/met9121286>
4. Junk S, Tränkle M (2011) Design for Additive Manufacturing technologies: New Applications of 3D-Printing for Rapid Prototyping and Rapid Tooling. In: *DS 68-5: Proceedings of the 18th International Conference on Engineering Design (ICED 11), Impacting Society through Engineering Design, Vol. 5: Design for X/Design to X*, Lyngby/Copenhagen, Denmark, 15.-19.08. 2011
5. Joshi SC, Sheikh AA (2015) 3D printing in aerospace and its long-term sustainability. *Virtual and Physical Prototyping* 10:175–185. <https://doi.org/10.1080/17452759.2015.1111519>
6. Lyons B (2014) Additive manufacturing in aerospace: Examples and research outlook. *The Bridge* 44
7. Song Y-A, Park S, Chae S-W (2005) 3D welding and milling: part II—optimization of the 3D welding process using an experimental design approach. *International Journal of Machine Tools and Manufacture* 45:1063–1069. <https://doi.org/10.1016/j.ijmachtools.2004.11.022>
8. Giffi CA, Gangula B, Illinda P (2014) 3D Opportunity for the Automotive Industry.”
9. COREY CLARKE (2017) Dutch RAMLAB and Autodesk showcase first 3D printed ship component. <https://3dprintingindustry.com/news/dutch-ramlab-autodesk-showcase-first-3d-printed-ship-component-111548/>. Accessed 09 May 2017
10. Paolini A, Kollmannsberger S, Rank E (2019) Additive manufacturing in construction: A review on processes, applications, and digital planning methods. *Additive Manufacturing* 30:100894. <https://doi.org/10.1016/j.addma.2019.100894>
11. van Woensel RNP, van Oirschot T, Burgmans MJH et al. (2018) Printing Architecture: An Overview of Existing and Promising Additive Manufacturing Methods and Their Application in the Building Industry. *The International Journal of the Constructed Environment* 9:57–81. <https://doi.org/10.18848/2154-8587/CGP/v09i01/57-81>
12. Manoharan V, Chou SM, Forrester S et al. (2013) Application of additive manufacturing techniques in sports footwear. *Virtual and Physical Prototyping* 8:249–252
13. Melchels FPW, Domingos MAN, Klein TJ et al. (2012) Additive manufacturing of tissues and organs. *Progress in Polymer Science* 37:1079–1104
14. Murr LE, Gaytan SM, Martinez E et al. (2012) Next generation orthopaedic implants by additive manufacturing using electron beam melting. *Int J Biomater* 2012:245727. <https://doi.org/10.1155/2012/245727>

15. Le Murr, Gaytan SM, Medina F et al. (2010) Next-generation biomedical implants using additive manufacturing of complex, cellular and functional mesh arrays. *Philosophical Transactions of the Royal Society of London A: Mathematical, Physical and Engineering Sciences* 368:1999–2032
16. Reeves P, Mendis D (2015) The Current Status and Impact of 3D Printing Within the Industrial Sector: An Analysis of Six Case Studies
17. Coykendall J, Cotteleer M, Holdowsky J et al. (2014) 3D opportunity in aerospace and defense: Additive manufacturing takes flight. A Deloitte series on additive manufacturing 1
18. Markets S (2014) Additive manufacturing in aerospace: Strategic implications. White paper. Consulted at: <http://www.smarttechpublishing.com>
19. Michel F, Lockett H, Ding J et al. (2019) A modular path planning solution for Wire + Arc Additive Manufacturing. *Robotics and Computer-Integrated Manufacturing* 60:1–11. <https://doi.org/10.1016/j.rcim.2019.05.009>
20. Awd M, Tenkamp J, Hirtler M et al. (2017) Comparison of Microstructure and Mechanical Properties of Scalmetalloy® Produced by Selective Laser Melting and Laser Metal Deposition. *Materials (Basel)* 11. <https://doi.org/10.3390/ma11010017>
21. Yadroitsev I, Smurov I (2010) Selective laser melting technology: From the single laser melted track stability to 3D parts of complex shape. *Physics Procedia* 5:551–560. <https://doi.org/10.1016/j.phpro.2010.08.083>
22. Deckers J, Meyers S, Kruth JP et al. (2014) Direct Selective Laser Sintering/Melting of High Density Alumina Powder Layers at Elevated Temperatures. *Physics Procedia* 56:117–124. <https://doi.org/10.1016/j.phpro.2014.08.154>
23. Ghosal P, Majumder MC, Chattopadhyay A (2018) Study on direct laser metal deposition. *Materials Today: Proceedings* 5:12509–12518. <https://doi.org/10.1016/j.matpr.2018.02.232>
24. Näsström J, Brueckner F, Kaplan AFH (2019) Laser enhancement of wire arc additive manufacturing. *Journal of Laser Applications* 31:22307. <https://doi.org/10.2351/1.5096111>
25. Chang S, Zhang H, Xu H et al. (2019) Online Measurement of Deposit Surface in Electron Beam Freeform Fabrication. *Sensors (Basel)* 19. <https://doi.org/10.3390/s19184001>
26. Stecker S, Lachenberg KW, Wang H et al. (2006) Advanced electron beam free form fabrication methods & technology. AWS welding show', Atlanta, GA:35–46
27. Elmer JW, Gibbs G (2019) The effect of atmosphere on the composition of wire arc additive manufactured metal components. *Science and Technology of Welding and Joining* 24:367–374. <https://doi.org/10.1080/13621718.2019.1605473>
28. Daminabo SC, Goel S, Grammatikos SA et al. (2020) Fused deposition modeling-based additive manufacturing (3D printing): techniques for polymer material systems. *Materials Today Chemistry* 16:100248. <https://doi.org/10.1016/j.mtchem.2020.100248>
29. (2019) Biomimetic Nanoengineered Materials for Advanced Drug Delivery. Elsevier

30. -Plocher J, Panesar A (2018) Next-Generation Fibre-Reinforced Lightweight Structures for Additive Manufacturing. In: 29th Annu. Int. Solid Free. Fabr. Symp., Austin, Texas, USA, pp 664–684
31. Moreno Nieto D, Casal López V, Molina SI (2018) Large-format polymeric pellet-based additive manufacturing for the naval industry. *Additive Manufacturing* 23:79–85.
<https://doi.org/10.1016/j.addma.2018.07.012>
32. Liu B, Wildman R, Tuck C et al. Investigation the effect of particle size distribution on processing parameters optimisation in selective laser melting process
33. CONCEPTLASER Co. LTD Technical Data of X LINE 2000R Metal laser melting system
34. Tolochko NK, Mozzharov SE, Yadroitsev IA et al. (2004) Selective laser sintering and cladding of single-component metal powders. *Rapid Prototyping Journal* 10:88–97.
<https://doi.org/10.1108/13552540410526962>
35. Previtali B, Demir AG, Bucconi M et al. Comparative costs of additive manufacturing vs. machining: The case study of the production of forming dies for tube bending. In:
36. Ding D, Pan Z, Cuiuri D et al. (2015) Process planning for robotic wire and arc additive manufacturing. In: *Industrial Electronics and Applications (ICIEA), 2015 IEEE 10th Conference on*, pp 2000–2003
37. John N. Dupont, Arnold R. Marder (1995) Thermal efficiency of arc welding processes. In:
38. Kapustka N, Harris ID (2014) Exploring arc welding for additive manufacturing of titanium parts. *Welding journal* 93:32–35
39. Williams SW, Martina F, Addison AC et al. (2015) Wire + Arc Additive Manufacturing. *Materials Science and Technology* 32:641–647. <https://doi.org/10.1179/1743284715Y.0000000073>
40. MX3D The MX3D Bridge. <http://mx3d.com/projects/bridge/>. Accessed 05 Aug 2017
41. Shirizly A, Dolev O (2019) From Wire to Seamless Flow-Formed Tube: Leveraging the Combination of Wire Arc Additive Manufacturing and Metal Forming. *JOM* 71:709–717. <https://doi.org/10.1007/s11837-018-3200-x>
42. Singh R (2016) Welding and Joining Processes. In: *Applied Welding Engineering*. Elsevier, pp 163–195
43. Suryakumar S, Karunakaran KP, Bernard A et al. (2011) Weld bead modeling and process optimization in hybrid layered manufacturing. *Computer-Aided Design* 43:331–344
44. Beuth J, Klingbeil N (2001) The role of process variables in laser-based direct metal solid freeform fabrication. *JOM* 53:36–39. <https://doi.org/10.1007/s11837-001-0067-y>
45. Ding D, Pan Z, Cuiuri D et al. (2015) A multi-bead overlapping model for robotic wire and arc additive manufacturing (WAAM). *Robotics and Computer-Integrated Manufacturing* 31:101–110.
<https://doi.org/10.1016/j.rcim.2014.08.008>
46. Chan B, Pacey J, Bibby M (1999) Modelling Gas Metal Arc Weld Geometry Using Artificial Neural Network Technology. *Canadian Metallurgical Quarterly* 38:43–51.
<https://doi.org/10.1179/cmqr.1999.38.1.43>

47. Pavan Kumar N, Devarajan PK, Arungalai Vendan S et al. (2017) Prediction of bead geometry in cold metal transfer welding using back propagation neural network. *Int J Adv Manuf Technol* 93:385–392. <https://doi.org/10.1007/s00170-016-9562-8>
48. Xiong J, Zhang G, Hu J et al. (2012) Bead geometry prediction for robotic GMAW-based rapid manufacturing through a neural network and a second-order regression analysis. *Journal of Intelligent Manufacturing* 25:157–163
49. Heralić A, Christiansson A-K, Lennartson B (2012) Height control of laser metal-wire deposition based on iterative learning control and 3D scanning. *Optics and Lasers in Engineering* 50:1230–1241. <https://doi.org/10.1016/j.optlaseng.2012.03.016>
50. Aviles-Viñas JF, Rios-Cabrera R, Lopez-Juarez I (2016) On-line learning of welding bead geometry in industrial robots. *Int J Adv Manuf Technol* 83:217–231. <https://doi.org/10.1007/s00170-015-7422-6>
51. Neto, Leonor Machado Santos Carvalho (2017) Studying the Application of Additive Manufacturing to Large Parts. Universidade de Lisboa
52. Ma G, Zhao G, Li Z et al. (2018) Optimization strategies for robotic additive and subtractive manufacturing of large and high thin-walled aluminum structures. *Int J Adv Manuf Technol* 52:589. <https://doi.org/10.1007/s00170-018-3009-3>
53. Flores J, Garmendia I, Pujana J (2018) Toolpath generation for the manufacture of metallic components by means of the laser metal deposition technique. *Int J Adv Manuf Technol* 93:2571. <https://doi.org/10.1007/s00170-018-3124-1>
54. Li Y, Han Q, Zhang G et al. (2018) A layers-overlapping strategy for robotic wire and arc additive manufacturing of multi-layer multi-bead components with homogeneous layers. *Int J Adv Manuf Technol* 96:3331–3344. <https://doi.org/10.1007/s00170-018-1786-3>
55. Zhang YM, Li P, Chen Y et al. (2002) Automated system for welding-based rapid prototyping. *Mechatronics* 12:37–53. [https://doi.org/10.1016/S0957-4158\(00\)00064-7](https://doi.org/10.1016/S0957-4158(00)00064-7)
56. Sun SH, Chiang HW, Lee MI (2007) Adaptive direct slicing of a commercial CAD model for use in rapid prototyping. *The international journal of advanced manufacturing technology* 34:689–701
57. Jin YA, He Y, Fu JZ (2013) An adaptive tool path generation for fused deposition modeling. In: *Advanced Materials Research*, vol 819, pp 7–12
58. Almeida PS, Williams S (2010) Innovative process model of Ti-6Al-4V additive layer manufacturing using cold metal transfer (CMT). In: *Proceedings of the twenty-first annual international solid freeform fabrication symposium*, University of Texas at Austin, Austin, TX, USA
59. Martina F, Mehnen J, Williams SW et al. (2012) Investigation of the benefits of plasma deposition for the additive layer manufacture of Ti-6Al-4V. *Journal of Materials Processing Technology* 212:1377–1386. <https://doi.org/10.1016/j.jmatprotec.2012.02.002>

60. Ding J, Colegrove P, Mehnen J et al. (2011) Thermo-mechanical analysis of Wire and Arc Additive Layer Manufacturing process on large multi-layer parts. *Computational Materials Science*.
<https://doi.org/10.1016/j.commatsci.2011.06.023>
61. Murakawa H (2013) Residual stress and distortion in laser welding. In: *Handbook of Laser Welding Technologies*. Residual stress and distortion in laser welding. Elsevier, 374-400e
62. Nasir NSM, Razab MKAA, Mamat S et al. (2006) REVIEW ON WELDING RESIDUAL STRESS. *stress* 2:8–10
63. Mishurova T, BAMBACH M, Sydow B et al. (2020) Residual Stress and Microstructure of a Ti-6Al-4V Wire Arc Additive Manufacturing Hybrid Demonstrator. *Metals* 10. <https://doi.org/10.3390/met10060701>
64. (2016) *Applied Welding Engineering*. Elsevier
65. Jacobs P (2000) The effects of random noise shrinkage on rapid tooling accuracy. *Materials & Design* 21:127–136. [https://doi.org/10.1016/S0261-3069\(99\)00060-6](https://doi.org/10.1016/S0261-3069(99)00060-6)
66. Katayama S (2013) Defect formation mechanisms and preventive procedures in laser welding. In: *Handbook of Laser Welding Technologies*. Elsevier, pp 332–373
67. Corbin DJ, Nassar AR, Reutzel EW et al. (2018) Effect of Substrate Thickness and Preheating on the Distortion of Laser Deposited Ti–6Al–4V. *J Manuf Sci Eng* 140:824. <https://doi.org/10.1115/1.4038890>
68. McAndrew AR, Alvarez Rosales M, Colegrove PA et al. (2018) Interpass rolling of Ti-6Al-4V wire + arc additively manufactured features for microstructural refinement. *Additive Manufacturing* 21:340–349. <https://doi.org/10.1016/j.addma.2018.03.006>
69. Hönnige JR, Colegrove PA, Ganguly S et al. (2018) Control of residual stress and distortion in aluminium wire + arc additive manufacture with rolling. *Additive Manufacturing* 22:775–783. <https://doi.org/10.1016/j.addma.2018.06.015>
70. F. Martina, M. J. Roy, B. A. Szost et al. (2016) Residual stress of as-deposited and rolled wire+arc additive manufacturing Ti–6Al–4V components. *Materials Science and Technology* 32:1439–1448. <https://doi.org/10.1080/02670836.2016.1142704>
71. Graf M, Hälsig A, Höfer K et al. (2018) Thermo-Mechanical Modelling of Wire-Arc Additive Manufacturing (WAAM) of Semi-Finished Products. *Metals* 8:1009. <https://doi.org/10.3390/met8121009>
72. Mukherjee T, Zhang W, DebRoy T (2017) An improved prediction of residual stresses and distortion in additive manufacturing. *Computational Materials Science* 126:360–372. <https://doi.org/10.1016/j.commatsci.2016.10.003>
73. Anwar MS, Untawale SP (2012) Measuring the process efficiency of controlled welding processes. *Int. J. Instrum. Control Autom* 1:33–39
74. Imoudu NE, Ayele YZ, Barabadi A (2017) The characteristic of cold metal transfer (CMT) and its application for cladding. In: *2017 IEEE International Conference on Industrial Engineering and Engineering Management (IEEM)*, pp 1883–1887

75. Ola OT, Doern FE (2014) A study of cold metal transfer clads in nickel-base INCONEL 718 superalloy. *Materials & Design* 57:51–59. <https://doi.org/10.1016/j.matdes.2013.12.060>
76. Denlinger ER, Michaleris P (2017) Mitigation of distortion in large additive manufacturing parts. *Proceedings of the Institution of Mechanical Engineers, Part B: Journal of Engineering Manufacture* 231:983–993. <https://doi.org/10.1177/0954405415578580>
77. Craeghs T, Bechmann F, Berumen S et al. (2010) Feedback control of Layerwise Laser Melting using optical sensors. *Physics Procedia* 5:505–514. <https://doi.org/10.1016/j.phpro.2010.08.078>
78. Hofman JT (2009) Development of an observation and control system for industrial laser cladding. University of Twente
79. MICRO-EPSILON MESSTECHNIK GmbH Blue Laser triangulation sensors for difficult surface types. www.micro-epsilon.com. Accessed 21 Jul 2020
80. Schmutzler C, Bayerlein F, Janson S et al. (2016) Pre-compensation of Warpage for Additive Manufacturing. *JMEA* 6. <https://doi.org/10.17265/2159-5275/2016.08.002>
81. Montevecchi F, Venturini G, Grossi N et al. (2017) Finite Element mesh coarsening for effective distortion prediction in Wire Arc Additive Manufacturing. *Additive Manufacturing* 18:145–155. <https://doi.org/10.1016/j.addma.2017.10.010>
82. Ding J, Colegrove P, Mehnen J et al. (2014) A computationally efficient finite element model of wire and arc additive manufacture. *Int J Adv Manuf Technol* 70:227–236. <https://doi.org/10.1007/s00170-013-5261-x>
83. Zhang Y, Chen Y, Li P et al. (2003) Weld deposition-based rapid prototyping: A preliminary study. *Journal of Materials Processing Technology* 135:347–357. [https://doi.org/10.1016/S0924-0136\(02\)00867-1](https://doi.org/10.1016/S0924-0136(02)00867-1)
84. Karunakaran KP, Suryakumar S, Chandrasekhar U et al. (2010) Hybrid rapid manufacturing of metallic objects. *IJRAPIDM* 1:433. <https://doi.org/10.1504/IJRapidM.2010.036116>
85. Bai J, Ding HL, Gu JL et al. (2017) Porosity evolution in additively manufactured aluminium alloy during high temperature exposure. *IOP Conf Ser.: Mater Sci Eng* 167:12045. <https://doi.org/10.1088/1757-899X/167/1/012045>
86. Guessasma S, Zhang W, Zhu J et al. (2015) Challenges of additive manufacturing technologies from an optimisation perspective. *Int J Simul Multisci Des Optim* 6:A9. <https://doi.org/10.1051/smdo/2016001>
87. Furumoto T, Koizumi A, Alkahari MR et al. (2015) Permeability and strength of a porous metal structure fabricated by additive manufacturing. *Journal of Materials Processing Technology* 219:10–16. <https://doi.org/10.1016/j.jmatprotec.2014.11.043>
88. Ryan E, Sabin TJ, Watts J et al. (2018) The influence of build parameters and wire batch on porosity of wire and arc additive manufactured aluminium alloy 2319. *Journal of Materials Processing Technology* 262. <https://doi.org/10.1016/j.jmatprotec.2018.07.030>

89. Derekar K, Lawrence J, Melton G et al. (2019) Influence of Interpass Temperature on Wire Arc Additive Manufacturing (WAAM) of Aluminium Alloy Components. *MATEC Web of Conferences* 269:5001. <https://doi.org/10.1051/mateconf/201926905001>
90. Wang D, Lu J, Tang S et al. (2018) Reducing Porosity and Refining Grains for Arc Additive Manufacturing Aluminum Alloy by Adjusting Arc Pulse Frequency and Current. *Materials (Basel)* 11. <https://doi.org/10.3390/ma11081344>
91. Xiong J, Zhang G, Gao H et al. (2013) Modeling of bead section profile and overlapping beads with experimental validation for robotic GMAW-based rapid manufacturing. *Robotics and Computer-Integrated Manufacturing* 29:417–423
92. Nguyen TC, Weckman DC, Johnson DA et al. (2013) High speed fusion weld bead defects. *Science and Technology of Welding and Joining* 11:618–633. <https://doi.org/10.1179/174329306X128464>
93. Kovacevic R (ed) (2012) *Welding Processes*. InTech
94. Soderstrom E, Mendez P (2006) Humping mechanisms present in high speed welding. *Science and Technology of Welding and Joining* 11:572–579. <https://doi.org/10.1179/174329306X120787>
95. DebRoy T, David SA, DuPont JN et al. (2013) *Trends in Welding Research 2012: Proceedings of the 9th International Conference*. ASM International
96. Cheung CF, Ho LT, Charlton P et al. (2010) Analysis of surface generation in the ultraprecision polishing of freeform surfaces. *Proceedings of the Institution of Mechanical Engineers, Part B: Journal of Engineering Manufacture* 224:59–73. <https://doi.org/10.1243/09544054JEM1563>
97. Kim BH, Choi BK (2002) Machining efficiency comparison direction-parallel tool path with contour-parallel tool path. *Computer-Aided Design* 34:89–95. [https://doi.org/10.1016/S0010-4485\(00\)00139-1](https://doi.org/10.1016/S0010-4485(00)00139-1)
98. Ding D, Pan ZS, Cuiuri D et al. (2014) A tool-path generation strategy for wire and arc additive manufacturing. *The international journal of advanced manufacturing technology* 73:173–183
99. Routhu S, Kankanala D, Ruan J et al. (2010) 2-D path planning for direct laser deposition process. In: *ASME 2010 International Design Engineering Technical Conferences and Computers and Information in Engineering Conference*, pp 415–423
100. Bariani PF, Berti G, D'Angelo L (1993) Tool Cost Estimating at the Early Stages of Cold Forging Process Design. *CIRP Annals - Manufacturing Technology* 42:279–282. [https://doi.org/10.1016/S0007-8506\(07\)62443-3](https://doi.org/10.1016/S0007-8506(07)62443-3)
101. Allen J (2006) An investigation into the comparative costs of additive manufacture vs. machine from solid for aero engine parts
102. Mehnen J, Ding J, Lockett H et al. (2011) Design for wire and arc additive layer manufacture. In: *Global Product Development*. Springer, pp 721–727
103. Venturini G, Montevocchi F, Scippa A et al. (2016) Optimization of WAAM Deposition Patterns for T-crossing Features. *Procedia CIRP* 55:95–100. <https://doi.org/10.1016/j.procir.2016.08.043>

104. Venturini G, Montevecchi F, Bandini F et al. (2018) Feature based three axes computer aided manufacturing software for wire arc additive manufacturing dedicated to thin walled components. *Additive Manufacturing* 22:643–657. <https://doi.org/10.1016/j.addma.2018.06.013>
105. Liu HH, Zhao T, Li LY et al. (2020) A path planning and sharp corner correction strategy for wire and arc additive manufacturing of solid components with polygonal cross-sections. *Int J Adv Manuf Technol* 106:4879–4889. <https://doi.org/10.1007/s00170-020-04960-4>
106. Wilson RJ (1979) *Introduction to graph theory*. Pearson Education India
107. Chebolu P, Cryan M, Martin R (2012) Exact counting of Euler tours for generalized series-parallel graphs. *Journal of Discrete Algorithms* 10:110–122. <https://doi.org/10.1016/j.jda.2011.03.011>
108. Cai Y (2016) *Instinctive computing*. Springer, London
109. Coupek D, Friedrich J, Battran D et al. (2018) Reduction of Support Structures and Building Time by Optimized Path Planning Algorithms in Multi-axis Additive Manufacturing. *Procedia CIRP* 67:221–226. <https://doi.org/10.1016/j.procir.2017.12.203>
110. Li L, Haghghi A, Yang Y (2018) A novel 6-axis hybrid additive-subtractive manufacturing process: Design and case studies. *Journal of Manufacturing Processes* 33:150–160. <https://doi.org/10.1016/j.jmapro.2018.05.008>
111. Panchagnula JS, Simhambhatla S (2018) Feature based Weld-Deposition for Additive Manufacturing of Complex Shapes. *J Inst Eng India Ser C* 99:285–292. <https://doi.org/10.1007/s40032-016-0339-5>
112. Flores J, Garmendia I, Pujana J (2018) Toolpath generation for the manufacture of metallic components by means of the laser metal deposition technique. *The international journal of advanced manufacturing technology*:1–10
113. Arregui L, Garmendia I, Pujana J et al. (2018) Study of the Geometrical Limitations Associated to the Metallic Part Manufacturing by the LMD Process. *Procedia CIRP* 68:363–368. <https://doi.org/10.1016/j.procir.2017.12.096>
114. Panchagnula JS, Simhambhatla S (2018) Manufacture of complex thin-walled metallic objects using weld-deposition based additive manufacturing. *Robotics and Computer-Integrated Manufacturing* 49:194–203. <https://doi.org/10.1016/j.rcim.2017.06.003>
115. Mehnen J, Ding J, Lockett H et al. (2014) Design study for wire and arc additive manufacture. *IJPD* 19:2. <https://doi.org/10.1504/IJPD.2014.060028>
116. Kazanas P, Deherkar P, Almeida P et al. (2012) Fabrication of geometrical features using wire and arc additive manufacture. *Proceedings of the Institution of Mechanical Engineers, Part B: Journal of Engineering Manufacture* 226:1042–1051. <https://doi.org/10.1177/0954405412437126>
117. Zhao Y, Jia Y, Chen S et al. (2020) Process planning strategy for wire-arc additive manufacturing: Thermal behavior considerations. *Additive Manufacturing* 32:100935. <https://doi.org/10.1016/j.addma.2019.100935>
118. Yili D, Shengfu Y, Yusheng S et al. (2018) Wire and arc additive manufacture of high-building multi-directional pipe joint. *Int J Adv Manuf Technol* 96:2389–2396. <https://doi.org/10.1007/s00170-018-1742-2>

119. Ruan J, Eiamsa-ard K, Liou FW (2005) Automatic Process Planning and Toolpath Generation of a Multiaxis Hybrid Manufacturing System. *Journal of Manufacturing Processes* 7:57–68. [https://doi.org/10.1016/S1526-6125\(05\)70082-7](https://doi.org/10.1016/S1526-6125(05)70082-7)
120. Prado-Cerqueira JL, Camacho AM, Diéguez JL et al. (2018) Analysis of Favorable Process Conditions for the Manufacturing of Thin-Wall Pieces of Mild Steel Obtained by Wire and Arc Additive Manufacturing (WAAM). *Materials (Basel)* 11. <https://doi.org/10.3390/ma11081449>
121. Awd M, Tenkamp J, Hirtler M et al. (2017) Comparison of Microstructure and Mechanical Properties of Scalmetalloy® Produced by Selective Laser Melting and Laser Metal Deposition. *Materials* 11. <https://doi.org/10.3390/ma11010017>
122. Sizova I, Hirtler M, Günther M et al. (2019) Wire-arc additive manufacturing of pre-forms for forging of a Ti-6Al-4V turbine blade. In: vol 2113, p 150017
123. Xiangfang X, Ganguly S, Ding J et al. (2017) Microstructural evolution and mechanical properties of maraging steel produced by wire + arc additive manufacture process. *Materials Characterization*. <https://doi.org/10.1016/j.matchar.2017.12.002>
124. Wang F, Williams S, Colegrove P et al. (2013) Microstructure and Mechanical Properties of Wire and Arc Additive Manufactured Ti-6Al-4V. *Metall and Mat Trans A* 44:968–977. <https://doi.org/10.1007/s11661-012-1444-6>
125. Caballero A, Ding J, Ganguly S et al. (2019) Wire + Arc Additive Manufacture of 17-4 PH stainless steel: Effect of different processing conditions on microstructure, hardness, and tensile strength. *Journal of Materials Processing Technology* 268:54–62. <https://doi.org/10.1016/j.jmatprotec.2019.01.007>
126. Suryakumar S, Karunakaran KP, Chandrasekhar U et al. (2013) A study of the mechanical properties of objects built through weld-deposition. *Proceedings of the Institution of Mechanical Engineers, Part B: Journal of Engineering Manufacture* 227:1138–1147. <https://doi.org/10.1177/0954405413482122>
127. Kou S (2003) *Welding metallurgy*. New Jersey, USA:431–446
128. Weman K (2011) *Welding processes handbook*. Elsevier
129. Ebrahimnia M, Goodarzi M, Nouri M et al. (2009) Study of the effect of shielding gas composition on the mechanical weld properties of steel ST 37-2 in gas metal arc welding. *Materials & Design* 30:3891–3895. <https://doi.org/10.1016/j.matdes.2009.03.031>
130. Kah P, Martikainen J (2013) Influence of shielding gases in the welding of metals. *Int J Adv Manuf Technol* 64:1411–1421. <https://doi.org/10.1007/s00170-012-4111-6>
131. Mvola B, Kah P (2017) Effects of shielding gas control: Welded joint properties in GMAW process optimization. *Int J Adv Manuf Technol* 88:2369–2387. <https://doi.org/10.1007/s00170-016-8936-2>
132. Zielinska S, Pellerin S, Valensi F et al. (2008) Gas influence on the arc shape in MIG-MAG welding. *Eur Phys J Appl Phys* 43:111–122. <https://doi.org/10.1051/epjap:2008106>

133. Donoghue J, Antonysamy AA, Martina F et al. (2016) The effectiveness of combining rolling deformation with Wire–Arc Additive Manufacture on β -grain refinement and texture modification in Ti–6Al–4V. *Materials Characterization* 114:103–114. <https://doi.org/10.1016/j.matchar.2016.02.001>
134. Hirtler M, Jedynek A, Sydow B et al. (2018) Investigation of microstructure and hardness of a rib geometry produced by metal forming and wire-arc additive manufacturing. *MATEC Web Conf* 190:2005. <https://doi.org/10.1051/mateconf/201819002005>
135. Caballero A, Ding J, Bandari Y et al. (2019) Oxidation of Ti-6Al-4V During Wire and Arc Additive Manufacture. *3D Printing and Additive Manufacturing* 6:91–98. <https://doi.org/10.1089/3dp.2017.0144>
136. Stützer J, Totzauer T, Wittig B et al. (2019) GMAW Cold Wire Technology for Adjusting the Ferrite–Austenite Ratio of Wire and Arc Additive Manufactured Duplex Stainless Steel Components. *Metals* 9:564. <https://doi.org/10.3390/met9050564>
137. Haden CV, Zeng G, Carter FM et al. (2017) Wire and arc additive manufactured steel: Tensile and wear properties. *Additive Manufacturing* 16:115–123. <https://doi.org/10.1016/j.addma.2017.05.010>
138. Ding D, Pan Z, Cuiuri D et al. (2016) Bead modelling and implementation of adaptive MAT path in wire and arc additive manufacturing. *Robotics and Computer-Integrated Manufacturing* 39:32–42. <https://doi.org/10.1016/j.rcim.2015.12.004>
139. Ríos S, Colegrove PA, Martina F et al. (2018) Analytical process model for wire + arc additive manufacturing. *Additive Manufacturing* 21:651–657. <https://doi.org/10.1016/j.addma.2018.04.003>
140. Xiong J, Zhang G, Hu J et al. (2012) Bead geometry prediction for robotic GMAW-based rapid manufacturing through a neural network and a second-order regression analysis. *Journal of Intelligent Manufacturing* 25:157–163
141. Hu Z, Qin X, Li Y et al. (2020) Welding parameters prediction for arbitrary layer height in robotic wire and arc additive manufacturing. *J Mech Sci Technol* 34:1683–1695. <https://doi.org/10.1007/s12206-020-0331-0>
142. International Organization for Standardization (2012) ISO 8373: 2012 (en) Robots and robotic devices- Vocabulary
143. Niku SBaDoMECPSLO (2019) *Introduction to Robotics: Analysis, Control, Applications* / Saeed B. Niku, 3rd
144. Hong TS, Ghobakhloo M, Khaksar W (2014) Robotic Welding Technology. *Comprehensive Materials Processing* 6:77–99. <https://doi.org/10.1016/B978-0-08-096532-1.00604-X>
145. Selvi S, Vishvaksenan A, Rajasekar E (2018) Cold metal transfer (CMT) technology - An overview. *Defence Technology* 14:28–44. <https://doi.org/10.1016/j.dt.2017.08.002>
146. Lorenzin G, Rutili G (2009) The innovative use of low heat input in welding: experiences on ‘cladding’ and brazing using the CMT process. *Welding International* 23:622–632

147. Sun Z, Lv Y, Xu B et al. (2015) Investigation of droplet transfer behaviours in cold metal transfer (CMT) process on welding Ti-6Al-4V alloy. *Int J Adv Manuf Technol* 80:2007–2014.
<https://doi.org/10.1007/s00170-015-7197-9>
148. Fronius International GmbH CMT: Three letters that stand for the most stable weld process in the world
149. Tapiola J (2017) Cold Metal Transfer cladding of wear and corrosion resistant coatings in engine applications, Unpublished
150. Colegrove P, Ikeagu C, Thistlethwaite A et al. (2013) Welding process impact on residual stress and distortion. *Science and Technology of Welding and Joining* 14:717–725.
<https://doi.org/10.1179/136217109X406938>
151. Fronius TPS 320i / 400i / 500i / 600i Operating Instructions: MIG/MAG power source.
152. (2013) Schweißpraxis aktuell: CMT-Technologie: Cold Metal Transfer - ein neuer Metallschutzgas-Schweißprozess. WEKA-Praxislösungen. WEKA-Media, Kissing
153. Fronius International GbmH TPS/i Robotics. www.tps-i.com/en/. Accessed 19 Apr 2020
154. FANUC America Corporation Industrial robots for manufacturing
155. FANUC Robot series R-30iB Mate CONTROLLER(B-83284EN/04)
156. Garc in JA, others (2010) New concepts in automation and robotic technology for surface engineering
157. FANUC Robot series Coordinated Motion Function: B-83484EN/02
158. DIN EN 10083-1
159. Society AW (2005) AWS A 5.18: specification for carbon steel electrodes and rods for gas shielded arc welding
160. S. A. David, R. G. Miller, Z. Feng (2017) Welding of unique and advanced alloys for space and high-temperature applications: welding and weldability of iridium and platinum alloys. *Science and Technology of Welding and Joining* 22:244–256. <https://doi.org/10.1080/13621718.2016.1222255>
161. Trivedi R, David SA, Eshelman MA et al. (2003) In situ observations of weld pool solidification using transparent metal-analog systems. *J Heat Transfer* 93:4885–4895. <https://doi.org/10.1063/1.1559934>
162. Suryakumar S, Karunakaran KP, Bernard A et al. (2011) Weld bead modeling and process optimization in Hybrid Layered Manufacturing. *Computer-Aided Design* 43:331–344.
<https://doi.org/10.1016/j.cad.2011.01.006>
163. Lippert RB, Lachmayer R, others (2016) Bionic inspired infill structures for a light-weight design by using SLM. In: *DS 84: Proceedings of the DESIGN 2016 14th International Design Conference*, pp 331–340
164. Nagamatsu H, Sasahara H, Mitsutake Y et al. (2020) Development of a cooperative system for wire and arc additive manufacturing and machining. *Additive Manufacturing* 31:100896.
<https://doi.org/10.1016/j.addma.2019.100896>
165. Adebayo A (2013) Characterisation of integrated WAAM and machining processes

166. Weisz-Patrault D (2020) Fast simulation of temperature and phase transitions in directed energy deposition additive manufacturing. *Additive Manufacturing* 31:100990. <https://doi.org/10.1016/j.addma.2019.100990>
167. Thompson A, Maskery I, Leach RK (2016) X-ray computed tomography for additive manufacturing: a review. *Meas Sci Technol* 27:72001
168. Slotwinski JA, Garboczi EJ, Hebenstreit KM (2014) Porosity Measurements and Analysis for Metal Additive Manufacturing Process Control. *J Res Natl Inst Stand Technol* 119:494–528. <https://doi.org/10.6028/jres.119.019>
169. Burden F, Winkler D (2008) Bayesian regularization of neural networks. In: *Artificial neural networks*. Springer, pp 23–42
170. Norm D (2009) Prüfung Metallischer Werkstoffe-Zugproben. Deutsches Institut für Normung, DIN 50125
171. Jhavar S, Jain NK, Paul CP (2014) Development of micro-plasma transferred arc (μ -PTA) wire deposition process for additive layer manufacturing applications. *Journal of Materials Processing Technology* 214:1102–1110. <https://doi.org/10.1016/j.jmatprotec.2013.12.016>
172. Krizhevsky A, Sutskever I, Hinton GE (2012) Imagenet classification with deep convolutional neural networks. In: *Advances in neural information processing systems*, pp 1097–1105
173. Maimon O, Rokach L (2008) *Soft Computing for Knowledge Discovery and Data Mining*. Springer US, Boston, MA
174. Pobitra Halder, Norottom Paul, Shamimur Rahman (2013) Effect of welding on the properties of Mild steel & cast iron specimen
175. Pinkerton AJ (2010) Laser direct metal deposition: theory and applications in manufacturing and maintenance. In: *Advances in Laser Materials Processing*. Elsevier, pp 461–491
176. Eisenbarth D, Wirth F, Spieldiener K et al. (2017) Enhanced Toolpath Generation for Direct Metal Deposition by Using Distinctive CAD Data. In: *International Conference on Additive Manufacturing in Products and Applications*, pp 152–161
177. David SA, Babu SS, Vitek JM (2003) Welding: Solidification and microstructure. *JOM* 55:14–20
178. Spong MW (1989) *Robot Dynamics and Control*, 1st. John Wiley & Sons, Inc, New York, NY, USA
179. Steven M. LaValle *PLANNING ALGORITHMS. Geometric Representations and Transformations*
180. Shinkin VN, Kolikov AP (2011) Elastoplastic shaping of metal in an edge-bending press in the manufacture of large-diameter pipe. *Steel in Translation* 41:528
181. Strano M (2005) Automatic tooling design for rotary draw bending of tubes. *Int J Adv Manuf Technol* 26:733–740
182. Ghiotti A, Simonetto E, Bruschi S et al. (2017) Springback measurement in three roll push bending process of hollow structural sections. *CIRP Annals* 66:289–292

183. Collie GJ, Black I (2008) An experimental evaluation of induction bending as a method for producing pipe bends with radii $\geq 2.5D$. Proceedings of the Institution of Mechanical Engineers, Part E: Journal of Process Mechanical Engineering 222:103–114. <https://doi.org/10.1243/09544089JPME163>
184. Shinkin VN (2017) Asymmetric three-roller sheet-bending systems in steel-pipe production. Steel in Translation 47:235–240
185. Asari A (1971) Apparatus for the production of steel pipes by extrusion
186. Zhao Y (2016) The Effect of Shielding Gas Composition on Weld Bead Geometry during Short-circuit GMA Welding of Inconel625 Alloy
187. Kosaki H (1982) Interpolation theory and the Wigner-Yanase-Dyson-Lieb concavity. Communications in Mathematical Physics 87:315–329
188. Dawes R, Thompson DL, Wagner AF et al. (2008) Interpolating moving least-squares methods for fitting potential energy surfaces: A strategy for efficient automatic data point placement in high dimensions. The Journal of chemical physics 128:84107
189. TT-WN 010 (2015) Tolerances for Elbows, Bends and Tube Coils
190. Xiang Wang, Reinhard Klette, Bodo Rosenhahn (2005) Geometric and Photometric Correction of Projected Rectangular Pictures. In:
191. Lam Nguyen, Johannes Buhl, Rameez Israr et al. (2021) Analysis and compensation of shrinkage and distortion in wire-arc additive manufacturing of thin-walled curved hollow sections. Additive Manufacturing 47:102365. <https://doi.org/10.1016/j.addma.2021.102365>
192. Peters B, Pozzetti G (2019) Numerical analysis of powder deposition in direct material injection. Granular Matter 22:2. <https://doi.org/10.1007/s10035-019-0963-x>
193. Montevocchi F, Venturini G, Grossi N et al. (2018) Idle time selection for wire-arc additive manufacturing: A finite element-based technique. Additive Manufacturing 21:479–486. <https://doi.org/10.1016/j.addma.2018.01.007>
194. Bonifaz EA, Palomeque JS (2020) A mechanical model in wire + Arc additive manufacturing process. Progress in Additive Manufacturing 5:163–169. <https://doi.org/10.1007/s40964-020-00112-y>

10. Appendices

A. Experimental data for ANN in rib-web structures

A1. Full experimental data for ANN in rib-web structures

No.	Group	Configuration					L_{Target} (mm)
		η	θ_1 ($^\circ$)	θ_2 ($^\circ$)	θ_3 ($^\circ$)	θ_4 ($^\circ$)	
1	A ₁	3	120	120	120	0	0.8
2	B ₁	2	180	90	90	0	1.0
3	B ₂	3	150	150	60	0	2.1
4	B ₃	3	160	160	40	0	2.5
5	B ₄	3	165	165	30	0	6.2
6	C ₁	3	150	120	90	0	1.2
7	C ₂	2	180	108	72	0	1.5
8	C ₃	2	180	120	60	0	1.6
9	C ₄	2	180	126	54	0	1.7
10	C ₅	2	180	144	36	0	2.5
11	C ₆	2	180	150	30	0	2.8
12	C ₇	2	180	162	18	0	6.8
13	C ₈	2	180	165	15	0	10.0
14	D ₁	4	90	90	90	90	3.0
15	E ₁	3	180	60	60	60	5.0
16	E ₂	4	135	75	75	75	4
17	E ₃	4	100	100	100	60	3
18	F ₁	4	108	72	108	72	4.6
19	F ₂	4	120	60	120	60	6.0
20	F ₃	4	126	54	126	54	3.3
21	F ₄	4	135	45	135	45	9.0
22	F ₅	4	144	36	144	36	9.5
23	F ₆	4	150	30	150	30	12.0
24	F ₇	4	162	18	162	18	24.5
25	F ₈	4	165	15	165	15	28.3
26	F ₉	4	108	72	72	108	3.1
27	F ₁₀	4	120	60	60	120	4.7
28	F ₁₁	4	126	54	54	126	3.3
29	F ₁₂	4	135	45	45	135	5.7
30	F ₁₃	4	144	36	36	144	4.8
31	F ₁₄	4	150	30	30	150	5.5
32	F ₁₅	4	162	18	18	162	10.5
33	F ₁₆	4	165	15	15	165	11.0
34	G ₁	3	180	52	76	52	6.0
35	G ₂	3	180	45	90	45	8.0
36	G ₃	3	180	37	106	37	11.0
37	G ₄	3	180	30	120	30	11.2
38	G ₅	3	180	90	45	45	4.5
39	G ₆	3	180	120	30	30	6.0
40	G ₇	4	108	90	90	72	3.2
41	G ₈	4	120	90	90	60	5.5
42	G ₉	4	126	90	90	54	4.5
43	G ₁₀	4	144	90	90	36	7.0
44	G ₁₁	4	150	90	90	30	9.5
45	G ₁₂	4	162	90	90	18	16.0
46	H ₁	3	180	90	60	30	8.0
47	H ₂	3	180	90	70	20	11.0
48	H ₃	3	180	90	30	60	5.5
49	H ₄	3	180	90	20	70	11.0
50	H ₅	3	180	15	30	135	11.0
51	H ₆	3	180	30	15	135	12.0

52	H ₇	4	126	72	108	54	6.2
53	H ₈	4	144	72	108	36	6.4
54	H ₉	4	144	54	126	36	8.0
55	H ₁₀	4	162	72	108	18	12.5
56	H ₁₁	4	162	54	126	18	14.5
57	H ₁₂	4	162	36	144	18	15.6
58	H ₁₃	4	126	108	72	54	4.6
59	H ₁₄	4	144	108	72	36	5.0
60	H ₁₅	4	144	126	54	36	7.0
61	H ₁₆	4	162	108	72	18	14.5
62	H ₁₇	4	162	126	54	18	12.5
63	H ₁₈	4	162	144	36	18	9.4

A2. Training data for ANN in rib-web structures

No.	Group	Input					Measurement	Prediction	Deviation
		η	θ_1 (°)	θ_2 (°)	θ_3 (°)	θ_4 (°)	L_{Target} (mm)	$L_{Predict}$ (mm)	ΔL (mm)
1	A ₁	3	120	120	120	0	0.8	0.3	-0.5
2	B ₁	2	180	90	90	0	1.0	0.1	-0.9
3	B ₂	3	150	150	60	0	2.1	1.5	-0.6
4	B ₃	3	160	160	40	0	2.5	3.6	1.1
5	B ₄	3	165	165	30	0	6.2	6.3	0.1
6	C ₁	3	150	120	90	0	1.2	1.8	0.6
7	C ₂	2	180	108	72	0	1.5	1.9	0.4
8	C ₃	2	180	120	60	0	1.6	2.0	0.4
9	C ₄	2	180	126	54	0	1.7	0.8	-0.9
10	C ₅	2	180	144	36	0	2.5	1.5	-1.0
11	C ₆	2	180	150	30	0	2.8	2.2	-0.6
12	C ₇	2	180	162	18	0	6.8	6.0	-0.8
13	C ₈	2	180	165	15	0	10.0	10.7	0.7
14	D ₁	4	90	90	90	90	3.0	3.5	0.5
15	E ₁	3	180	60	60	60	5.0	4.0	-1.0
16	E ₂	4	135	75	75	75	4	3.0	-1.0
17	E ₃	4	100	100	100	60	3	3.3	0.3
18	F ₁	4	108	72	108	72	4.6	5.2	0.6
19	F ₂	4	120	60	120	60	6.0	6.4	0.4
20	F ₃	4	126	54	126	54	3.3	3.5	0.2
21	F ₄	4	135	45	135	45	9.0	9.1	0.1
22	F ₅	4	144	36	144	36	9.5	8.4	-1.1
23	F ₆	4	150	30	150	30	12.0	11.6	-0.4
24	F ₈	4	165	15	165	15	28.3	27.5	-0.8
25	F ₉	4	108	72	72	108	3.1	3.4	0.3
26	F ₁₀	4	120	60	60	120	4.7	4.6	-0.1
27	F ₁₁	4	126	54	54	126	3.3	2.3	-1.0
28	F ₁₂	4	135	45	45	135	5.7	8.1	2.4
29	F ₁₃	4	144	36	36	144	4.8	5.4	0.6
30	F ₁₄	4	150	30	30	150	5.5	5.0	-0.5
31	F ₁₅	4	162	18	18	162	10.5	10.4	-0.1
32	F ₁₆	4	165	15	15	165	11.0	11.5	0.5
33	G ₁	3	180	52	76	52	6.0	6.0	0.0
34	G ₂	3	180	45	90	45	8.0	9.5	1.5
35	G ₃	3	180	37	106	37	11.0	10.2	-0.8
36	G ₄	3	180	30	120	30	11.2	10.6	-0.6
37	G ₅	3	180	90	45	45	4.5	4.9	0.4
38	G ₆	3	180	120	30	30	6.0	5.6	-0.4
39	G ₇	4	108	90	90	72	3.2	2.5	-0.7
40	G ₈	4	120	90	90	60	5.5	6.7	1.2
41	G ₉	4	126	90	90	54	4.5	4.3	-0.2
42	G ₁₀	4	144	90	90	36	7.0	6.2	-0.8

43	G ₁₁	4	150	90	90	30	9.5	9.5	0.0
44	G ₁₂	4	162	90	90	18	16.0	16.2	0.2
45	H ₁	3	180	90	60	30	8.0	8.6	0.6
46	H ₂	3	180	90	70	20	11.0	11.1	0.1
47	H ₄	3	180	90	20	70	11.0	10.2	-0.8
48	H ₅	3	180	15	30	135	11.0	11.7	0.7
49	H ₆	3	180	30	15	135	12.0	12.6	0.6
50	H ₇	4	126	72	108	54	6.2	7.0	0.8
51	H ₈	4	144	72	108	36	6.4	6.2	-0.2
52	H ₉	4	144	54	126	36	8.0	9.5	1.5
53	H ₁₀	4	162	72	108	18	12.5	13.0	0.5
54	H ₁₁	4	162	54	126	18	14.5	14.2	-0.3
55	H ₁₂	4	162	36	144	18	15.6	15.4	-0.2
56	H ₁₃	4	126	108	72	54	4.6	7.1	2.5
57	H ₁₄	4	144	108	72	36	5.0	5.6	0.6
58	H ₁₆	4	162	108	72	18	14.5	15.1	0.6
59	H ₁₇	4	162	126	54	18	12.5	12.8	0.3
60	H ₁₈	4	162	144	36	18	9.4	9.1	-0.3

A3. Optimal training data for ANN in rib-web structures

No.	Group	Input					Measurement	Prediction	Deviation
		η	θ_1 (°)	θ_2 (°)	θ_3 (°)	θ_4 (°)	L_{Target} (mm)	$L_{Predict}$ (mm)	ΔL (mm)
1	B ₁	2	180	90	90	0	1.0	1.51	0.5
2	B ₂	3	150	150	60	0	2.1	2.28	0.2
3	B ₃	3	160	160	40	0	2.5	2.56	0.1
4	B ₄	3	165	165	30	0	6.2	6.30	0.1
5	C ₁	3	150	120	90	0	1.2	1.58	0.4
6	C ₃	2	180	120	60	0	1.62	2.00	0.4
7	C ₄	2	180	126	54	0	1.7	1.37	-0.3
8	C ₅	2	180	144	36	0	2.5	3.01	0.5
9	C ₇	2	180	162	18	0	6.8	6.11	-0.7
10	C ₈	2	180	165	15	0	10.0	9.32	-0.7
11	D ₁	4	90	90	90	90	3.0	2.98	0.0
12	E ₁	3	180	60	60	60	5.0	6.49	1.5
13	E ₂	4	135	75	75	75	4.0	4.40	0.4
14	E ₃	4	100	100	100	60	3.0	3.38	0.4
15	F ₁	4	108	72	108	72	4.6	4.47	-0.1
16	F ₂	4	120	60	120	60	6.0	6.02	0.0
17	F ₄	4	135	45	135	45	9.0	8.17	-0.8
18	F ₇	4	162	18	162	18	24.5	24.60	0.1
19	F ₈	4	165	15	165	15	28.3	28.98	0.7
20	F ₉	4	108	72	72	108	3.1	3.60	0.5
21	F ₁₀	4	120	60	60	120	4.7	4.14	-0.6
22	F ₁₂	4	135	45	45	135	5.7	5.20	-0.5
23	F ₁₃	4	144	36	36	144	4.8	4.28	-0.5
24	F ₁₄	4	150	30	30	150	5.5	6.11	0.6
25	F ₁₆	4	165	15	15	165	11.0	11.31	0.3
26	G ₁	3	180	52	76	52	6.0	6.95	0.9
27	G ₂	3	180	45	90	45	8.0	8.23	0.2
28	G ₃	3	180	37	106	37	11.0	11.36	0.4
29	G ₇	4	108	90	90	72	3.2	3.41	0.2
30	G ₈	4	120	90	90	60	5.5	5.38	-0.1
31	G ₁₀	4	144	90	90	36	7.0	6.57	-0.4
32	G ₁₁	4	150	90	90	30	9.5	9.80	0.3
33	G ₁₂	4	162	90	90	18	16.0	17.06	1.1
34	H ₁	3	180	90	60	30	8.0	7.93	-0.1
35	H ₂	3	180	90	70	20	11.0	11.09	0.1

36	H ₃	3	180	90	30	60	5.5	5.24	-0.3
37	H ₄	3	180	90	20	70	11.0	10.93	-0.1
38	H ₅	3	180	15	30	135	11.0	10.37	-0.6
39	H ₆	3	180	30	15	135	12.0	11.80	-0.2
40	H ₇	4	126	72	108	54	6.2	6.21	0.0
41	H ₉	4	144	54	126	36	8.0	8.45	0.4
42	H ₁₂	4	162	36	144	18	15.6	14.36	-1.2
43	H ₁₄	4	144	108	72	36	5.0	4.95	-0.1
44	H ₁₅	4	144	126	54	36	7.0	6.48	-0.5
45	H ₁₆	4	162	108	72	18	14.5	17.92	3.4
46	H ₁₇	4	162	126	54	18	12.5	12.14	-0.4
47	A ₁	3	120	120	120	0	0.8	1.91	1.1
47	C ₂	2	180	108	72	0	1.5	1.53	0.0
49	C ₆	2	180	150	30	0	2.8	4.34	1.5
50	F ₃	4	126	54	126	54	3.3	7.17	3.9
51	F ₅	4	144	36	144	36	9.5	11.29	1.8
52	F ₆	4	150	30	150	30	12	14.12	2.1
53	F ₁₁	4	126	54	54	126	3.3	5.01	1.7
54	F ₁₅	4	162	18	18	162	10.5	9.59	-0.9
55	G ₄	3	180	30	120	30	11.2	12.11	0.9
56	G ₅	3	180	90	45	45	4.5	7.25	2.7
57	G ₆	3	180	120	30	30	6.0	8.30	2.3
58	G ₉	4	126	90	90	54	4.5	5.13	0.6
59	H ₈	4	144	72	108	36	6.4	7.44	1.0
60	H ₁₀	4	162	72	108	18	12.5	14.99	2.5
61	H ₁₁	4	162	54	126	18	14.5	14.00	-0.5
62	H ₁₃	4	126	108	72	54	4.6	4.85	0.2
63	H ₁₈	4	162	144	36	18	9.4	11.80	2.4

B. Solving trigonometric equation for rotation angles

$$d. \cos \theta_z - e. \sin \theta_z = a \quad (\text{B.1})$$

$$d. \cos \theta_x \cdot \sin \theta_z + e. \cos \theta_x \cdot \cos \theta_z - f. \sin \theta_x = b \quad (\text{B.2})$$

$$d. \sin \theta_x \cdot \sin \theta_z + e. \sin \theta_x \cdot \cos \theta_z + f. \cos \theta_x = c \quad (\text{B.3})$$

Let denote $t = \tan(\theta_z/2)$, we have:

$$\left\{ \begin{array}{l} \sin \theta_z = 2 \sin(\theta_z/2) \cdot \cos(\theta_z/2) = 2 \frac{\sin(\theta_z/2)}{\cos(\theta_z/2)} \cdot \cos^2(\theta_z/2) \\ \cos(\theta_z) = \cos^2(\theta_z/2) - \sin^2\left(\frac{\theta_z}{2}\right) = \left(1 - \frac{\sin^2\left(\frac{\theta_z}{2}\right)}{\cos^2\left(\frac{\theta_z}{2}\right)}\right) \cdot \cos^2(\theta_z/2) \end{array} \right.$$

$$\Rightarrow \left\{ \begin{array}{l} \sin \theta_z = \frac{2t}{1+t^2} \\ \cos \theta_z = \frac{1-t^2}{1+t^2} \end{array} \right. \quad (\text{B.4})$$

Substituting Eq. (B.4) into the formula in Eq. (B.1):

$$d \frac{1 - t^2}{1 + t^2} - e \frac{2t}{1 + t^2} = a$$

$$\Rightarrow (a + d)t^2 + 2et + a - d = 0 \tag{B.5}$$

The unknown variable (t) can be obtained from the quadratic equation Eq. (B.5). It is possible that the quadratic equation results in two values. The rotating angle (θ_z) is then retrieved, and the tilting angle (θ_x) can be computed from Eq. (B.2) or Eq. (B.3).